Potential for analysis of microseismicity from a single-station record at the Åknes unstable rockslope

Vetle Christiansen

Thesis submitted for the degree of
Master in Geosciences: Geophysics and Geodynamics
60 credits

Department of Geosciences
Faculty of mathematics and natural sciences

UNIVERSITY OF OSLO

Spring 2021

Potential for analysis of microseismicity from a single-station record at the Åknes unstable rockslope

Vetle Christiansen

Potential for analysis of microseismicity from a single-station record at the Åknes unstable rockslope

http://www.duo.uio.no/

Printed: Reprosentralen, University of Oslo

Abstract

Åknes is an unstable rockslope in Stranda municipality in western Norway. A failure of the slope has the potential of creating a tsunami where waves can reach a height of up to 85 m, posing a threat to nearby settlements. Monitoring of the slope is important to better understand the deformation and deformation changes at the site. In addition to direct measurements, seismic monitoring may provide useful knowledge on the slope mechanisms, as seismic instrumentation could record local events related to the deformation processes. An important task is to detect these local events and classify them, analyse their time distribution and localize them. In this study, microseismicity at the Åknes site was analysed using a three-components broadband seismometer. The overall aim was to reveal the potential for using the broadband seismometer for analysis of microseismicity at the site. It included detection and classification of local events, investigation of their distribution over three and a half months in comparison with meteorological parameters and estimation of source directions. Events were detected by using STA/LTA triggering and template event cross-correlation and classified based on their signature in both the time and frequency domain. It was found that a single-station record has the potential for being used to local seismicity at Åknes. Amongst the findings was several ≪slopequakes≫, likely to be associated with the slope deformation. A correlation between the time distribution of these events and temperature development at the site was indicated, as the detection rate seemed to increase during temperature rise in the spring. To estimate source directions, polarization analysis of the waveforms was performed. The use of polarization analysis for source direction determination turned out to be challenging, as it was difficult to easily identify different phase arrivals in the waveforms of local events, but it was revealed that the method may be applicable in some cases.

Acknowledgements

The completion of this master thesis would not have been possible without the help and support from several people. First and foremost, I would like to thank my supervisors Valerie Maupin (University of Oslo), Nadège Langet (NORSAR) and Volker Oye (NORSAR) for their guidance, valuable feedback and good discussions during the planning and development of this project the last year. Also, I would like to express my gratitude to my family and friends for their support and encouragement during the work with the thesis and throughout my studies.

Contents

List of Figures

List of Tables

1 Introduction

Rockslides are considered as a serious natural hazard in Norway. Especially in the western part of Norway, which is dominated by deep fjords surrounded by steep hillsides, rockslides could have disastrous consequences. An avalanche of a large rock volume that hits a fjord below may create a tsunami, which can be critical to settlements close to the fjord. There are several historical examples of such events in western Norway, like in Loen (1905 and 1936) and Tafjord (1934), where more than 170 people lost their lives in total (Blikra et al., 2006). Åknes is an unstable rockslope situated in Stranda municipality in western Norway (figure 1). It is in Møre and Romsdal county, not very far away from Tafjord. The site is in the hillside of Sunnylvsfjorden, a part of Storfjorden, at the western side of the fjord. Settlements close to Åknes are Stranda (15 km), Hellesylt (13 km) and Geiranger (24 km). It is covering an area of approximately 1 km^2 and a volume estimated to be 54 mill. m^3 (NVE, 2020). An avalanche from the slope that hits the fjord below could be a serious threat to the nearby settlements, such as Hellesylt and Geiranger, where waves could reach a height of up to 85 m if the entire volume fails (NVE, 2020). Figure 2 shows an overview of the site and the unstable part.

Figure 1: Location of Åknes and nearby settlements (Norgeskart, 2021).

To better understand the mechanisms controlling the slope movement and associated risks, geological mapping and geophysical surveys have been performed at the study site. Geophysical studies include borehole logging, refraction seismic, resistivity surveys and ground penetrating radar. In addition, permanent instrumentation have been installed on the slope. Amongst other things a GPS network, camera, borehole instrumentation, a meteorological station, lasers for distance measurements and seismic instrumentation (Fischer et al., 2019). The seismic network comprises a surface network of geophones, a broadband seismometer and a string of geophones placed in a borehole. In 2005, the surface network of eight three-component geophones was installed in the upper part. A three-component broadband seismometer (AKN) was added in 2009 and a string of eight three-component geophones with 5 m spacing between each was placed in a borehole in 2017. The purpose of the seismic instruments at the site is to provide

additional knowledge on the slope movements to the direct measurements, as they could record local signals related to a possible slide and deformation changes (Roth et al., 2009).

In recent years, the use of microseismic monitoring in rockslide areas has become a more common approach for analysing the mechanisms causing deformation (Fischer et al., 2019). Different processes such as rockfalls, mass-flows and sliding might take place on a rockslope like Åknes. These processes may generate different types of seismic signals that can be recognized in seismic recordings. Detecting and classifying such signals and investigating changes in the seismic record over time can therefore provide useful knowledge on the deformation processes (Provost et al., 2018).

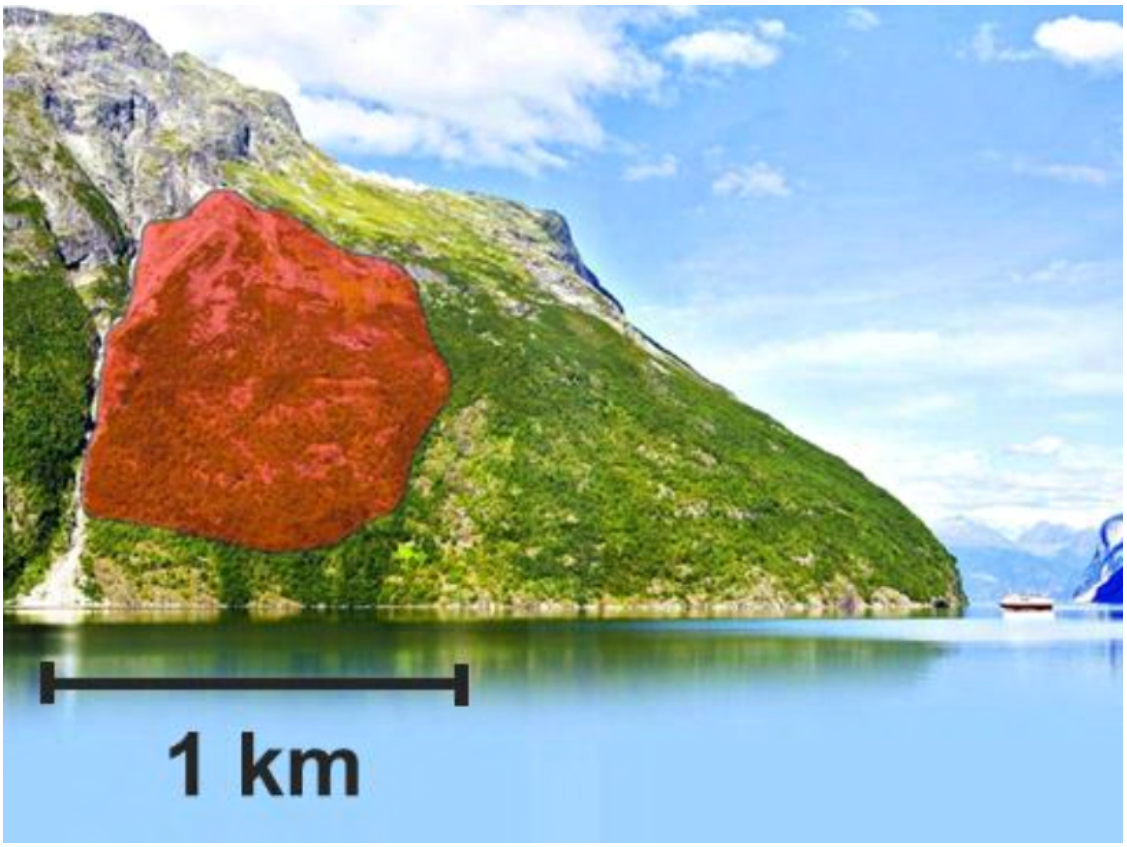

Figure 2: Overview of the study site, from Harbitz et al. (2015). Red area shows the unstable part.

Several studies have already been performed using data recorded from the geophone network, but data from the broadband seismometer (AKN) have not been used very much yet. Continuous broadband records from a three-components single-station can provide useful knowledge on both local and regional events in a wide frequency range (Roth et al., 2009). By studying the polarization of the waveforms, it might be possible to identify different phase arrivals, which in turn can be used to estimate source directions (back-azimuths) to seismic events (Havskov et al., 2011).

Objectives

Overall, the aim of this study was to investigate the potential of using a three-component single-station record for analysing microseismicity at Åknes. It includes the following objectives:

- Detect microseismic events on the broadband seismometer (AKN) at Åknes.
- Classify microseismic events based on their seismic signature in both the time domain and frequency domain.
- Analyse the time distribution of microseismic events over three and a half months and investigate the correlation between meteorological parameters and certain types of signals.
- Investigate the potential for using polarization analysis in order to estimate source directions to local events.

Thesis outline

In the first part of the thesis, a description of the most important characteristics of the study site is given. Further, central theory regarding seismicity related to rockslides, seismic event detection and single-station analysis found in the literature is presented. It continues with a stepwise description of the methods used for event detection, classification and polarization analysis. Finally, the most interesting findings are presented and discussed.

2 Study site: Geological setting and meteorological conditions

2.1 Bedrock

Åknes is situated within the Western Gneiss Region and the bedrock at the site is characterized by different types of gneisses (Tucker et al., 1990). The bedrock is dominated by quartz-dioritic to granitic gneissic rocks, estimated to originate from Proterozoicum (2500-542 Ma). Altering and reworking of the bedrock later occurred during the Caledonian Orogeny (490-390 Ma) (Ganerød et al., 2008). Studies of borehole data from the slope have identified three main lithologies: granitic gneiss, quartz-dioritic gneiss and biotite-rich gneiss (Ganerød et al., 2007). Foliation is commonly seen as dipping parallel/sub-parallel to the slope towards south/southeast in these gneisses, which may affect the slope instability (Braathen et al., 2004).

2.2 Structural geology

The entire slope is approximately 1500 m long from sea level up to about 1300 m.a.s.l. and dipping $30 - 35°$ towards south into Sunnylvsfjorden. Former studies have shown that the unstable part of the site is roughly 1000 m long and 800 m wide, where the upper boundary lies 800-900 m.a.s.l. and the lower boundary at about 150 m.a.s.l. Ganerød et al. (2008) have suggested that the area can be divided into five zones based on structural characteristics. As figure 3 illustrates, these five zones are called 1) the back scarp zone, 2) the toe zone, 3) the western boundary zone, 4) the eastern boundary zone and 5) the central zone.

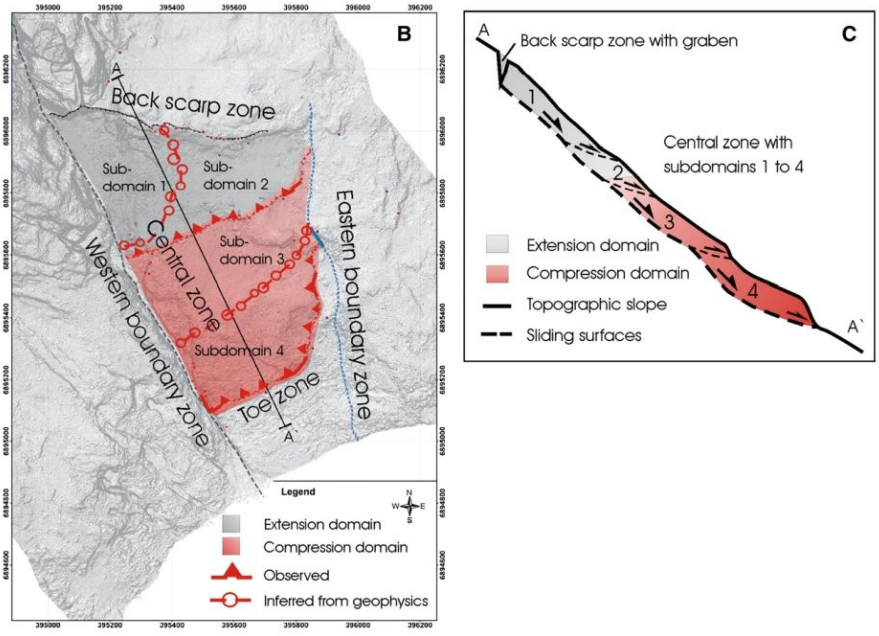

Figure 3: Map from Ganerød et al. (2008) showing the different zones of the rockslide and a sketch of the structural setting.

The back scarp zone defines the upper boundary of the unstable area at 800-900 m.a.s.l. It is approximately 800 m wide in the E-W direction (Grøneng et al., 2011). The westernmost part of the zone shows a cliff that extends about 200 m towards east. A graben structure then continues the zone for about 150 m eastwards. This structure is approximately 20-30 m wide and deep. A fracture characterized by eastwards decreasing width defines the last part of the back scarp zone. It is an open fracture reducing from 20-30 m to 0.5-1 m in the easternmost part (Ganerød et al., 2008). The toe zone is the lower limit of the area at about 150 m.a.s.l. At this lower boundary, a sliding surface that is nearly parallel to the slope topography is observed. The dip angle has been found to vary from about 20° to 32°, some degrees smaller than the average slope topography (Ganerød et al., 2008).

The western boundary zone defines the western limit of the unstable area and is characterized by a steep strike-slip fault which has a NNW-SSE orientation. A crevasse of 10 to 40 m height can be seen at this western boundary. The fault continues further up in the hillside past the rockslide area and could be a structure that is as old as from the Devonian (419-359 Ma) (Osmundsen et al., 2001, Braathen, 1999, Andersen et al., 1997). The eastern boundary zone is the eastern limit at the site. It is characterized by a NNE-SSW striking fault which is slightly dipping towards NW. The dip has been estimated to be about $35 - 45°$. It is a fault zone showing highly fractured rock oriented sub-parallel compared to the fault plane. This fault is most likely also a pre-existing structure (Ganerød et al., 2008). The central zone is the main part of the unstable area, which can be divided into four sub-domains based on movements. Sub-domain 1 and 2 are experiencing extension, while sub-domain 3 and 4 are under compression. In sub-domain 1 movements are in a SW/SSW direction, while the three other sub-domains show displacements in a SE/SSE direction. An undulating basal sliding plane in depth is believed to bound the deforming mass (Ganerød et al., 2008).

Analyses have shown that slope movements are fastest near the back scarp, where displacement rates could be as high as 14 cm/year beneath the back scarp (Heincke et al., 2010). Displacement rates decrease down-slope to 2-4 cm/year in the upper central area, while the lower area experiences an increase in elevation of 1-3 cm/year due to compressional forces (Ganerød et al., 2008).

2.3 Meteorological conditions

Since 2004, a meteorological station located at an elevation of 900 m in the upper slope area has been operated by Norges vassdrags- og energidirektorat (NVE). It provides useful information on meteorological parameters like air temperature, precipitation and snow depth. Yearly average temperature is $2 - 4°C$. From early December to the middle of April, the daily average temperature is commonly below $0°C$, but can also be significantly positive. Large average temperature variations of up to $10°C$ may occur during winter/spring from one day to another.

Analyses of the snow depth have shown that snow commonly starts to accumulate during November and is totally gone by the end of May (Grøneng et al., 2011). Investigations of the snow melt period from 2005-2008 by Grøneng et al. (2011), have shown that there can be great

variations from one year to the next. They found that the beginning of the snow melt varied from early March to middle of April, and the length of the period from 3 weeks to 1.5 months. The snow depth is normally about 2 m at the most during winter, measured at the station. The total precipitation at the site is commonly between 1500 and 2000 mm/year and at the most in the autumn. Lower precipitations are usually observed from April to August. During the winter months and early spring (December-March/April) they fall mostly as snow, when air temperatures drop below $0°C$ (Grøneng et al., 2011).

Studies of displacements at the site with both extensometers and lasers have shown that there might exist a link between displacement rates at Åknes and meteorological parameters, such as precipitation and temperature. As temperatures become positive from late winter/early spring, measurements have indicated an increase in extensional movements in the back scarp zone. It could imply a connection between meltwater and displacement rates during spring. Oppositely, when temperatures stay mostly negative during winter, the ground freezes and a large amount of snow lies on the slope, no remarkable changes in deformation rates have been detected (Grøneng et al., 2011).

3 Theory

In this chapter, central theory regarding the topic under study and of importance for the analysis is presented. It includes a basic description of the different types of seismic waves, seismicity related to rockslides, detection of seismic events and the concept of single-station analysis for direction finding and event location.

3.1 Seismic waves

Seismic waves are elastic waves that propagate in the ground away from a seismic source, like an earthquake. Elastic waves are waves that cause reversible particle displacements of a rock, meaning that it will return to its initial positions when the waves have passed by. Two main classes of seismic waves exist: body waves and surface waves (Reynolds, 2011).

3.1.1 Body waves

Body waves are seismic waves that can propagate in the interior of the earth. They are further subdivided into two types: P-waves and S-waves. P-waves, sometimes also referred to as pressure waves/primary waves, are the waves that propagate through the earth with the highest velocity and are the first appearing waves in a seismogram record of an earthquake. The particle motions are parallel to the direction the waves propagate and can be described as switching compressional/dilatational motion (figure 4). P-waves are able to move through both fluids and solids (Reynolds, 2011).

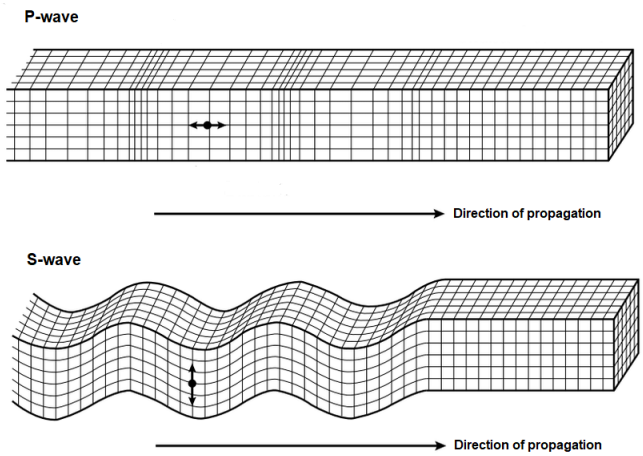

Figure 4: Illustration of P-wave and S-wave particle motions, adapted from Bolt (1982).

The other subclass of body waves has particle motions that are perpendicular to the direction of propagation (figure 4), and is called S-waves. Other usual names for these waves are shear-waves and secondary waves. If the particle motion is perpendicular to the propagation direction in a vertical plane only, the wave is called an SV-wave. A wave that has particle motion perpendicular to the travel direction in a horizontal plane only, is called a SH-wave.

Shear waves are limited to propagate only in solids, as fluids do not have any shear strength (Reynolds, 2011).

3.1.2 Surface waves

Surface waves are seismic waves that are travelling only near the earth's surface and are subdivided into two different types: Rayleigh waves and Love waves. The first type, Rayleigh waves, are waves that propagate with particle displacements in a vertical ellipse (figure 5) relative to the ground. Amplitudes of these waves are exponentially reduced with depth (Reynolds, 2011).

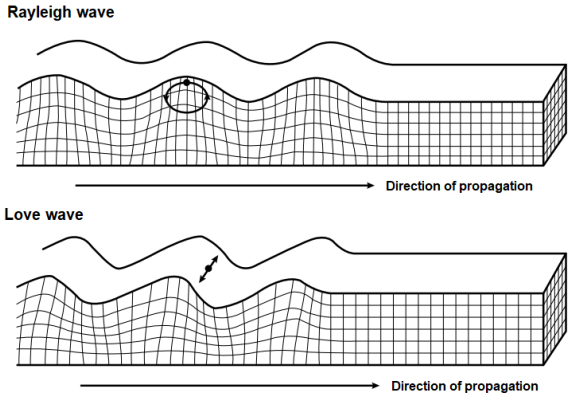

Figure 5: Illustration of Rayleigh wave and Love wave particle motions, adapted from Bolt (1982).

The second type of surface waves, Love waves, propagate with particle movements horizontal and perpendicular to the direction of propagation, as illustrated in figure 5. They can exist in the case where a material of high shear-wave velocity is lying under a material of lower shear-wave velocity. When surface waves propagate, different frequencies travel at different velocities and the waves change as they propagate. This is called dispersion (Reynolds, 2011).

3.2 Seismic sources related to rockslides

From the deformation processes taking place on a steep and unstable rockslope, such as the study site at Åknes, seismic energy can be generated from several possible sources. Breakage of rocks, rockfalls, flowing materials and fluid-triggered deformation are some of the processes that can possibly generate seismic energy (figure 6).

3.2.1 Rockfalls

Rockfalls are a very common phenomenon in steep rockslide areas. They are characterized by a rock mass travelling fast downwards through the free air, often in combination with some rolling and bouncing on the way down. In a rockfall with several blocks involved, there are little interaction between the different fragments (Varnes, 1978). The detachment of a rock volume

often happens where there are existing discontinuities and can be triggered by several different processes. Common processes leading to rockfalls are earthquakes, freeze-thaw processes and water flowing through discontinuities in the ground (Luckman, 2013). Rockfalls serve as a potential seismic source as seismic waves can be generated when the mass travels downslope and is in contact with the ground (Provost et al., 2018).

3.2.2 Rock breakage

Breakage of rocks and movements along existing discontinuities in the ground are processes that are likely to occur frequently on an unstable rockslope. It may be processes such as cracking and fracturing, or movements along a sliding surface. Cracking/fracturing on a rockslope is commonly caused by tensile forces acting on the material, as the material often has a weak tensile strength. In depth, rock breakage might also be caused by weathering (e.g. freeze-thaw processes), the weight of overlying materials and shaking of the ground. Along the sides and base of a rockslide, crushing and sliding (shearing) are thought to be dominating processes. From these processes seismic energy can be released (Provost et al., 2018).

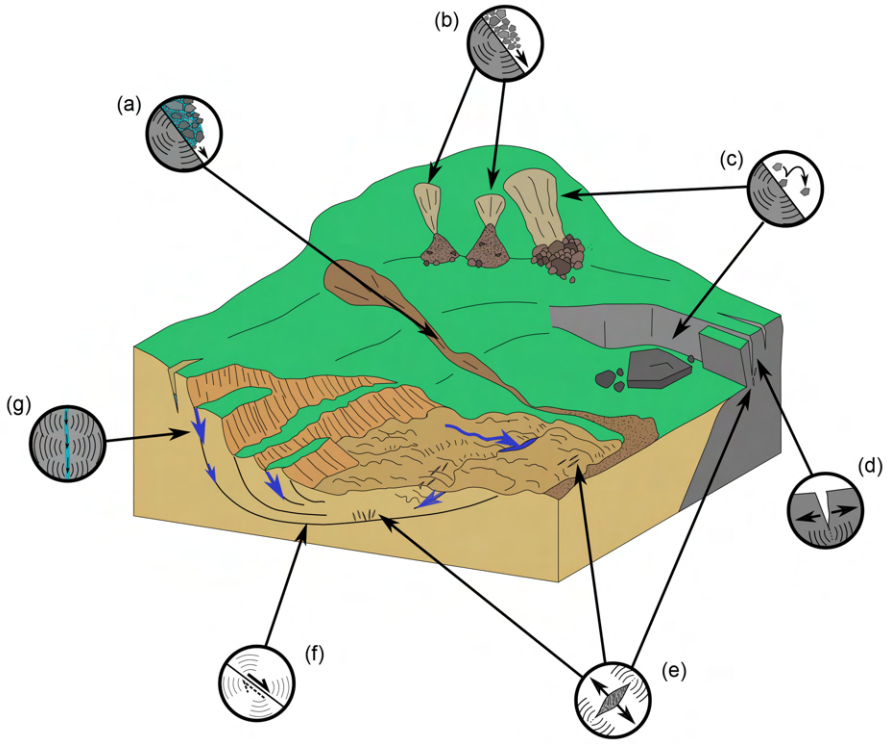

Figure 6: Illustration of processes related to rockslides that are possible seismic sources, from Provost et al. (2018). a) and b) illustrates wet and dry granular flows, respectively, c) shows the process of a rockfall, d) opening of fracture, e) opening of crack, f) movements along a sliding surface and g) illustrates fluid flows along discontinuities.

3.2.3 Flows

Another potential seimic source in a rockslide area is related to different types of mass flows. Such flows consist commonly of a combination of rock fragments, smaller grains and other types of loose material. Compared to rockfalls, there is more interaction between different rock fragments that the mass consists of. Fluids may also be involved and it is common to subdivide into dry and wet flows. As the mass flows downslope in contact with the ground, seismic energy might be generated. Seismic signals generated from these events are believed to be a combination of interaction between fragments within the mass flow and interaction with the ground, thus complex waveforms are commonly seen (Provost et al., 2018).

3.2.4 Fluid-triggered sources

Fluid flows may be an important process for generating seismic sources on a rockslope. Discontinuities on the slope might serve as a network for fluids to migrate in the ground. As fluids flow through the ground and the ground becomes saturated, an increase in pore pressure can possibly make the slope more unstable, for example along a sliding surface. This could lead to earthquakes and repetitive signals with harmonic waveforms being generated (Provost et al., 2018).

3.3 Seismic signals related to rockslides

Seismic signals related to active rockslopes and the origins of such events have been described in some previous studies, including Provost et al. (2018) and Tonnellier et al. (2013), where the aim has been to classify events based on the seismic signature with time and the frequency content. Provost et al. (2018) analysed seismic signals from several active rockslopes in order to find similarities in the data pointing towards a standard classification system. The seismic signature comprises features like duration, signal shape and frequency content. Their observations indicated three main types of seismic events found in such areas: 1) slopequakes, 2) granular flows and 3) rockfalls.

3.3.1 Slopequakes

Slopequakes are considered to be locally occuring events in the subsurface inside a rockslope. These are short lasting events with a duration of less than 10 seconds, commonly 1-5 seconds. First arrivals are generally emergent and therefore difficult to pick precisely (Tonnellier et al., 2013). The greatest amplitudes are often seen early after the signal onset. Highest frequencies are also usually seen in the first part of the signal, and a decay of high-frequency content with time is observed. The average frequency typically varies from about 10 Hz for low-frequency events to 20 Hz for high-frequency events. In cases where there is a significant contrast between the frequency content of early arrivals and later arrivals, the signal may be classified as a hybrid slopequake. Due to short source to receiver distances, different phase arrivals are difficult to separate, but they are believed to mainly consist of surface waves. Some phases could still possibly be identified in the waveforms, one could in some cases manage to pick P-waves in the high-frequency content at the signal onset. The origins of slopequakes are still not fully

understood, but investigations of these kinds of signals have suggested they originate from rock breakage (see section 3.2.2) such as movements along a sliding surface or cracking/fracturing (Provost et al., 2018). Examples of the waveforms of different types of slopequakes can be seen in figure 7.

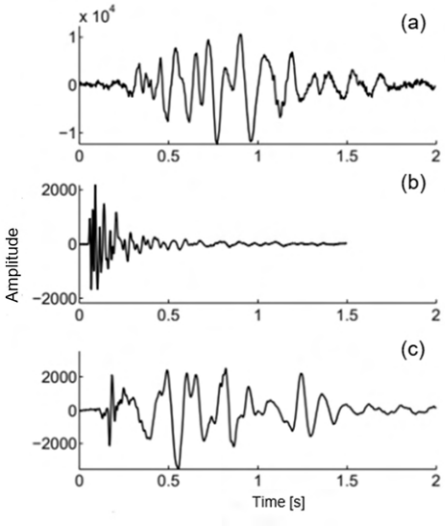

Figure 7: Examples of slopequakes from Provost et al. (2018): a) low-frequency slopequake, b) high-frequency slopequake, c) hybrid slopequake.

3.3.2 Granular flows

Granular flow events are relatively long lasting events. The duration varies from tens of seconds to tens of minutes, depending on the presence of fluids. If there are fluids involved, the signal duration is commonly more than ten minutes. A dry flow normally lasts shorter than ten minutes. In the seismogram, granular flow signals are typically seen as elongated and spindle-shaped waveforms (figure 8). A clear first arrival is difficult to identify as the onsets are commonly emergent. Similarly to slopequakes, arrivals of different seismic phases are very difficult to separate and in most cases not possible to visually detect in the waveform. Most of the energy is often seen around frequencies in the range 5-20 Hz, which naturally can depend on the distance from the event to the recording station. Less energy is commonly seen for frequencies below 5 Hz. If there are fluids involved, one might observe more energy around much higher frequencies. These signals originate from a combination of interactions within the mass flows and with the ground, see section 3.2.3 (Provost et al., 2018).

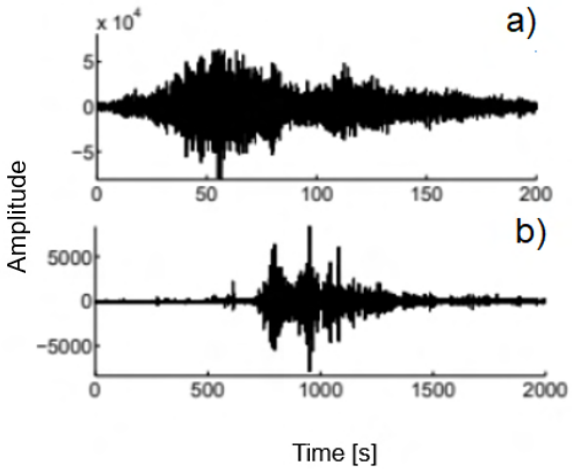

Figure 8: Examples of the seismic signature of granular flows from Provost et al. (2018): a) dry granular flow, b) wet granular flow.

3.3.3 Rockfalls

Rockfalls are in general seen as several contributions in the seismograms, from the multiple times a rock mass hits the ground (figure 9). Signals from several bumps may arrive at the station simultaneously, if there are a number of blocks involved. Their duration varies a lot, typically from a couple of seconds to tens of seconds. In addition to the distance from source to receiver, frequencies depend on the total rock mass, where more energy is seen around lower frequencies with increasing mass. Several high-energy areas are usually observed in the spectrogram of a rockfall. Different phase arrivals are difficult to identify and surface waves are mostly seen. Rockfalls are believed to be mainly triggered by freeze-thaw processes, earthquakes or by fluids flowing through discontinuities in the ground, see section 3.2.1 (Luckman, 2013).

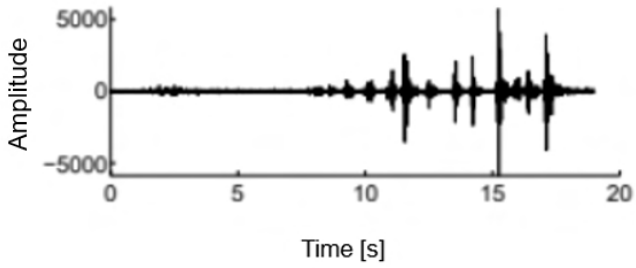

Figure 9: Example of a typical seismic recording of a rockfall, from Provost et al. (2018). Several spikes are clearly seen in the waveform, related to the multiple times a rock mass hits the ground.

3.4 Seismic event detection

3.4.1 STA/LTA event detection

One way to investigate possible seismic events in a large amount of data, is to use a short-term average (STA) over long-term average (LTA) trigger algorithm. A STA/LTA algorithm calculates the average of amplitudes of a moving short time window and a longer time window. The ratio is determined and every time it exceeds a given threshold level, an event is registered. A seismic event does not necessarily have very high amplitudes and may be difficult to see at first sight, hence such an algorithm could provide helpful information regarding possible events. Figure 10 illustrates a classic alignment of the two windows, where the calculations are performed for the index at the boundary between them.

Figure 10: Classic alignment of STA/LTA windows.

The STA and LTA values are determined according to equation 1 and 2:

$$STA(i) = \frac{1}{M} \sum_{j=i}^{i+M} a_i^2 \tag{1}$$

$$LTA(i) = \frac{1}{N} \sum_{j=i-N}^{i} a_i^2 \tag{2}$$

where M is the number of sampling points in the STA-window, N is the number of sampling points in the LTA-window and a_i is the amplitude at sampling point i (Trnkoczy, 1999).

Four different parameters are of importance for the algorithm: 1) length of STA time window, 2) length of LTA time window, 3) trigger threshold, 4) detrigger threshold. 1) and 2) are lengths of the time windows given in seconds. 3) is the value of the STA/LTA ratio that must be exceeded for an event to be registered. When the ratio exceeds the trigger threshold level for a time sample point, an event is registered at that time. 4) marks the end of an event if the STA/LTA ratio becomes smaller than this value.

These are important parameters because they will affect what types of signals, as well as the number of events one will find in the data. When setting the length of the STA-window one

should take into account the dominant frequencies (periods) of an event of interest, as the window length needs to be longer than a couple of periods. A short STA-window will normally increase the detection of local events of short duration, while choosing a longer window will be better for long duration distant events. The basic idea of a LTA calculation is that it should represent an estimate of the average background noise level, so one should ideally have some information on the expected noise content. By choosing a very small LTA-window some events will perhaps not be triggered, due to a quick change of the LTA value, because the ratio remains small even though the STA average is high. Oppositely, a very long LTA window might not sense variations in the noise level, which could result in unwanted triggers (Trnkoczy, 1999).

Setting an appropriate trigger threshold value is not an easy task, because it is a balance between the desired seismic events that will be detected and the number of unwanted (false) triggers in the record. A high value will normally decrease the number of unwanted triggers and might be a good choice if the targets are very strong events. Oppositely, a lower trigger threshold level is more suitable for detection of lower amplitude events, but more unwanted triggers will probably appear in the record.

One should also take into account the level of noise at the study site, when deciding on the trigger threshold. A relatively flat and predictable noise level will allow for a lower value. In such a setting, with little noise variations from human activity, a typical threshold value is 4. Sites where the seismic recordings are influenced by much human activity would require a higher threshold. The detrigger threshold level will decide how much of the decaying part of an event that will be recorded. Setting a low value could be preferable for catching more of the decay, but it could also give unwanted long recordings such as in the case of a rapid change in the noise level. A common threshold is 2 if the noise levels are not very high (Trnkoczy, 1999).

3.4.2 Cross-correlation

The concept of cross-correlation is a common approach to estimate the similarity between two time series, and can be a useful tool in order to track a long continuous seismic record for shorter lasting events (Holland, 2013). The sum of the dot product between two vectors is the basis for the method, given by:

$$C_{ab} = \sum_{i=0}^{N-1} a_i b_i \tag{3}$$

where C_{ab} is the correlation coefficient, N is the number of sampling points, a_i is the value at sampling point i for vector a and b_i is the value at sampling point i for vector b (Derrick et al., 2004).

By shifting one signal along the other signal, one can find the relative alignment between the two where the similarity is maximized. Often the shift is referred to as the lag between the two signals. The equation is then simply given by:

$$C_{ab}(\tau) = \sum_{i=0}^{N-1} a_i b_{i-\tau} \tag{4}$$

where τ is the lag between the two signals (Derrick et al., 2004).

A challenge with the expression above (equation 4) is that it could be difficult to interpret and compare different results because the correlation coefficient will be influenced by the units of the two data series. Therefore, it is common to use a normalized version of the expression which will make the result independent of units. To get a normalized version of the cross-correlation coefficient it is common to first find the autocorrelation of the two data series. An autocorrelation is the cross-correlation of a vector with itself. Then, the square root of the autocorrelations is found and multiplied together. Finally, the cross-correlation coefficient as found in equation 4 is divided by this product to normalize. Equation 5 describes the relationship:

$$\rho_{ab}(\tau) = \frac{C_{ab}(\tau)}{\sqrt{C_{aa}(0)}\sqrt{C_{bb}(0)}} \tag{5}$$

where τ is the lag, $\rho_{ab}(\tau)$ is the normalized cross-correlation, $C_{ab}(\tau)$ is the cross-correlation as found in equation 4, $C_{aa}(0)$ is the autocorrelation of vector a and $C_{bb}(0)$ is the autocorrelation of vector b.

The advantage of this normalized version of cross-correlation is that one will never get a value that is greater than 1, since the factor below the fraction line will always be the greatest. Thus, it could be easier to compare cross-correlation coefficients. In a last step it could be a good idea to remove the mean of the two vectors. By doing this one will get negative values only when the data series have an opposite relation (Derrick et al., 2004). The expression for the cross-correlation is then given by:

$$\rho_{ab}(\tau) = \frac{\sum_{i=0}^{N-1}(a_i - \overline{a}) * (b_{i-\tau} - \overline{b})}{\sqrt{\sum_{i=0}^{N-1}(a_i - \overline{a})^2}\sqrt{\sum_{i=0}^{N-1}(b_{i-\tau} - \overline{b})^2}} \tag{6}$$

where $\rho_{ab}(\tau)$ is the cross-correlation coefficient, a_i is the value at sampling point i for vector a, b_i is the value at sampling point i for vector b, $\overline{a}$ is the average of vector a, $\overline{b}$ is the average of vector b, N is the number of sampling points and τ is the lag. The equation (equation 6) is a much used version for cross-correlation, and is known as the Pearson Product-Moment correlation (Derrick et al., 2004).

3.5 Direction finding and location using a single-station

The locations of seismic events are usually determined by using arrivals from a network of many stations, but one three-component station may also in some cases be used to estimate source directions and even locations (Havskov et al., 2011).

3.5.1 P-wave first arrival analysis

To estimate source directions from a single-station record one can use P-wave first arrivals and exploit that P-waves are linearly polarized in the direction of propagation. A P-wave propagating upwards from a source is linearly polarized in a vertical plane, hence the particle motion can be observed on a component aligned in the source direction (radial) and on a vertical component. On the basis of this, one might be able to find the back-azimuth to a seismic source, which is the angle relative to north (clockwise) from the seismometer to the source. The east and north component of a seismogram can be utilized to find the radial direction. It can be estimated by using the recordings of the first arrival of the P-wave on the east and north components and the following relationship:

$$AZI = arctan(\frac{A_E}{A_N}) \tag{7}$$

where AZI is the direction of particle displacement, A_E is the amplitude measured on the east component and A_N is the amplitude measured on the north component.

The estimated direction of particle displacement from equation 7 gives a 180° uncertainty for the back-azimuth (BAZ). This is because the amplitude of the first arrival on the Z-component can be positive or negative. When it is negative (down), the calculated direction from the horizontal components is in the direction of the source. Oppositely, when it is positive (up), it is away from the source and the back-azimuth is in a 180° different direction. Figure 11, from Havskov et al. (2011), shows an illustration of the case.

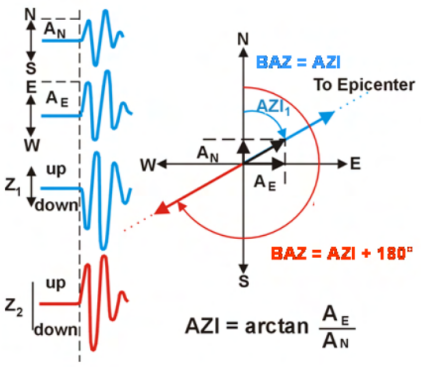

Figure 11: Illustration of back-azimuth estimation from P-wave first arrival, from Havskov et al. (2011). First motions on the three components are seen to the left. Associated back-azimuths (BAZ) are given to the right, which can be determined from equation 7.

3.5.2 Estimation of source distance from S-P arrival times

It might also be possible to find the distance to seismic sources from single-station recordings. If one is able to identify first arrivals of both P- and S-waves, one can make use of the difference in arrival times to estimate the distance. This method requires not only a precise pick of the two phases, but also information on the P- and S-wave velocities. When using constant P- and S-wave velocities, one can express the arrival times by the following relationship:

$$t_P = t_0 + \frac{d}{V_P} \tag{8}$$

$$t_S = t_0 + \frac{d}{V_S} \tag{9}$$

where t_P is the arrival time of the P-wave, t_S is the arrival time of the S-wave, V_P is the P-wave velocity, V_S is the S-wave velocity, t_0 is the event time and d is the distance to the source.

By combining equation 8 and 9 and solving for d, the source distance can be expressed as:

$$d = (t_S - t_P)\frac{V_P V_S}{V_P - V_S} \tag{10}$$

This only applies for direct P- and S-waves propagating in the crust if V_P/V_S is constant (Havskov et al., 2011).

3.5.3 Back-azimuth estimation by rotation from ZNE to ZRT system through all angles

Back-azimuths may be estimated by rotation of a wave from the ZNE-system (vertical, north, east) to the ZRT-system (vertical, radial, transverse), where the radial component will be aligned with the source direction. Since both P-waves and Rayleigh waves will show particle motions in a vertical plane from the source to receiver, they might both be used to estimate back-azimuths. One way to do this is to rotate the waveforms from the ZNE-system to the ZRT-system and determine the direction with respect to north that gives most energy on the radial component. Another way is to find the direction that gives the best correlation between the radial component and the vertical component. If using Rayleigh waves, a phase shift of 90° must be taken into consideration, between these components (Köhler et al., 2019). The rotation from ZNE-components to ZRT-components is performed by taking the product of the NE-components and a rotation matrix:

$$r = \begin{bmatrix} cos(i) & sin(i) \\ -sin(i) & cos(i) \end{bmatrix} \tag{11}$$

$$\begin{bmatrix} R \\ T \end{bmatrix} = \quad r \begin{bmatrix} N \\ E \end{bmatrix} \tag{12}$$

where r is the rotation matrix and i is the angle clockwise from north.

4 Data and software

4.1 Seismological data

Seismological data recorded by the broadband seismometer (AKN) at Åknes have been analysed in this project. It is a three-component (vertical, north and east) permanent seismic station on the slope, which was installed and has been operated by NORSAR since November 2009. Data are recorded at a sampling rate of 200 Hz, which gives a Nyquist frequency of 100 Hz. The Nyquist frequency is half of the sampling rate and the highest frequency a signal can contain to still be fully recovered. A lower corner period of 60s makes the instrument capable of sensing frequencies in the range 0.0167-100 Hz. Figure 12 shows the position of AKN on the slope at an altitude of 508 m.a.s.l., and the position of the geophone network (762-862 m.a.s.l.).

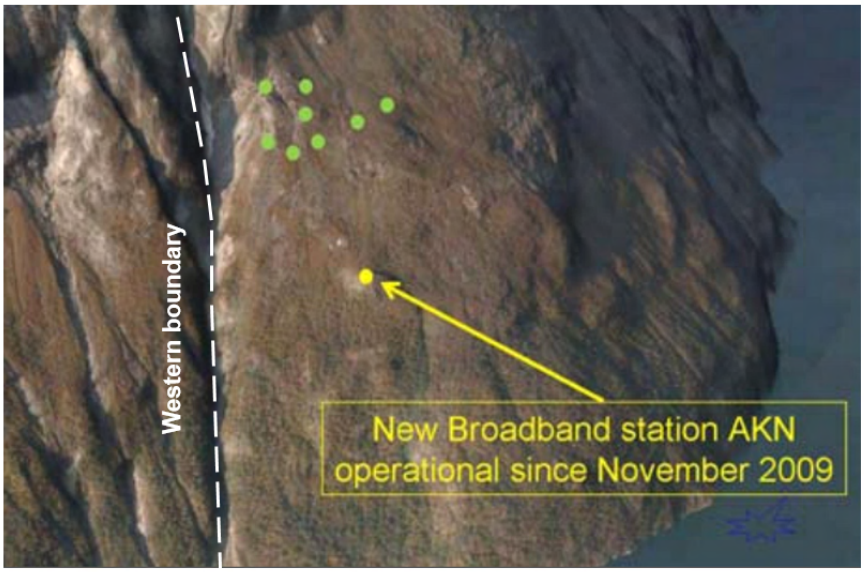

Figure 12: Location of the broadband station (AKN) and the geophone network (green points) on the slope, from Roth and Blikra (2010).

The acquired data are hosted at the University of Bergen (UiB) and made available with open access through the webpage www.orfeus-eu.org. ORFEUS is a foundation for organizing seismological data gathered in the European-Mediterranean region and making it digitally available. Data are downloaded in miniSEED format. SEED is short for Standard for the Exchange of Earthquake Data and is a data format containing seismological time series data and metadata. The miniSEED format contains time series data, but limited of the belonging metadata stored in the full SEED format, hence it is more suitable for processing. A total of three and a half months of data from 01.03.20 to 15.06.20 were gathered from ORFEUS and used for analysis. An example of one hour of raw data recorded by AKN is given in figure 13.

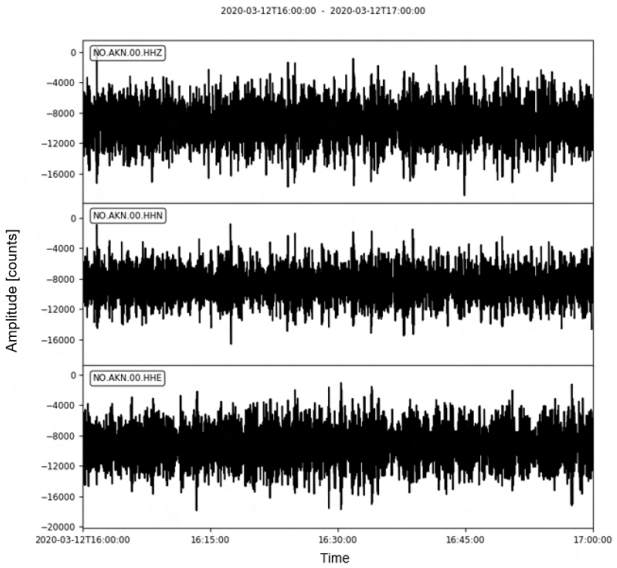

Figure 13: Example of one hour of raw data recorded by AKN on 12.03.20, for all three components (Z,N,E).

4.2 Meteorological data

Meteorological data provided by NVE, measured at the station installed 900 m.a.s.l., were used in this study. The data contains hourly recordings of meteorological parameters. Three and a half months of temperature and precipitation measurements were gathered and analysed for the period 01.03.20 to 15.06.20.

4.3 Software

All data were processed and analysed using the programming language Python. Different frameworks built for manipulation and processing of data in Python were utilized. Obspy is a framework developed for seismology, and were used to process and manipulate seismological data of the miniSEED files. It is a powerful tool for analysis in both the frequency domain and time domain. CSV files of meterological data were read in and manipulated using the data analysis framework Pandas. Numpy and Matplotlib are other Python packages that were utilized for mathematical operations and to create figures, respectively.

5 Methodology

In this chapter, the methods used for the analysis of microseismic events are presented. The workflows regarding event detection, classification and polarization analysis are given.

5.1 STA/LTA event detection

Considering the large amount of data and the continuous seismic record of both events and seismic noise, it was decided to run a short-term average (STA) over long-term average (LTA) trigger algorithm (described more in detail under section 3.4.1) to get an overview of the potential events. A Python script working with the Obspy implementation of the classic STA/LTA algorithm was utilized, and run through the period. Each step of the algorithm is described in the following sections.

Setting STA/LTA parameters

First, the time window lengths and threshold levels were determined to be as following:

Length of STA-window: 0.5 s

Length of LTA-window: 15 s

Trigger threshold value: 6

Detrigger threshold value: 2

A STA-window of 0.5 seconds was chosen by taking into account the duration of an expected local event, which could be as short as 1 second or even shorter. The LTA-window was set to have a medium length of 15 seconds, which might be long enough to give a fair estimate of the noise level and also short enough to maybe sense variations in the noise levels. The trigger threshold of 6 seemed like a fair value considering both the wanted targets and expected noise levels. Local events may not show great amplitudes, so a very high threshold could lead to many missed events. There are no clear indications of very high noise levels at the study site, but to try to not get too many false detections, a very low threshold value was also avoided. A relatively low detrigger threshold of 2 was set in order to record much of the decaying tail (coda) expected to be seen in local slopequake events. Some random days of data were chosen to test the algorithm, and the mentioned thresholds and time windows seemed to give fair results. Trigger values between 3 and 8 and detrigger values between 2 and 4 were tested.

Processing steps and STA/LTA calculations

After deciding on the trigger/detrigger thresholds and time windows, a file where the results could be saved in was defined to contain information about the onset times and durations. In a next step, one day of continuous data was loaded in and some processing of the raw data was performed. First, demean was applied. This process removes the mean of the signal and the result is that the data is centered close to zero (figure 14).

Bandpass filtering was also performed in order to fit the data to what is believed to be the main frequency range of desired events. A Butterworth bandpass filter with a lower frequency of 2 Hz and an upper frequency of 60 Hz was used, considering that events of interest for the slope monitoring are likely to have their main frequency content within this range (Provost et al., 2018). Figure 15 shows an example of a seismogram before and after bandpass filtering is applied.

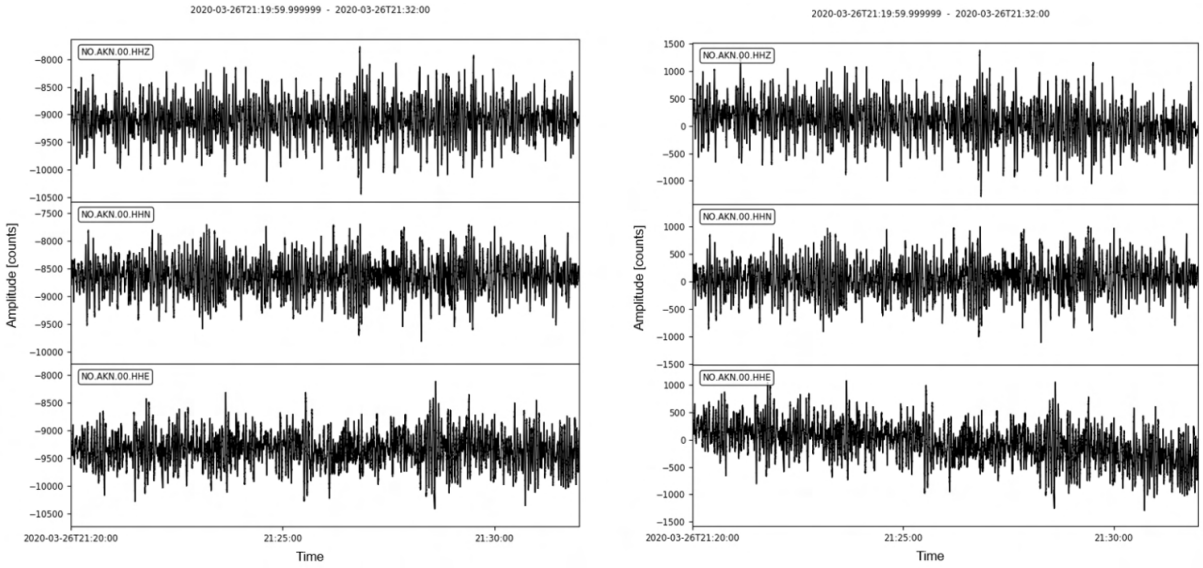

Figure 14: Example of 12 minutes of recorded data before (left) and after (right) demean is applied.

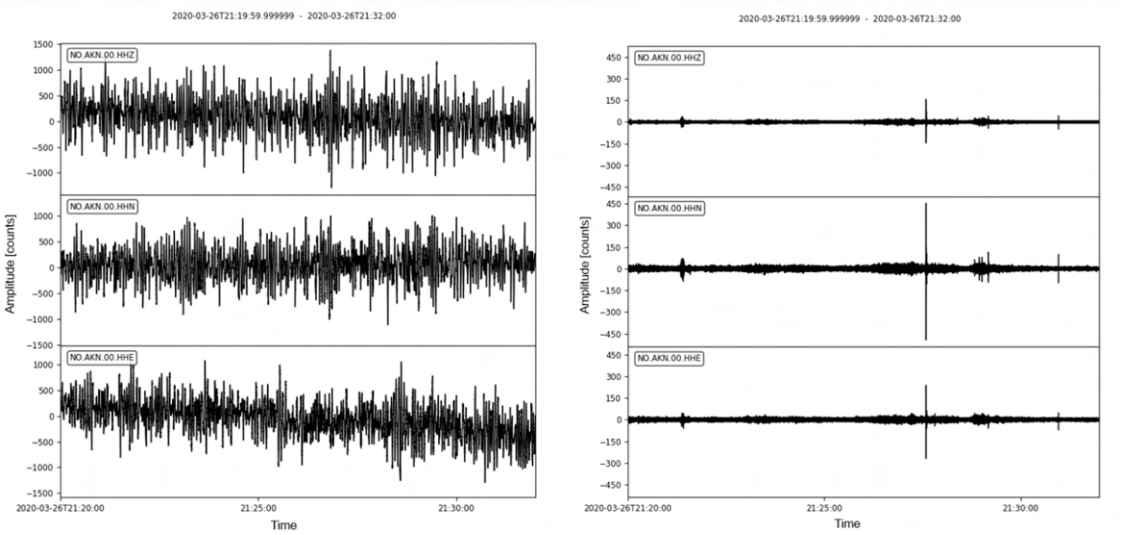

Figure 15: Example of data after demean is applied, before (left) and after (right) bandpass filtering. Several possible microseismic events can now be observed.

Further, after some simple processing of the raw data was performed, the STA/LTA calculations were carried out. It was done by using the classic STA/LTA approach, where the short-term average and long-term average amplitude values are calculated as given by equation 1 and 2 (see section 3.4.1). The STA/LTA ratio was calculated for all three components individually and an event was registered every time the given trigger threshold was exceeded on all three components. It was done for one day at a time for the period from 01.03.20 to 15.06.20. The alignment of the STA- and LTA-windows, the same as in figure 10, gives some sample points at the start of each day where the long-term average can not be calculated. For these sample points the average of the signal was used for the LTA value.

An example of a possible microseismic event detected by the method can be seen in figure 16. It shows an event that has been triggered on the vertical component. In the lower part of the figure the calculated STA/LTA ratio versus time is given, while the corresponding seismogram is seen above. Red and blue vertical lines in the seismogram mark the start and end of the trigger as the ratio exceeds 6 and goes below 2, respectively. The horizontal stipled lines are plotted where the ratio is 2 and 6. A rapid increase in the amplitude ratio can be observed at the trigger onset.

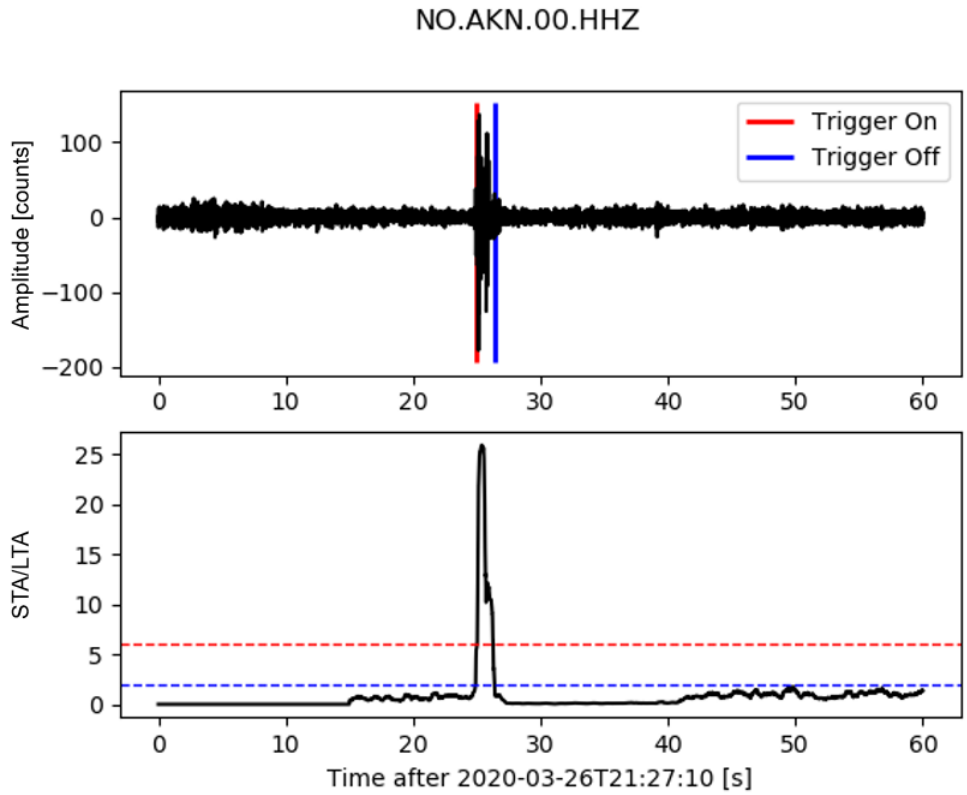

Figure 16: Example of an event detected by running the STA/LTA trigger algorithm. Upper part: seismogram of the vertical component. Red and blue vertical lines mark the start and end of the trigger, respectively. Lower part: calculated STA/LTA ratio versus time. Stipled red and blue lines are plotted at STA/LTA = 6 and STA/LTA = 2.

5.2 Event classification

In order to determine different event classes, the STA/LTA record was first visually inspected. The process of determining different microseismic event classes from the STA/LTA record was very challenging, and much time was spent finding several events that were similar enough to be defined under the same class. After visual inspection and analysis of the waveforms in both the frequency domain and time domain, together with comparison with signals found in previous studies (Provost et al., 2018, Tonnellier et al., 2013), three main classes of events were eventually determined: 1) hybrid slopequakes, 2) low-frequency slopequakes, 3) rockfalls. Event class 1 was further divided into two subclasses, hybrid slopequakes (I) and hybrid slopequakes (II) (figure 17).

Several features were analysed to distinguish between different types of signals and classify them. The signal onset (impulsive or emergent), waveform shape, frequency content and duration were taking into account. To analyse the frequency content, spectrograms and plots of the power spectral density (PSD) were produced using available functions in Obspy. A spectrogram of a signal displays the energy at different frequencies and how it changes with time. The power spectral density (PSD) shows the power distribution for different frequencies in a signal and is measured in decibels per hertz (dB/Hz).

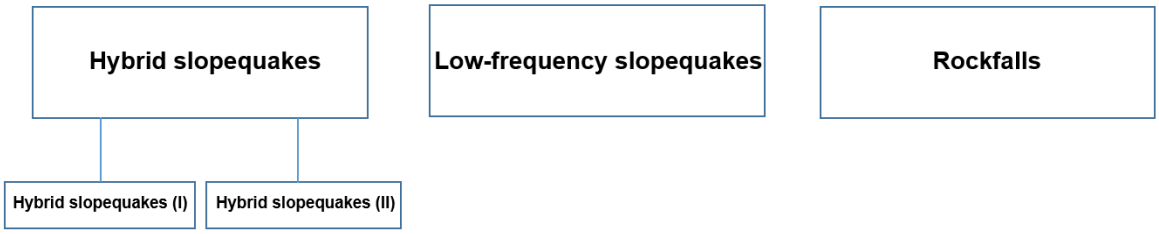

Figure 17: Overview of event classes.

5.2.1 Event class 1: hybrid slopequakes

Hybrid slopequakes (I)

Figure 18.a shows the seismogram of an event of the first subclass in event class 1. It shows a duration of about 3 seconds. More generally, these types of signals are seen with a duration of 1-5 seconds in the recorded data. The waveform shape is characterized by largest amplitudes in the first part of the signal, before a decay is seen towards the signal end. First arrivals are emergent and an accurate onset is difficult to determine. It is not possible to visually distinguish between different phase arrivals.

Spectrograms and PSD for all three components are shown in figure 18.b. Most energy is found around and below 10 Hz, as illustrated by the bright areas in the spectrograms and by one major peak in the PSD plots, but some energy is also present for higher frequencies up to about 40 Hz at the beginning of the signal. There is a significant contrast between dominating frequencies of early and later arrivals. Based on these features and the classification of similar signals proposed by Provost et al. (2018) and Tonnellier et al. (2013), the waveform has been classified as a hybrid slopequake and the event class will in the following be referred to as the hybrid slopequakes (I) class.

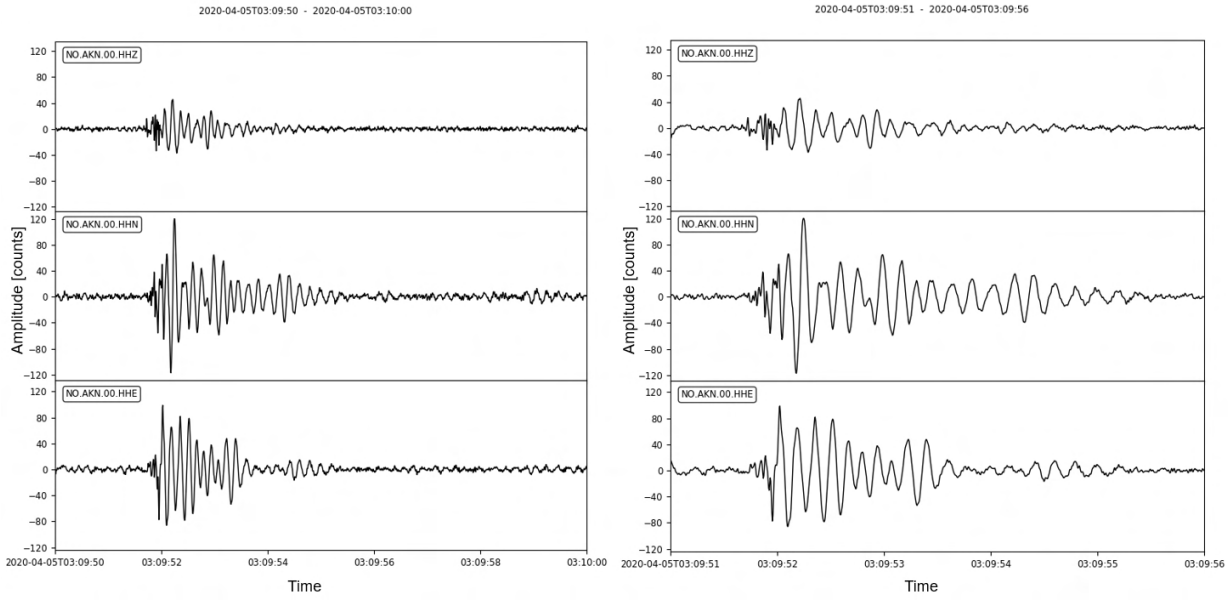

(a)

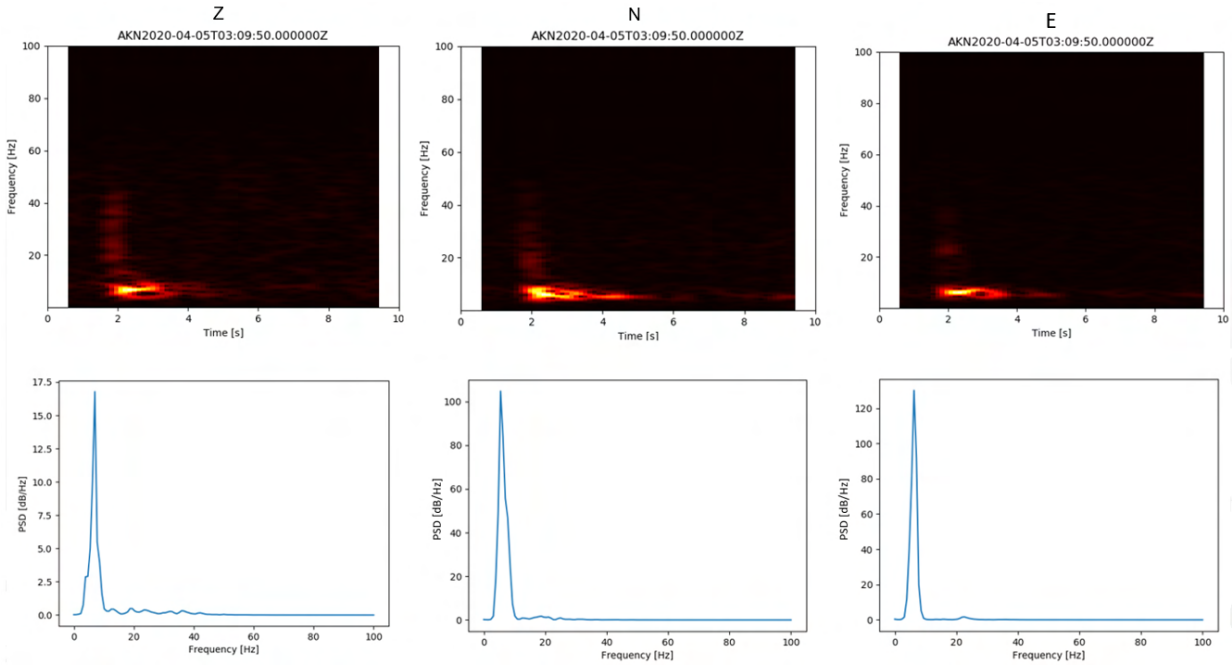

(b)

Figure 18: Example of event in the hybrid slopequakes (I) class. a) Left: seismogram of the event in a time window of 10 seconds. Right: seismogram of the event in a time window of 5 seconds. b) Spectrogram (top) and power spectral density (PSD)(bottom) corresponding to the time window of 10 seconds. From left to right: Z-component, N-component and E-component.

Hybrid slopequakes (II)

In figure 19.a one can see the seismogram of an event of the second subclass in event class 1. The duration is about 2 seconds. Other observations show that the duration of these types of signals varies from 1-4 seconds in the AKN record. It shows a similar waveform shape as events in the hybrid slopequakes (I) class (figure 18). Largest amplitudes are seen early after the signal onset, before a decay is observed with time towards the end of the event. First arrivals are commonly emergent and it is difficult to determine the exact signal onset and to visually distinguish between different phase arrivals.

Figure 19.b shows the spectrograms and PSD for all components. It shows highest frequencies in the first part, up to about 40 Hz. Less high-frequency content is seen with time and there is a significant contrast between dominating frequencies of early and later arrivals. Two areas of high energy can be observed from the spectrograms and PSD plots, at about 10 Hz and 20 Hz. Compared to the hybrid slopequakes (I) class, much more energy is seen above 10 Hz. Based on these characteristics and studies of similar waveforms by Provost et al. (2018) and Tonnellier et al. (2013), these kind of signals have been classified as hybrid slopequakes, but as another type than the event seen in figure 18. It will in the following be referred to as the hybrid slopequakes (II) class.

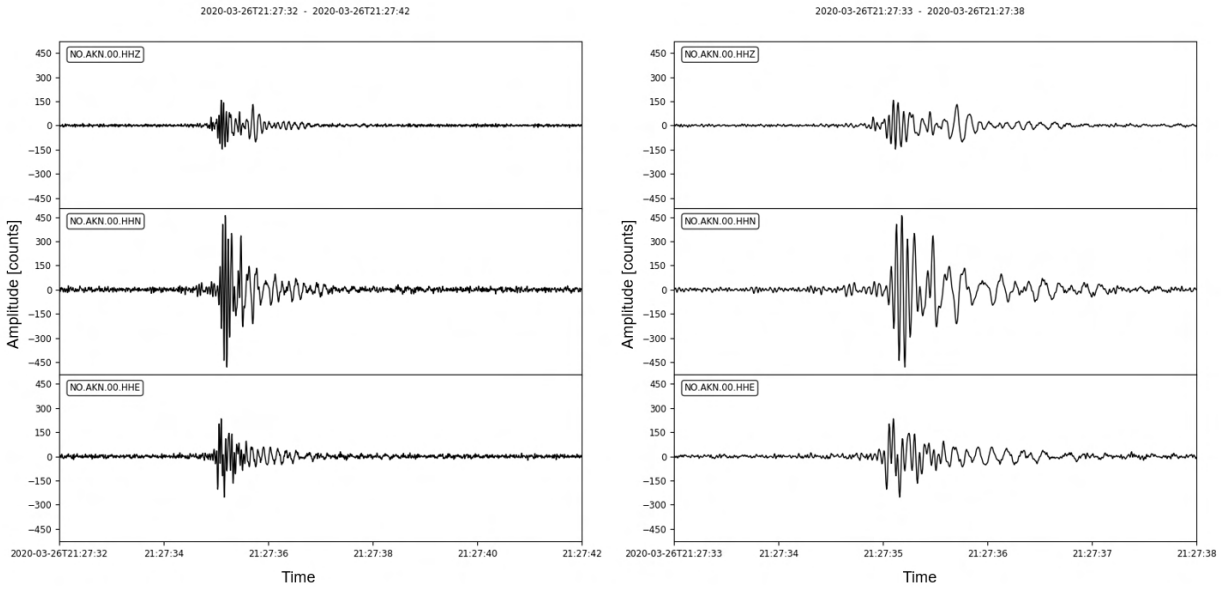

(a)

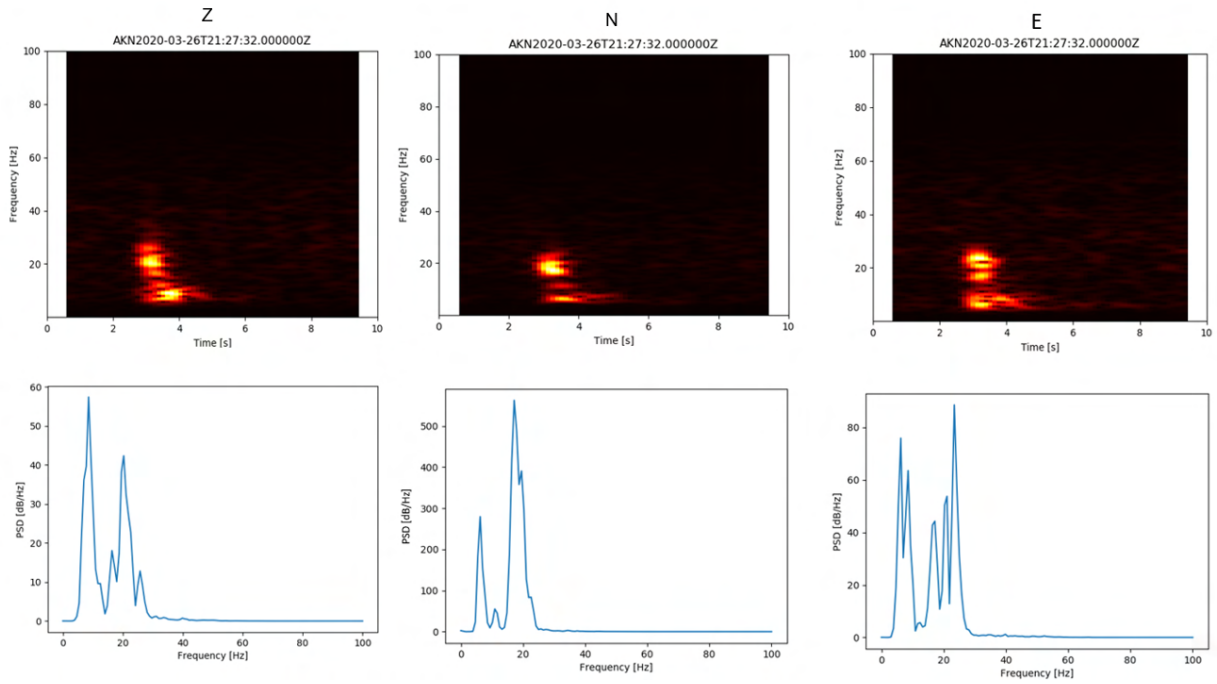

(b)

Figure 19: Example of an event in the hybrid slopequakes (II) class. See description of figure 18.

5.2.2 Event class 2: low-frequency slopequakes

The STA/LTA record also revealed a significant amount of pyramidal shaped events of relatively low frequencies, which has been defined as an own event class. Figure 20.a shows the seismogram of an event in this class. The event lasts for approximately 1.5 seconds. Other observations indicate, as similar to the hybrid slopequakes, a duration of less than 5 seconds and typically 1-3 seconds. It has a pyramidal shape where the greatest amplitudes are seen around the middle of the signal. The exact first arrival and different phase arrivals are difficult to determine.

Spectrograms and PSD for all three components are seen in figure 20.b. It shows mainly frequencies in a narrow range below 10 Hz (5-10 Hz) and small variations in the frequency content with time. Based on these features and by comparing with the descriptions of similar waveforms from Tonnellier et al. (2013) and Provost et al. (2018), these types of events have been classified as low-frequency slopequakes.

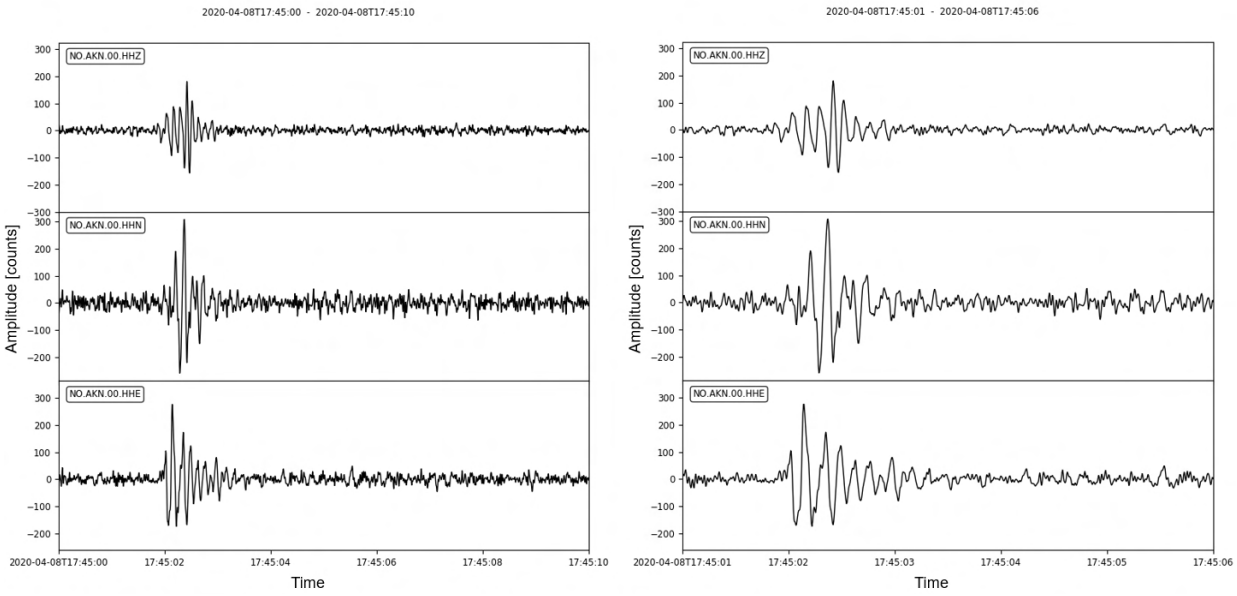

(a)

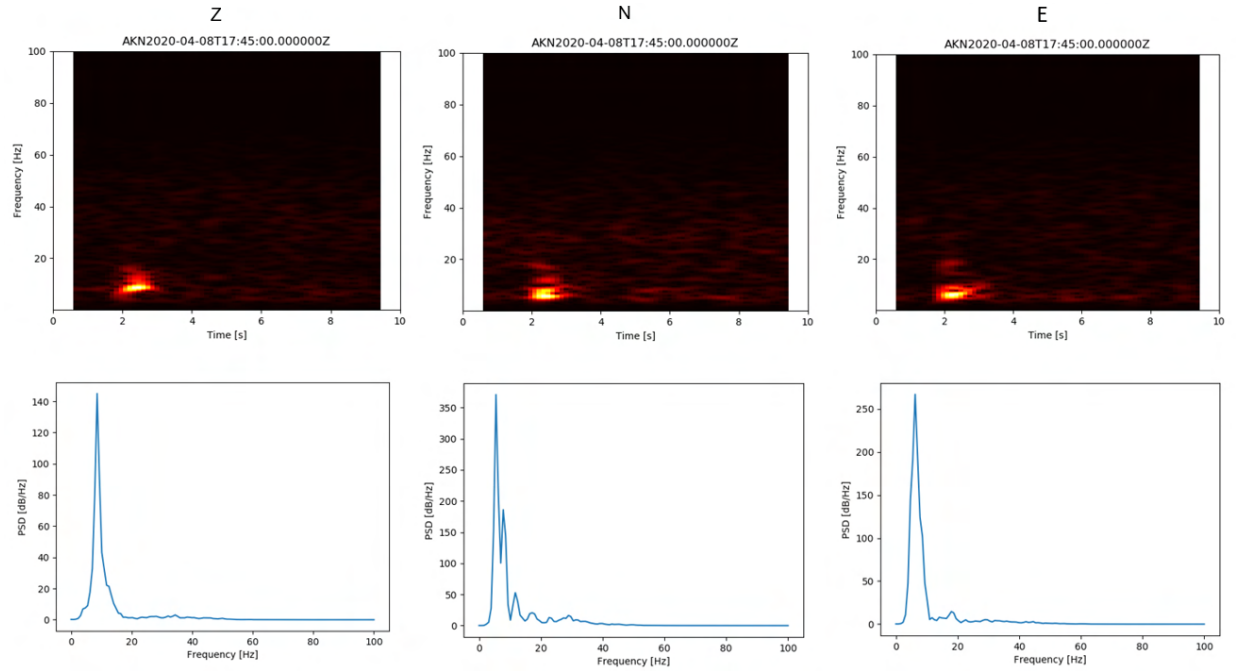

(b)

Figure 20: Example of an event in the low-frequency slopequakes class. See description of figure 18.

5.2.3 Event class 3: rockfalls

Figure 21.a shows the seismogram of an event in event class 3. A duration of about 10 seconds can be observed. Observations of a few other similar signals showed that the duration of these types of events varies more than for the other classes, from a few seconds to tens of seconds. The signal shape is more alternating compared to events in the other classes, with several spikes seen in the waveform. It may imply that the seismic signature is a result of several impacts. First arrivals are emergent and it is difficult to determine the exact onset of the event and to separate different phase arrivals.

Spectrograms and PSD for all three components are given in figure 21.b. Several areas of high energy are seen in the spectrograms. Most energy is observed for frequencies around 10 Hz through the signal. Some smaller amounts of energy are observed for higher frequencies up to about 50 Hz. Based on these characteristics and the event classifications proposed by Tonnellier et al. (2013) and Provost et al. (2018), the waveform has been classified as a rockfall.

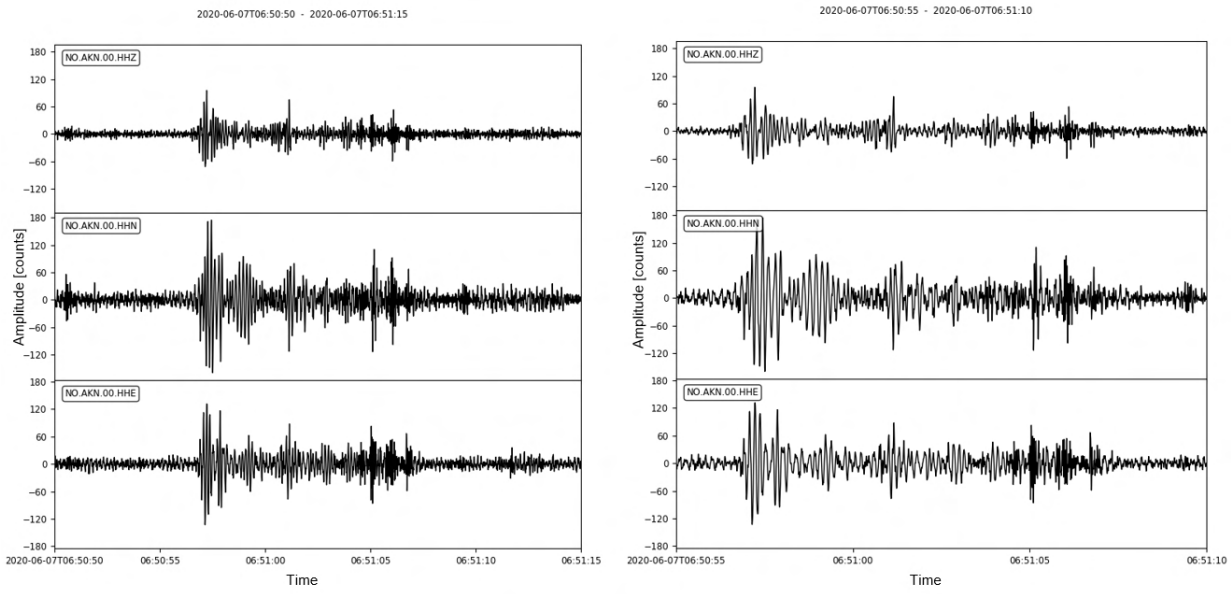

(a)

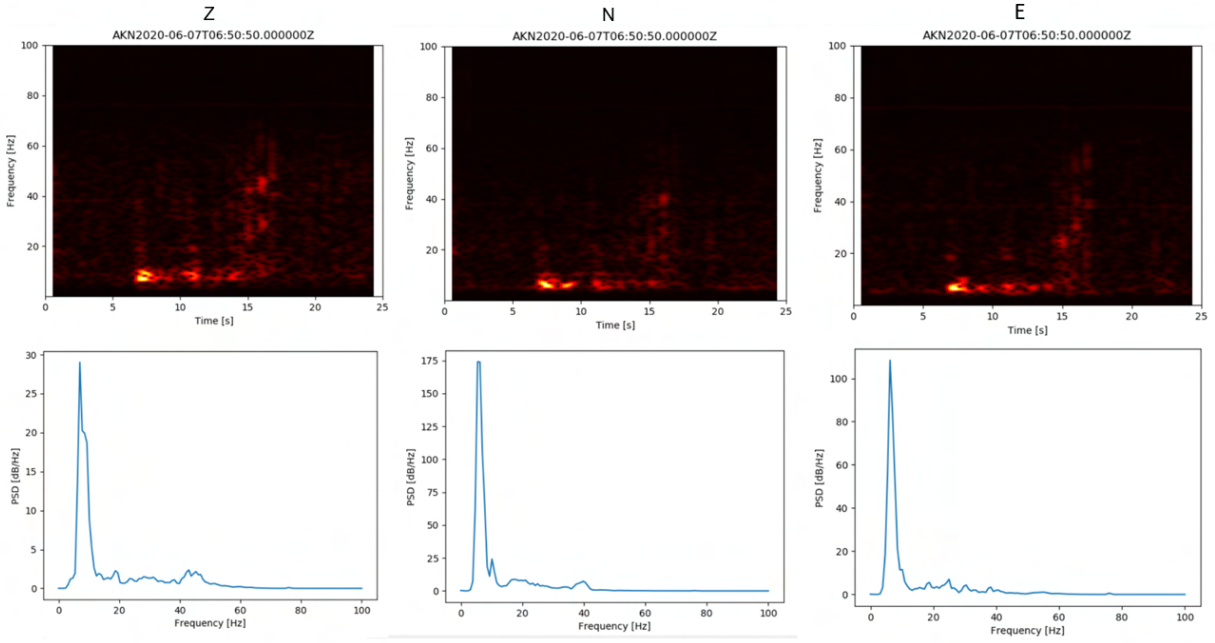

(b)

Figure 21: Example of an event in the rockfalls class. See description of figure 18. Time windows of seismograms are 25 (left) and 15 seconds (right). Spectrogram and PSD correspond to the 25 seconds time window.

5.3 Template event cross-correlation

To track the continuous seismic record for similar events as described under section 5.2, a Python program which uses a template event cross-correlation algorithm was run through the data for the period 01.03.20-15.06.20. Holland (2013) developed a script for cross-correlation of short duration seismic events with a longer continuous record, which has been utilized in this study together with the Obspy implementation. The idea of this approach is to use template waveforms for cross-correlation with a longer dataseries in order to detect the time sample points where a given threshold for similarity (cross-correlation coefficient) is exceeded. A Pearson normalized cross-correlation algorithm is used in the script, as described earlier in section 3.4.2. After some initial tests of the method it was found that events in two of the three main classes were suitable for the method. Both types of signals in event class 1 (hybrid slopequakes) and the signal type in event class 2 (low-frequency slopequakes) were found appropriate for template event cross-correlation. For events in event class 3 (rockfalls), initial tests showed difficulties in detecting waveforms with sufficient similarities. It could be due to a more variable duration and complex waveform for these types of signals. Based on this, it was decided to use only the events in class 1 and 2. The events used as template waveforms are those seen in figure 18 (hybrid slopequakes (I)), figure 19 (hybrid slopequakes (II)) and figure 20 (low-frequency slopequakes). Each step of the method is given in the following.

Setting cross-correlation thresholds and time windows for template events

The first step, before running the algorithm through the continuous record, was to decide on the appropriate thresholds (cross-correlation coefficients) for the similarity between the template events and the data that is being tracked for similar events. It is very important to have a good calibration of this parameter, as it will decide the number of correlations one will find. By setting a very low cross-correlation threshold one might get a lot of false detections, but on the other hand may avoid missing possible related events. A very high threshold may give a better estimate of the number of correlations that are actually associated signals, but one might risk to miss a lot of events. Therefore, to get as reliable results as possible, it is crucial to set suitable values for the cross-correlation coefficients. In addition, the time windows chosen for the template events will affect the amount of correlations. As different event types may require different threshold values and time window lengths, it can be a pitfall to use the same for all event types. It might be difficult to set these parameters only by looking at the signals, so it is preferable to do some initial testing on a smaller amount of the dataset in order to get a good calibration. Therefore, to see if the method was suitable at all for the dataset and to find appropriate parameters, it was first tested on some random days of data from the time period.

After testing the method on several days of data, it was verified that it was rather suitable for the detection of events in the hybrid slopequakes classes and the low-frequency slopequakes class, as it was possible to detect several events with a high degree of similarity to the template events. The time windows for the templates were decided to start from the registered STA/LTA event time. From this onset it was used a window of 1.5 seconds for hybrid slopequakes and 1.2 seconds for the low-frequency slopequake. The time window lengths were determined in order to include important parts of the different signals, both the onsets and decaying parts (codas). It

was also considered to be fair values based on observations of the common durations of the different events.

To decide on the cross-correlation coefficient thresholds, events with different correlation values to the template waveforms were visually inspected. In figure 22, the low-frequency slopequake template event and five detected events with different correlation coefficents are seen. It shows correlation values ranging from 0.51 to 0.75 and a high degree of similarity down to about 0.65. Thus, the cross-correlation threshold was set to 0.65 for the low-frequency slopequakes class. The same testing was done for the hybrid slopequakes (I) and hybrid slopequakes (II) template events. Appendix A (figure 43 and figure 44) shows these templates and the time windows used for cross-correlation together with five events that have different correlation values with the template waveforms. Based on this an appropriate threshold was set to 0.60 for the hybrid slopequakes (I) class and 0.55 for the hybrid slopequakes (II) class (table 1).

Table 1: Cross-correlation thresholds.

Cross-correlation coefficient thresholds	
Event type	Threshold
Hybrid slopequakes (I)	0.60
Hybrid slopequakes (II)	0.55
Low-frequency slopequake	0.65

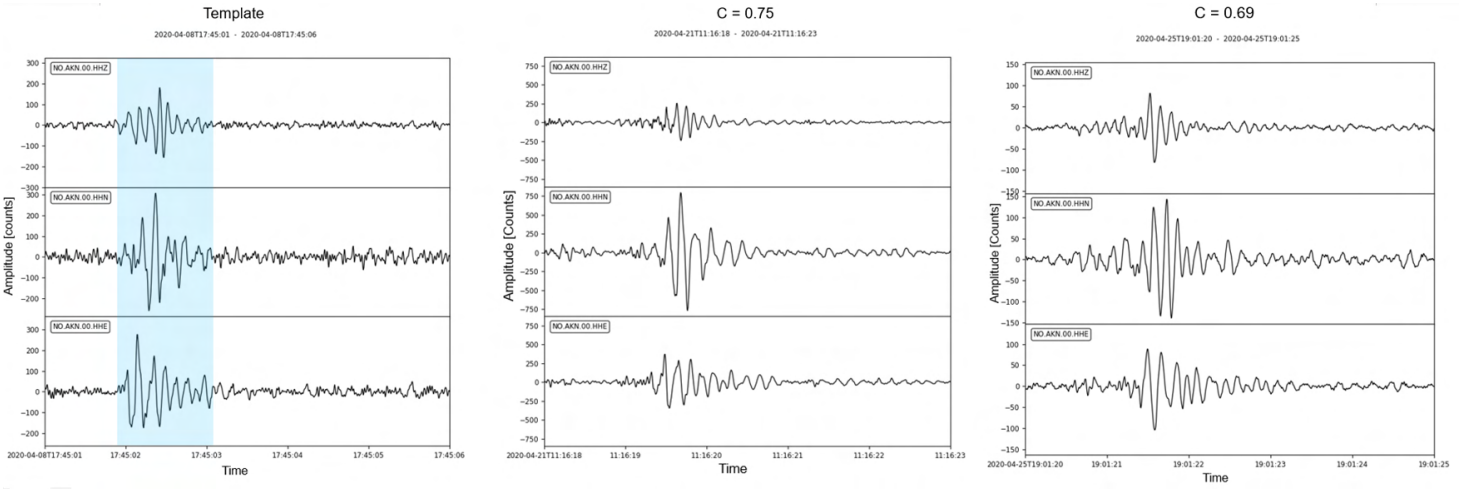

(a)

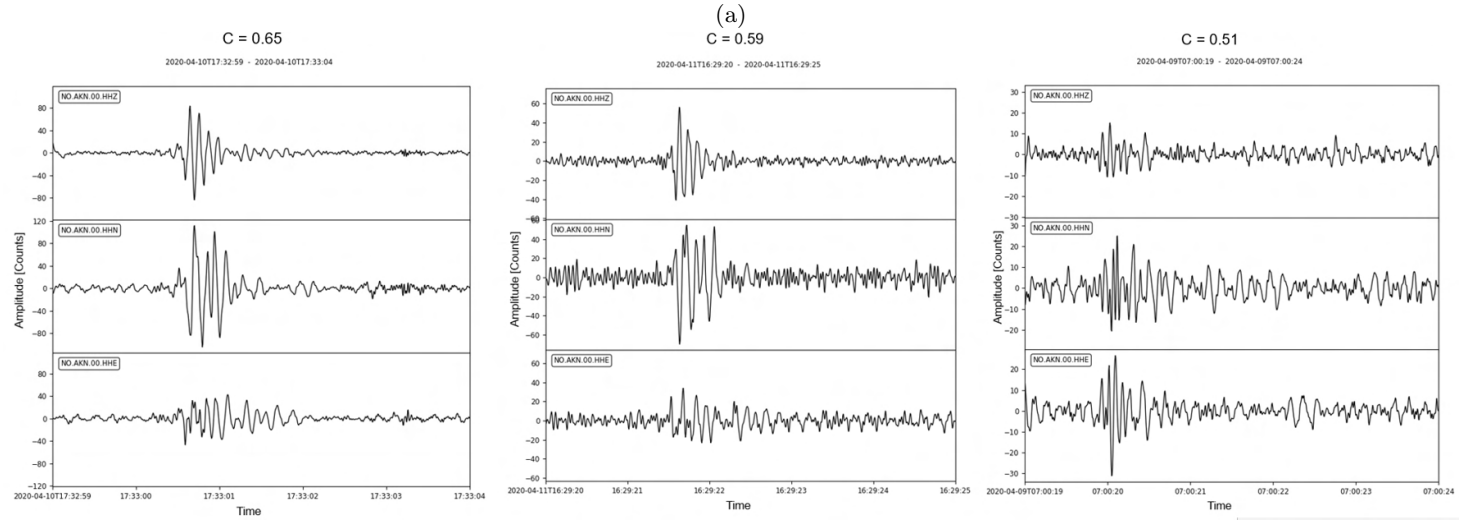

(b)

Figure 22: Low-frequency slopequake threshold calibration. C = cross-correlation coefficient. a) Seismogram of template waveform and the time window (blue) used for cross-correlation, and events with correlations of 0.75 and 0.69 with the template. b) Examples of waveforms with correlations of 0.65, 0.59 and 0.51 with the template event in a). A high degree of similarity was found for C = 0.65 and above, thus a threshold of 0.65 was used for this class.

Processing steps and cross-correlation calculations

After setting the cross-correlation coefficient thresholds and time windows to be used, a file was defined to contain information about the cross-correlation event detections (time and cross-correlation coefficient). In a next step, data for the templates between the start and end of the time windows was loaded and processed in the same way as was done for the STA/LTA event detection. Demean and bandpass filtering in the range 2-60 Hz were applied, as described and explained more under section 5.1.

In the next part of the script, one day of continuous data was loaded in, and processed (demean and bandpass filtering) similarly to the template signals. The template event cross-correlation was then performed by passing the templates through the data and calculating the correlation for every time sample point, using the Pearson normalized version of cross-correlation (equation 6). All three components were used in the calculations. The average of the correlation between the individual components was estimated and if the average of the coefficient was higher than the given threshold, a new event was registered for that time.

To get as few false detections as possible, all the registered detections were checked against the STA/LTA event record, and only overlapping events were kept. In addition, the record was checked for events matching with more than one template signal, which was the case for only one event.

5.4 Polarization analysis

To be able to estimate source directions/locations from a single-station three-component system (described more in section 3.5), it is crucial to separate different phase arrivals. By investigating the particle motion (polarization) of a signal this might be possible, as one can exploit that different seismic phases are polarized differently. An attempt has been made to perform such analysis on local events at Åknes, in order to estimate the source directions (back-azimuths). In the following sections a description of the process for back-azimuth estimation of local events is given.

5.4.1 Amplitude cross-plot analysis

A common method for polarization analysis is to plot the different components of a three-component seismic recording against each other over a time window, to investigate the wave polarization (e.g linear or elliptical). Short time windows of a few periods along a wave are typically used for such analysis, which may reveal different seismic phases in the waveform (e.g. P-waves or Rayleigh waves). Having a three-component seismogram with a vertical component (Z), east component (E) and a north component (N), it is possible to investigate the particle motion in two vertical planes (E-Z and N-Z) and a horizontal plane (E-N).

5.4.2 Regional events as reference

The region around Åknes sometimes experiences small earthquakes. Many of these events have been localized by NORSAR. Several of them are easily identified on the AKN station and the polarization of these waveforms could be used as a reference for more local events, even though local events have a much shorter distance from the source to the receiver. To see what a first arriving P-wave could look like in amplitude cross-plots and if it was possible to find the directions to events of known locations, three regional earthquakes (magnitude 2.5-2.7) not very far away from Åknes were studied. In addition, observations of the seismograms of local events showed that the vertical component commonly has lower amplitudes than the horizontal ones. This effect may be due to local conditions, or it could indicate that there is something wrong with the instrument. Therefore, regional earthquakes were also used to investigate this issue, as one would expect a rather vertical incidence for these events.

If travelling in a homogeneous and isotropic medium the P-wave should be linearly polarized in the direction of propagation, but in the inhomogenous earth the particle motion could be more irregular or elliptical. Especially higher frequencies are affected by inhomogeneties (Bormann et al., 2009). Figure 23 shows a map of the picked events together with the location of Åknes. In figure 24.a, the location of a regional event of magnitude 2.5 and the corresponding recording on AKN with the investigated time window are shown. Amplitude cross-plots of the ZNE-system can be seen in figure 24.b. It shows a relatively linear polarization in all three planes, but some irregularity and ellipticity can be observed. If the event is correctly localized, the back-azimuth that can be read from the plots seems to give a good estimate of the source direction, towards the west/northwest. The incidence is near vertical and the recording does not indicate any issues with the vertical component. Analysis of the two other regional events are given in appendix B (figure 45 and 46). The polarization analysis was tested for frequencies in the range 5-50 Hz, which also could be a suitable range for first arrivals of local events.

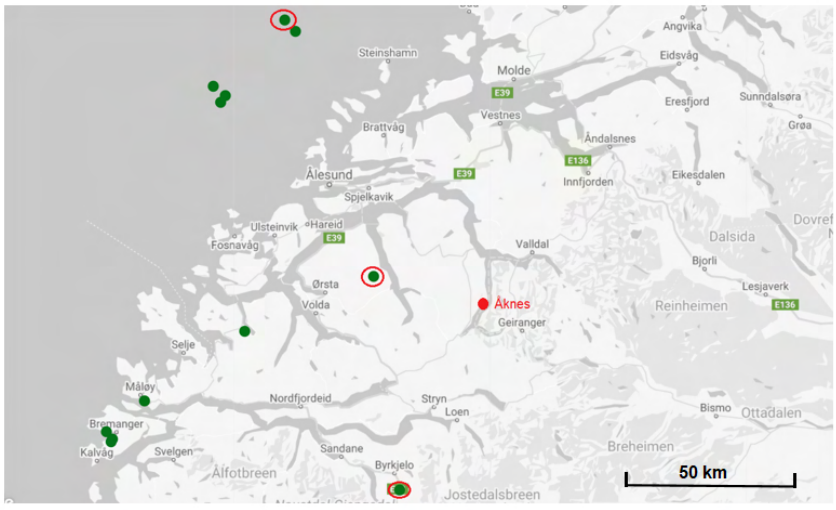

Figure 23: Overview of regional earthquakes that were analysed. Red circles mark the three events.

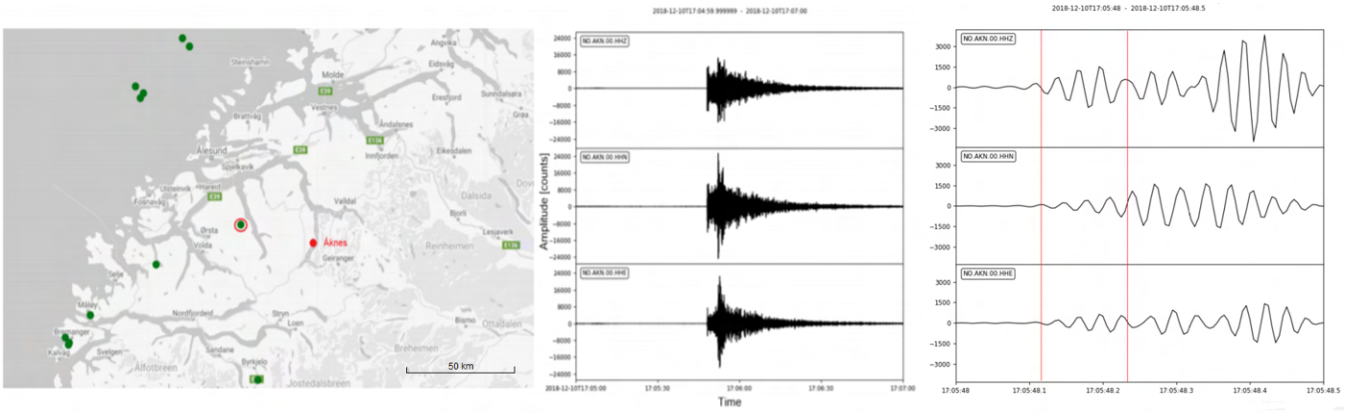

(a)

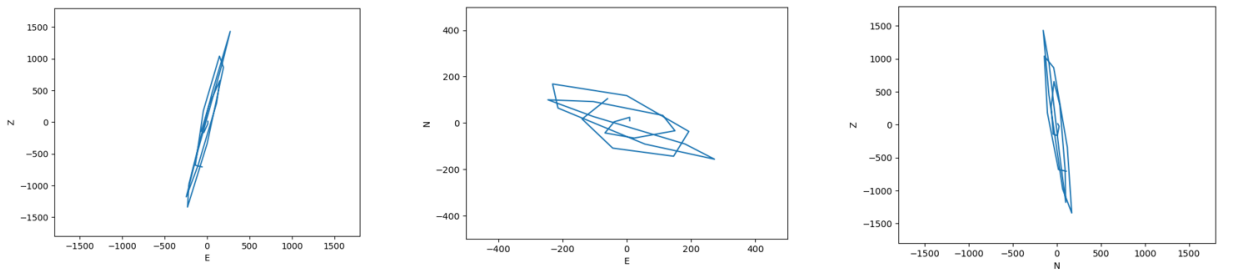

(b)

Figure 24: Polarization analysis of regional earthquake. a) From left to right: location of event (marked by red circle), seismogram in 2 minutes time window and zoom in on first arrivals and time window used for the analysis (marked by red vertical lines). b) Amplitude cross-plots in the two vertical planes (E-Z and N-Z) and the horizontal plane (E-N).

5.4.3 Polarization analysis of local events

Polarization analysis of several events in each event class was performed. It turned out to be a demanding task, as it in most cases was not easy to see a clear signal onset. Therefore, amplitude cross-plots in the two vertical planes (E-Z and N-Z) and the horizontal plane (E-N) were created for smaller time windows along the waveforms. The different time windows were colorcoded and plotted in the planes with corresponding colors, in order to easier see how the polarization changed. Since an exact signal onset was difficult to visually determine in most cases, the start of the analyses was slightly before the STA/LTA onsets. In the following, the polarization of events in the different classes is described.

Hybrid slopequakes (I)

Figure 25 shows an example of polarization analysis of an event in the hybrid slopequakes (I) class. In the first time window (blue) a relatively linear particle motion is observed in all three planes, which might imply P-wave arrivals. If so, the wave is coming from a north/north-northeast direction. Further, the particle motion changes to a direction that looks quite perpendicular to the first motions in the second time window (orange), which may indicate the arrival of S-waves within this window. Plots of the two latest time windows (green and purple) show a relatively elliptical particle motion, which might be elliptically polarized Rayleigh wave arrivals. Compared to the regional events, the vertical component is quite small relative to the horizontal components. This may imply sub-horizontal propagating P-waves (in blue), as indicated by the particle motion in the vertical planes, especially the N-Z plane. For S-waves it is more difficult to infer something from the amplitude of the vertical component, as it can be both SH and SV components.

Two other examples of analysed events in this class can be found in appendix C (figure 47 and 48). They show much of the same features, especially in the first part of the waveforms. A relatively linear polarization in all three planes is generally seen right after the STA/LTA onsets, before the polarization seems to change to a motion that looks quite perpendicular in the second time window compared to the first one. Further, it seems to be a transition to a somewhat more elliptical particle motion. The observed particle motions within the first time window imply a P-wave propagation that is commonly sub-horizontal for these events.

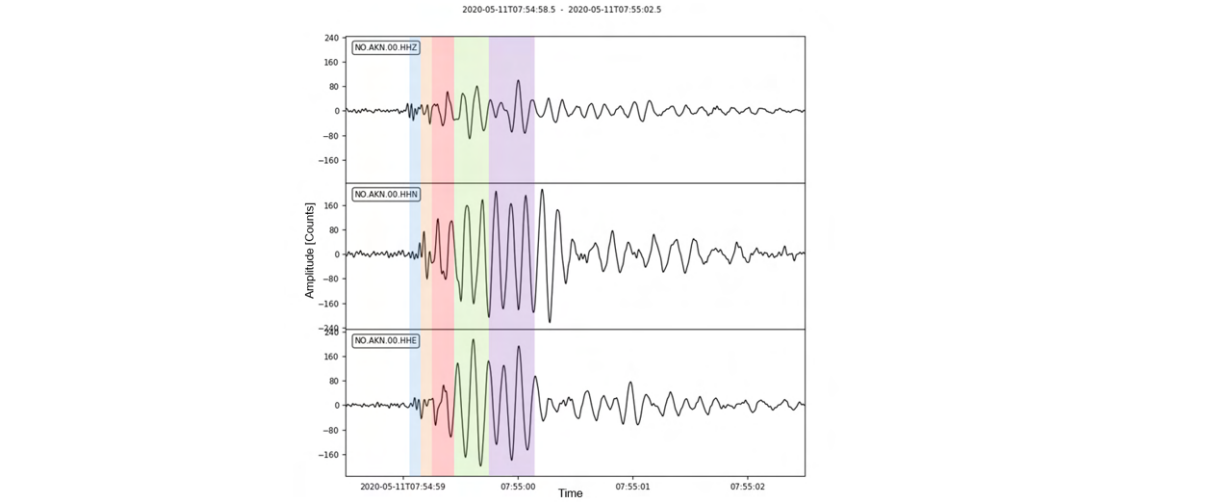

(a)

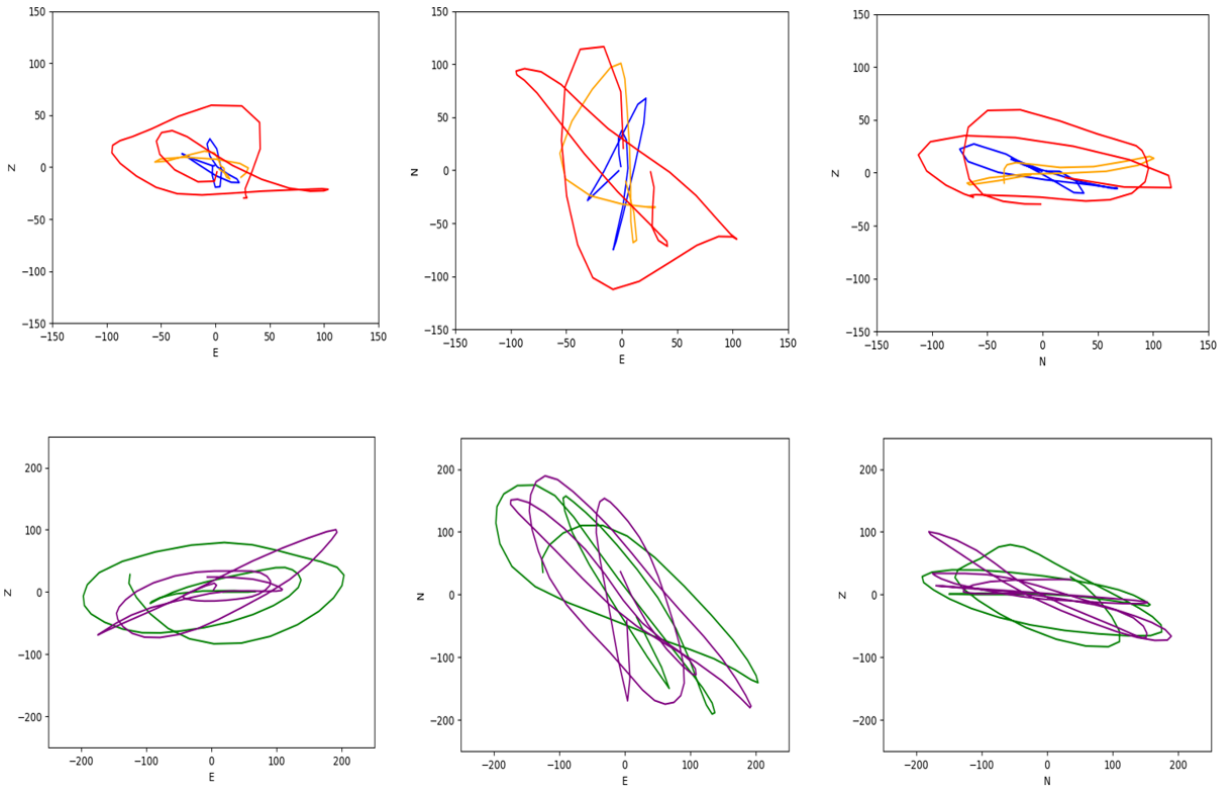

(b)

Figure 25: Example of polarization analysis of an event in the hybrid slopequakes (I) class. a) Seismogram of event with colored time windows used for the analysis. b) Amplitude cross-plots with colors corresponding to the different time windows.

Hybrid slopequakes (II)

In figure 26, an example of polarization analysis of an event in the hybrid slopequakes (II) class is seen. The amplitude cross-plots of the first time window (blue) indicate a relatively linear polarization in all three planes, which might imply dominating P-wave arrivals. If this is the case, the incoming wave is coming from the northwest. Further, the particle motion seems to change in the second and third time window (orange and red) to a direction that is quite perpendicular to the first motions. This may indicate a change from P-wave arrivals to S-wave arrivals. In the plots of the later time windows (green, purple and black) it is not easy to see a characteristic particle motion. The purple plot shows a somewhat elliptical motion, which might be an elliptically polarized Rayleigh wave. Amplitudes on the vertical component are also here quite small relative to the horizontal components, implying sub-horizontal propagating P-waves (blue), as illustrated by the particle motions in the vertical planes. It indicates that the source is in the sub-surface and not from deep into the basement.

Two other examples of analysed events in this class can be found in appendix C (figure 49 and figure 50). The polarization of these waveforms show much of the same trends as for the analysed event in figure 26. A quite linear polarization in all three planes is observed for the first (blue) time windows, which may indicate that the very first periods of events in this class are generally dominated by P-waves. They also show a change in particle motion in the following, to a direction that is somewhat perpendicular to the motion in the first time window. For later arrivals the amplitude cross-plots are more chaotic and it is difficult to see any good signs of the wave types. The observed polarization in the vertical planes within the first time window, indicates a generally sub-horizontal P-wave propagation.

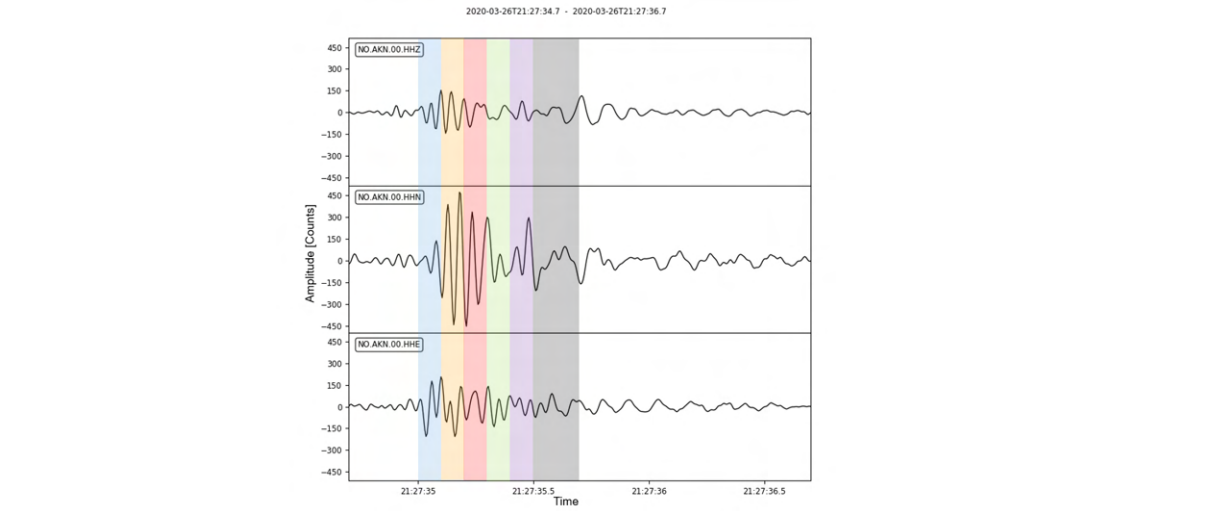

(a)

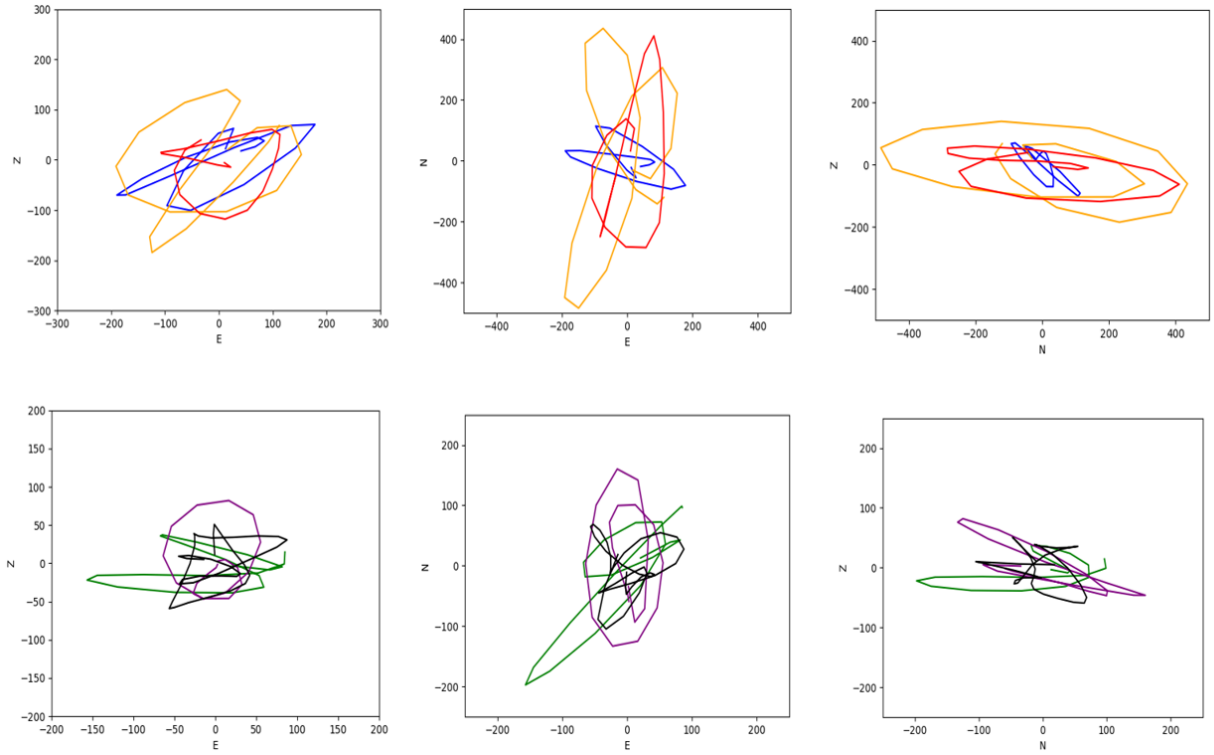

(b)

Figure 26: Example of polarization analysis of an event in the hybrid slopequakes (II) class. See explanation of figure 25.

Low-frequency slopequakes

Figure 27 shows the amplitude cross-plots and seismogram with the time windows used for polarization analysis of an event in the low-frequency slopequakes class. No very clear indications of different seismic phases can be observed, although the particle motion looks partly somewhat elliptical, which may imply that there are Rayleigh waves in the signal. On the other hand, if it is only Rayleigh waves, it is expected to see one dominant direction in the horizontal plane. The particle motion in the E-N plane here is rather complex. It indicates that if there are Rayleigh waves, they interfere with other wave types also, perhaps Love waves.

Two other examples of analysed waveforms in this class can be found in appendix C (figure 51 and figure 52). It shows similarly to the event described here, that different phase arrivals are difficult to observe. Some indications of elliptical polarization are found, and it may be that Rayleigh waves are generally found in these types of signals. On the other hand, indications of Rayleigh waves vary much for the analysed events and it is not possible to say that it is in general the dominating wave type.

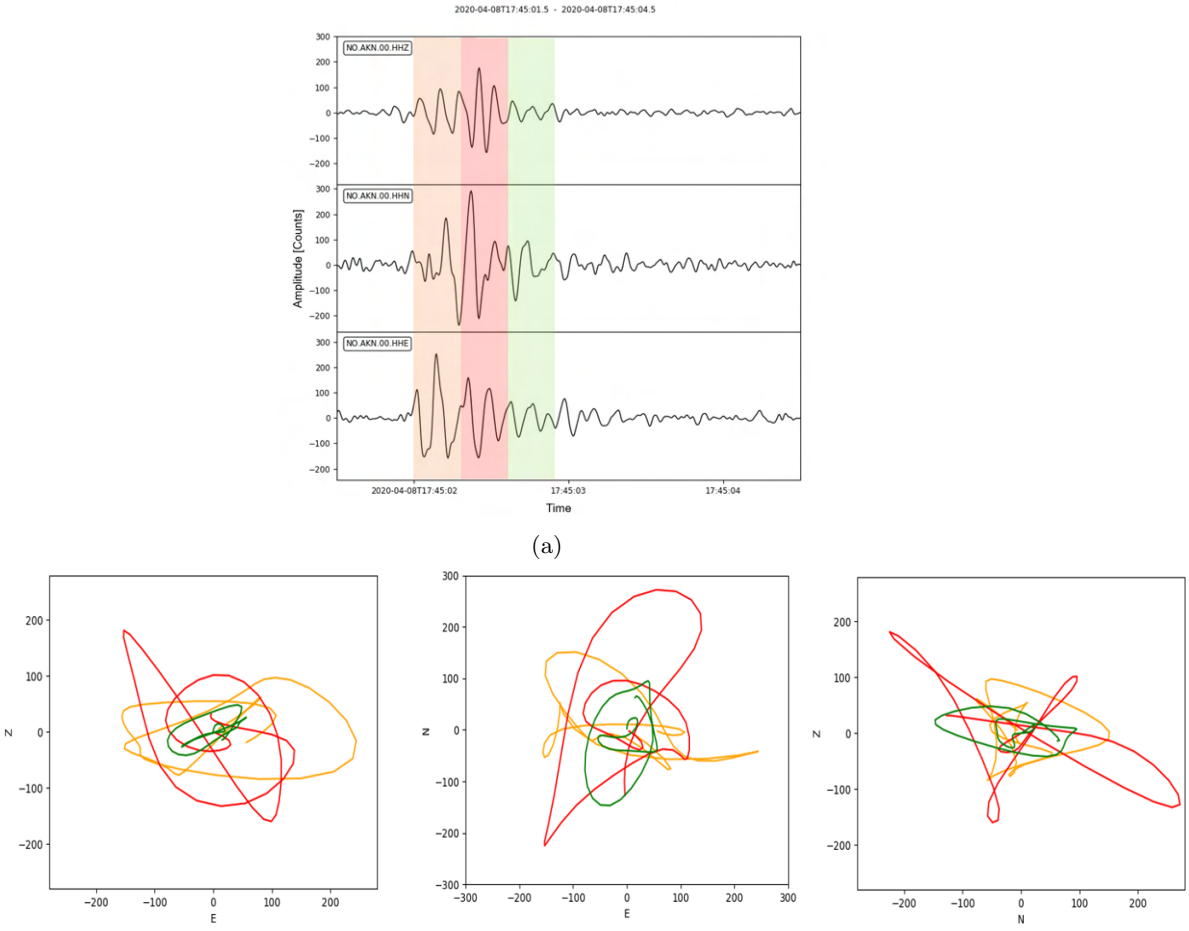

(a)

(b)

Figure 27: Example of polarization analysis of an event in the low-frequency slopequakes class. See explanation of figure 25.

Rockfalls

Polarization analysis of an event classified as a rockfall is given in figure 28. No very clear indications of different phase arrivals can be observed. The particle motions in the beginning of the signal (blue window) seem somewhat linear in all three planes, might indicating dominating P-waves. Further, the polarization tends to change to be more elliptical, perhaps indicating that there are Rayleigh waves involved. However, it remains difficult to determine different wave types from the cross-plots. Another example from this class can be found in appendix C.

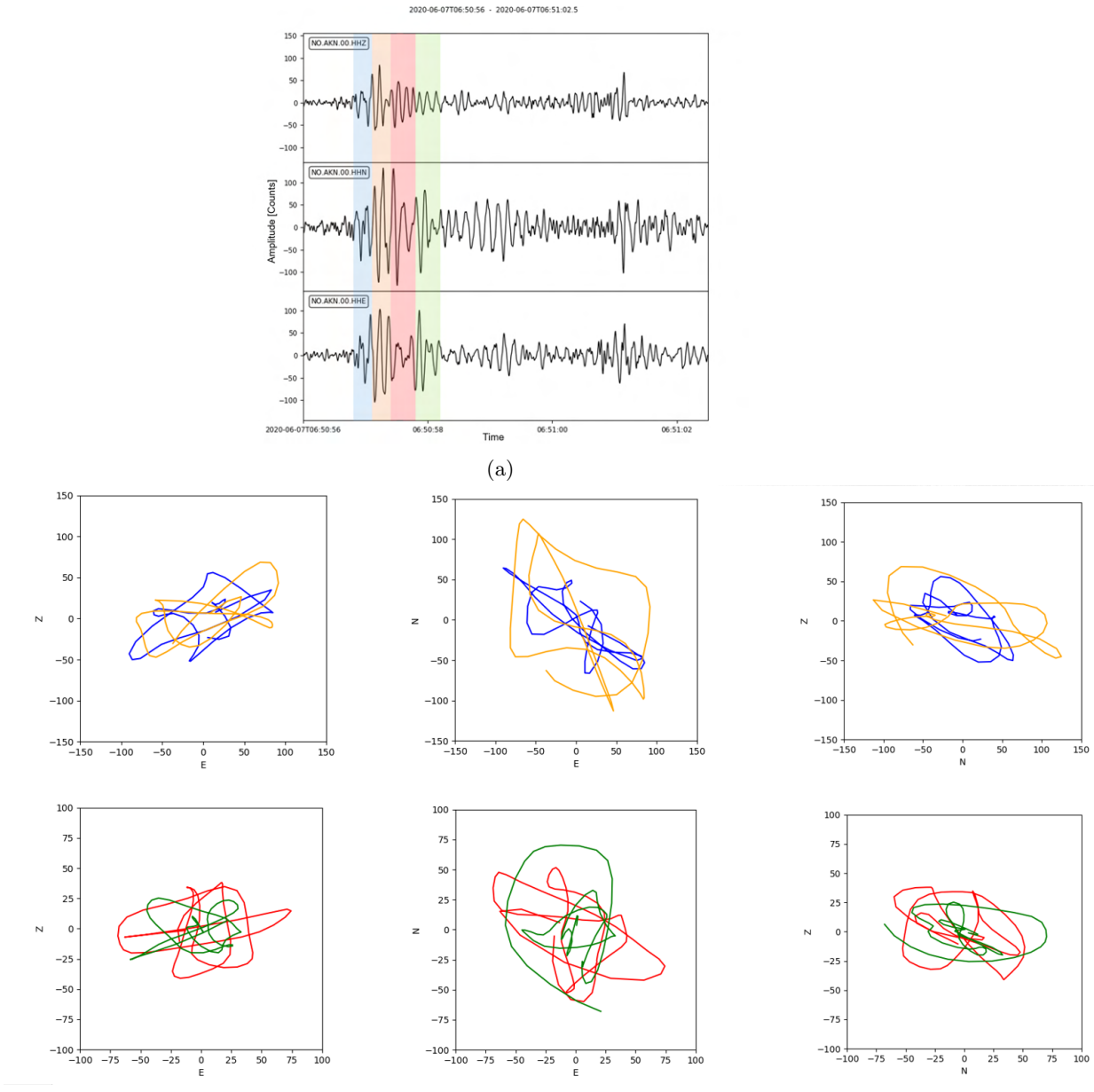

(a)

(b)

Figure 28: Example of polarization analysis of an event in the rockfalls class. See explanation of figure 25.

5.4.4 Polarization analysis using rotated coordinate system

A final thing that was tested regarding polarization analysis, was to perform the analysis in a rotated coordinate system aligned with the slope. The slope is oriented approximately north-south and is dipping about 30° in average. To investigate if this could have an effect, it was tested to rotate the data 30° into a new coordinate system where Z and N are transformed into L and Q, as illustrated in figure 29. The function rotate($ZNE -- > LQT$) in Obspy was utilized to perform the rotation. It rotates the data from the left-handed ZNE-system to the right-handed LQT-system. An example of polarization analysis in the rotated coordinate system can be seen in figure 30. It shows amplitude cross-plots of an event in the rockfalls class, the same as in figure 28. Examples from the slopequakes classes are given in appendix D. Doing the polarization analysis in the rotated system did not reveal anything new than what was not already observed from the analysis in the ZNE-system.

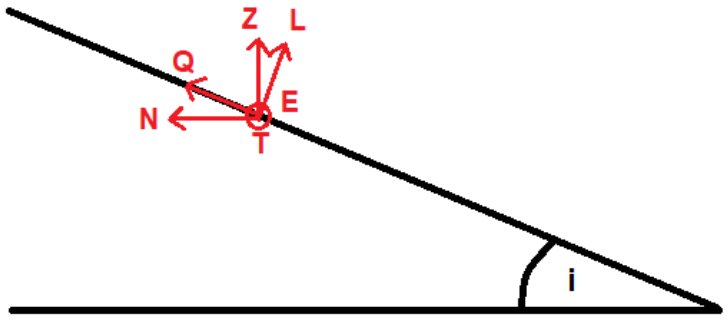

Figure 29: Simple sketch illustrating the rotation into a new coordinate system. The angle $i = 30°$.

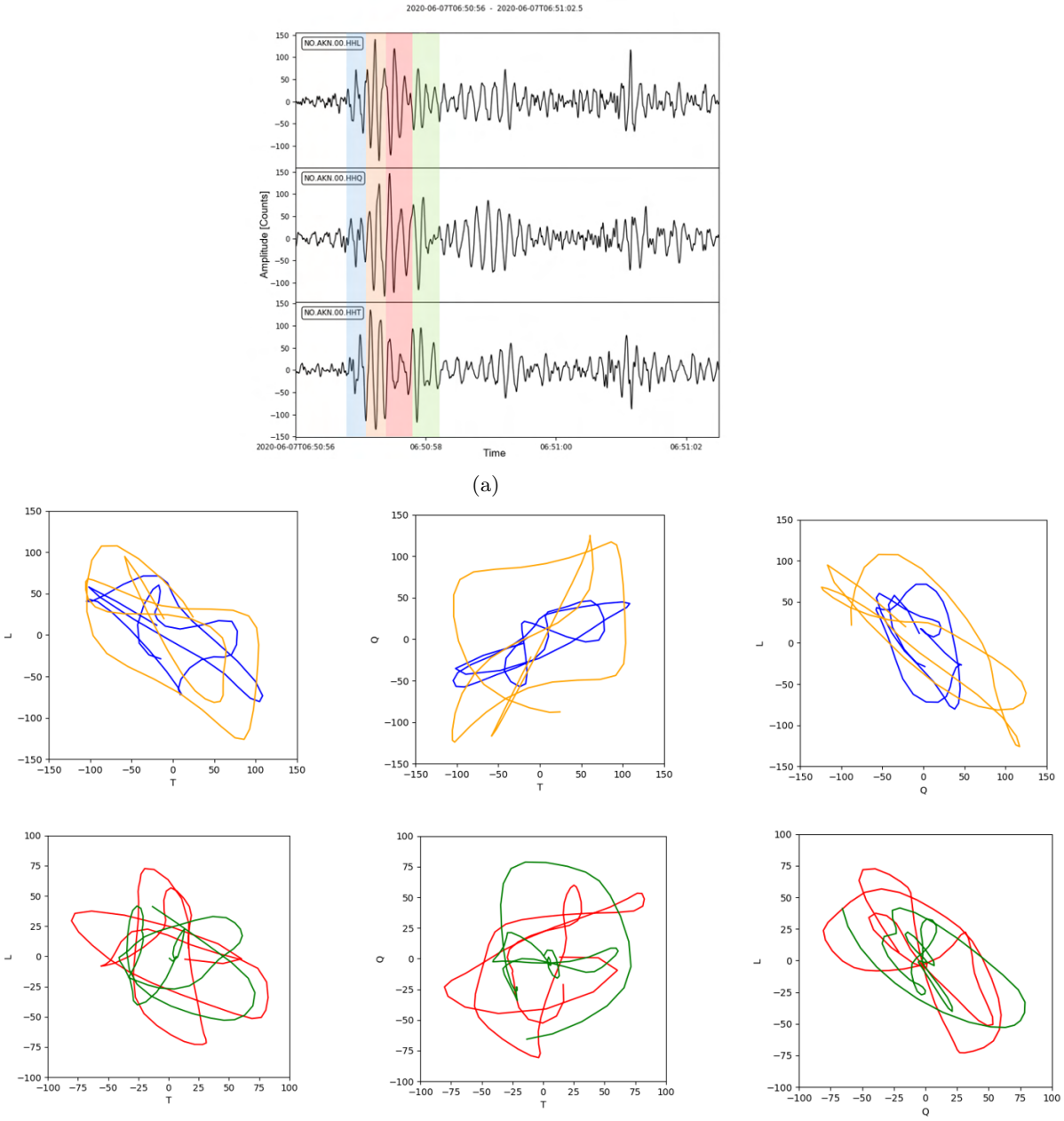

(a)

(b)

Figure 30: Example of polarization analysis of an event in the rockfalls class in rotated system. See caption of figure 25 for explanation.

5.4.5 Back-azimuth estimation from first arrivals of hybrid slopequakes

After studying the polarization of local events and fair indications of dominating P-waves in the high-frequency first arrivals of both types of hybrid slopequakes in several cases, it was decided to try to use these events for determination of source directions. Clear indications of other phases that could be used (Rayleigh waves) were difficult to see and it was found that the best was to use the assumed first arrivals. The polarization analysis of low-frequency slopequakes and rockfalls showed that it was very difficult to identify different phases, and were found not to be suitable for back-azimuth estimations. The process for back-azimuth determination is described in the following.

Algorithm for estimation of back-azimuths

The same approach as proposed by Köhler et al. (2019) for source directions determination from P-wave arrivals was utilized. As described earlier (section 3.5), this method determines the direction with respect to north that gives the most energy on the radial component, which should be in the source direction. It can be done by first estimate the direction that gives the best correlation between the radial component and the vertical component, because they should be equally polarized. This gives a range of 180° for the source direction (+/- 90° the direction of best correlation between radial and vertical component). To calculate the back-azimuth one can find the direction which gives the most energy on the radial component in this range (Köhler et al., 2019). To do so, a Python script working with the Obspy implementation was used.

First, the frequency range and time windows were determined. The chosen frequency range was 10-40 Hz, based on observations of the dominating frequencies of the first arrivals. A time window of 100 ms (20 sample points) starting slightly before the STA/LTA onsets (5 sample points) was chosen. Very clear first onsets was in general difficult to observe, but based on the polarization analysis it was decided to go with this time window and assume dominating P-waves.

The data containing the events was then loaded and filtered in the chosen frequency range. Further, rotation from the ZNE-system to the ZRT-system through all angles ($1 - 360°$ clockwise from north) was performed, and the correlation between the vertical and radial component within the chosen time window was determined for each angle. For the rotation from the ZNE-system to the ZRT-system the function rotate(NE−− >RT) in Obspy was applied. The rotation from ZNE-components to ZRT-components is performed by taking the product of the NE-components and a rotation matrix as given by equation 11 and 12 under section 3.5. The correlation between the vertical and radial component was determined by calculating the Pearson normalized cross-correlation (as described in section 3.4.2) between the two components for each angle.

Finally, the direction of maximum energy (amplitude) on the radial component was determined as the back-azimuth. Figure 31 shows three examples of back-azimuths estimated using the proposed method. After rotation into the ZRT-system most energy is found on the radial component within the windows used for back-azimuth determination, but some energy is still

present on the transversal component in all three cases. This may imply that there are also other waves involved, not only P-waves.

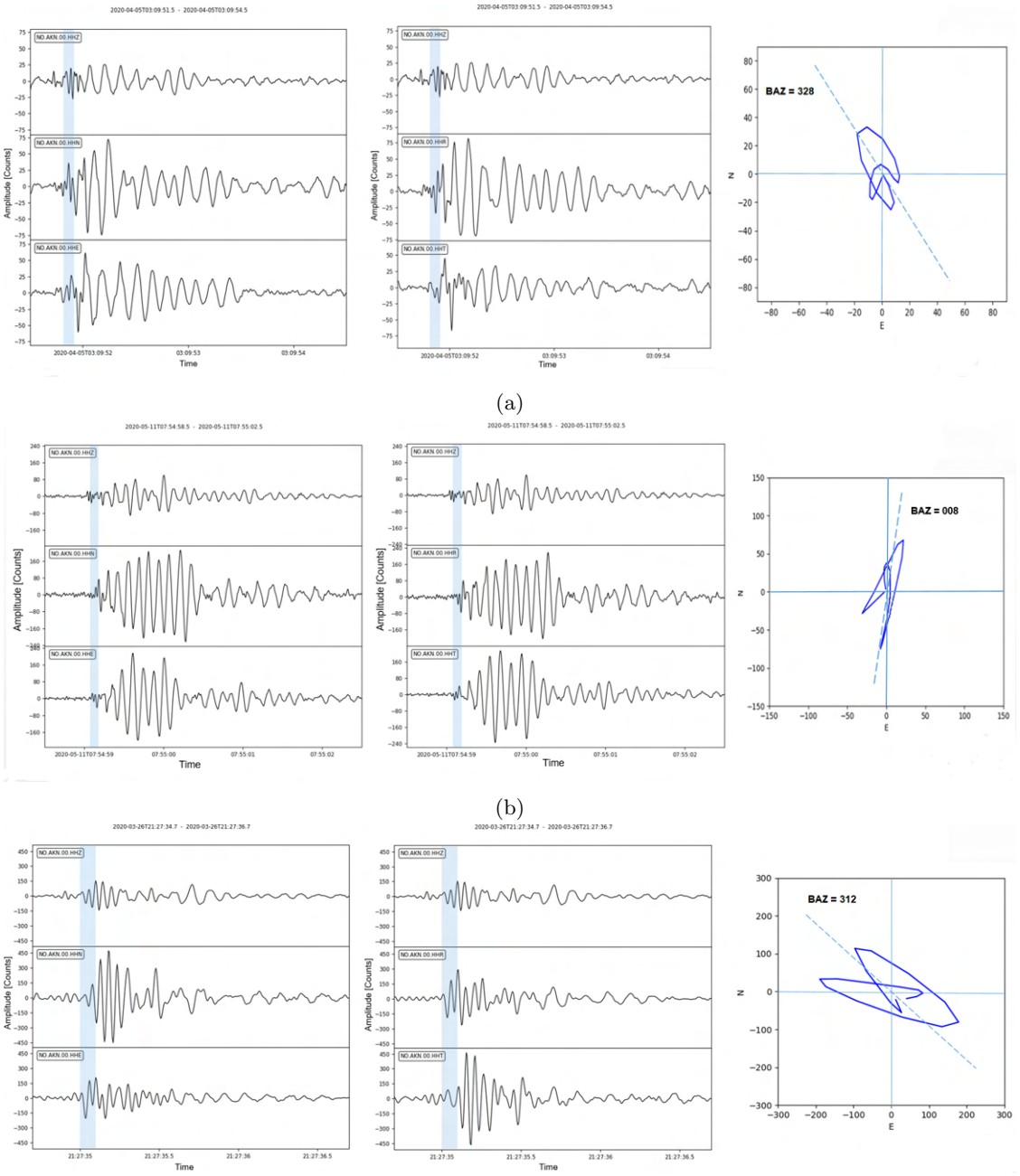

(a)

(b)

(c)

Figure 31: Examples of back-azimuths determined for two events in the hybrid slopequakes (I) class (a and b) and one event in the hybrid slopequakes (II) class (c). Left: seismograms with the time windows (blue) used for the analysis in the ZNE-system. Middle: seismograms after rotation to the ZRT-system. Right: amplitude cross-plots in the horizontal plane (E-N). Stipled lines show the directions of most energy on the radial component.

Comparison with event locations from the geophone network

Three of the hybrid slopequakes events have been localized by Nadège Langet (NORSAR), using the geophone network at the site. They were localized from first arrivals on 5 of the geophones (geophones 1-5) with a 3D velocity model. Locations of the three events are plotted as yellow circles in figure 32. They are the same events as in figure 31. Event 1 belong to the hybrid slopequakes (II) class, event 2 and 3 to the hybrid slopequakes (I) class. Back-azimuths associated with event locations from the geophone network agrees well with the ones estimated from polarization analysis for the first two events (table 2), as they only differ by 5° and 8°. For the third event the difference of 41° is a little bit larger. The larger difference here does not seem to be due to more energy on the transversal component, as it is not more energy relatively to the radial component in this case than for the two other events. It can perhaps be linked with uncertainties as regards the pick of traces used for the analysis, or with the velocity model used for the event location.

Table 2: Back-azimuths associated with locations from the geophone network (a) and from polarization analysis in this study (b).

(a)

Event	Time	BAZ
1	26-Mar-2020 21:27:34	320
2	05-Apr-2020 03:09:51	323
3	11-May-2020 07:54:58	327

(b)

Event	Time	BAZ
1	26-Mar-2020 21:27:34	312
2	05-Apr-2020 03:09:51	328
3	11-May-2020 07:54:58	008

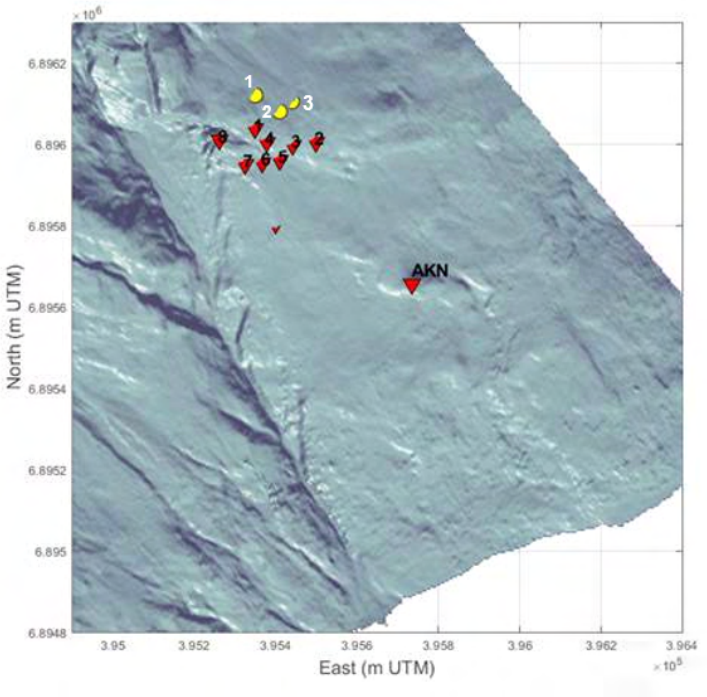

Figure 32: Locations of three hybrid slopequakes events.

6 Results

In this chapter the results from the performed analysis are given, including STA/LTA event detections, template event cross-correlation detections and back-azimuth estimations.

6.1 STA/LTA detections and meteorological data

Figure 33 shows detected STA/LTA events together with daily average temperature, daily maximum temperature and daily precipitation during the period 01.03.20 to 15.06.20. The average temperature stays mainly negative during March until the middle of April. In the second half of April temperatures stay mostly positive, before a new drop in temperatures and a period of negative temperatures are seen from early May to the middle of May. Temperatures then stay positive from the middle of May throughout the period. Significant temperature variations appear during the period, and remarkable variations around $0°C$ are seen from early March until the middle of May, as illustrated by both the average and maximum temperature curves.

The curve of daily precipitation shows great variations during the period, from 0 mm to about 50 mm per day. A relatively dry period is seen during the first half of March. More moderate amounts can be observed in the second half of March, most is seen during the last days of the month. Little precipitation is noticed the first days of April, before a significant rise and large amounts over several days can be observed around mid-April. From mid-April to about mid-May the daily precipitation is generally low, although some smaller variations occur. Further, a very dry period is indicated by the curve until mid June.

An average of about 200 STA/LTA events was detected per day. The number of detections varies a lot during the period, between 25 and 600 per day. The overall detection rate is generally low during March and the first half of April. From the middle to late April, the overall trend is an increase in the number of daily events, before a smooth decrease and relatively low detection rate is seen during the first half of May. A new rise in detections occur during the second half of May and the number of events are generally high until the middle of June.

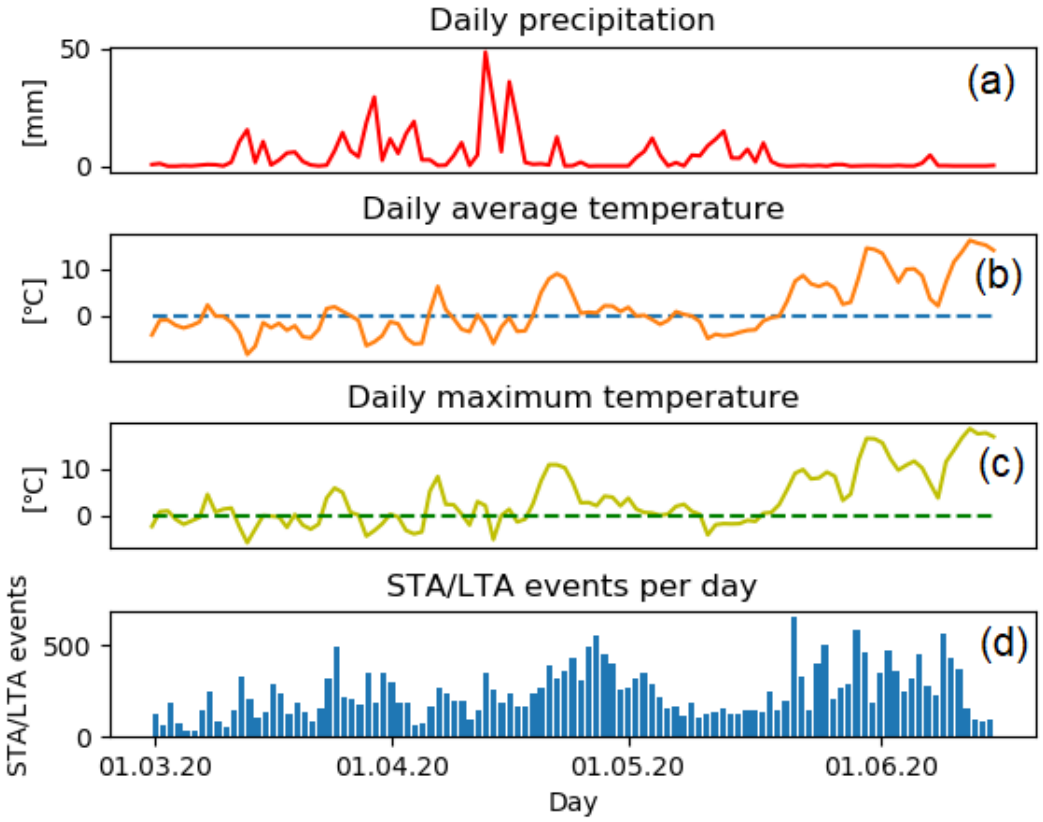

Figure 33: STA/LTA events and meteorological data from 01.03.20 to 15.06.20: a) daily precipitation in [mm], b) daily average temperature in [$°C$], c) daily maximum temperature in [$°C$], d) number of STA/LTA events per day. Stipled lines are plotted at $0°C$

6.2 Event detections from template event cross-correlation and other events

Table 3 shows an overview of the total number of events detected for each type of signal from template event cross-correlation. A total of 229 events were found to be similar enough to the template events to be classified as one of the three slopequake types. This is, compared to the overall STA/LTA event detections (figure 33), only a very small fraction. The distribution of events is 86 in the hybrid slopequakes (I) class, 25 in the hybrid slopequakes (II) class and 118 events in the low-frequency slopequakes class. Event catalogs with all cross-correlation detections of these three classes are found in appendix E (table 4-6).

Table 3: Slopequake detections from template event cross-correlation

Event detections from template event cross-correlation	
Event type	Total number of events detected
Hybrid slopequakes (I)	86
Hybrid slopequakes (II)	25
Low-frequency slopequakes	118

6.2.1 Hybrid slopequakes (I)

The time distribution of daily detections of hybrid slopequakes (I) and cumulative number of events during the period 01.03.20-15.06.20 are plotted in figure 34, together with meteorological data for the same time period. Only a few detections are seen until late March. A significant increase in the number of events can then be observed during the last days of the month. Further, the detection rate is sporadic and relatively low during the first half of April. During the second half of April and the first days of May, the number of events is generally high. Many days in a row with several event detections can be noticed, with a peak in late April. At the same time, the daily average temperature stays significantly positive for many days. As the temperature again drops below $0°C$ in early May, the daily number of events is generally low. In late May a new rise in event detections can be observed, when temperatures stay permanently positive.

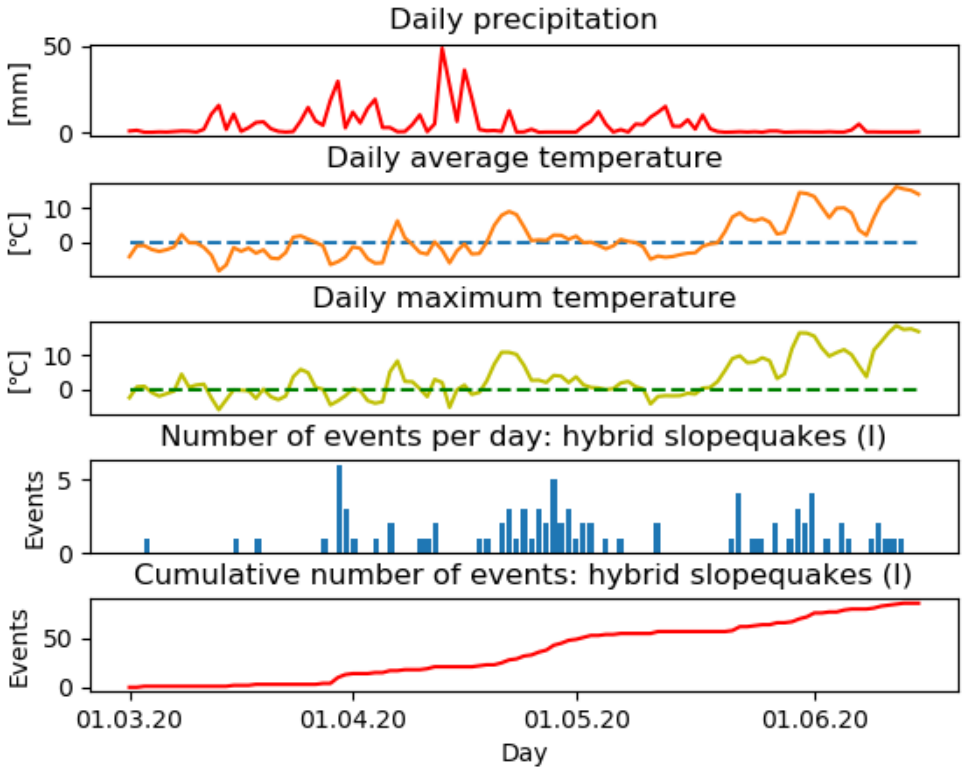

Figure 34: Time distribution of events in the hybrid slopequakes (I) class.

In figure 35.a, an example of an event detected from cross-correlation with the template event (figure 18) in the hybrid slopequakes (I) class is shown. Figure 35.b shows the spectrogram and PSD for each component. The cross-correlation coefficient is 0.62 and the waveform shape and frequency content are very similar to the template event. It has a duration of about 3 seconds. The waveform shape is characterized by largest amplitudes at the beginning of the signal, before a decay is later observed. Most of the energy is found around 10 Hz, but some high-frequency content up to 40 Hz are seen in the first part.

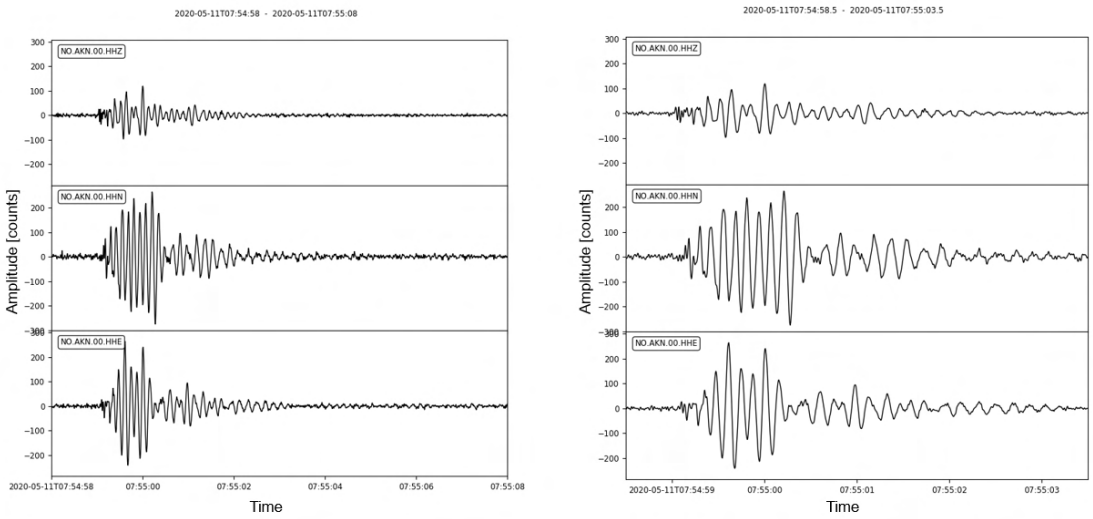

(a)

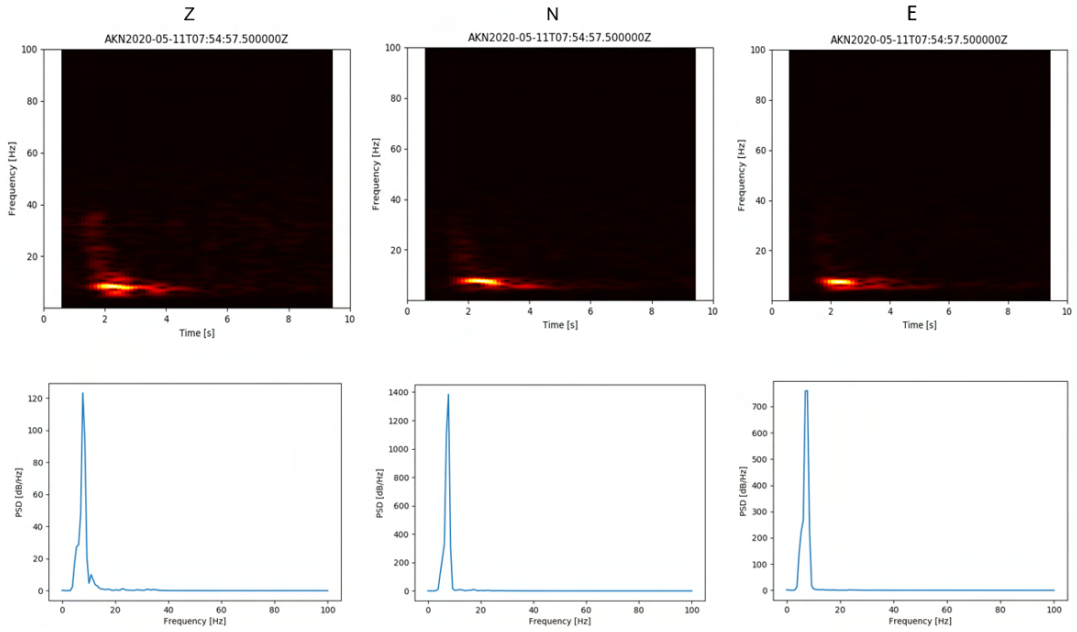

(b)

Figure 35: Example of cross-correlation detection in the hybrid slopequakes (I) class. The correlation coefficient is 0.62 to the template event (figure 18). See caption of figure 18 for explanation.

6.2.2 Hybrid slopequakes (II)

The time distribution of events classified as hybrid slopequakes (II) and meteorological data for the investigated period are given in figure 36. Overall, few events of this type were detected. During the first half of March only one event is observed. In the second half of March more events are seen with a peak in the last days of the month. During April there are very few detections until late in the month, where a significant rise is seen and many events are detected in a few days. It appears after the great temperature rise in the second half of April. Throughout the rest of the investigated period there are no correlations, except for one day in early May.

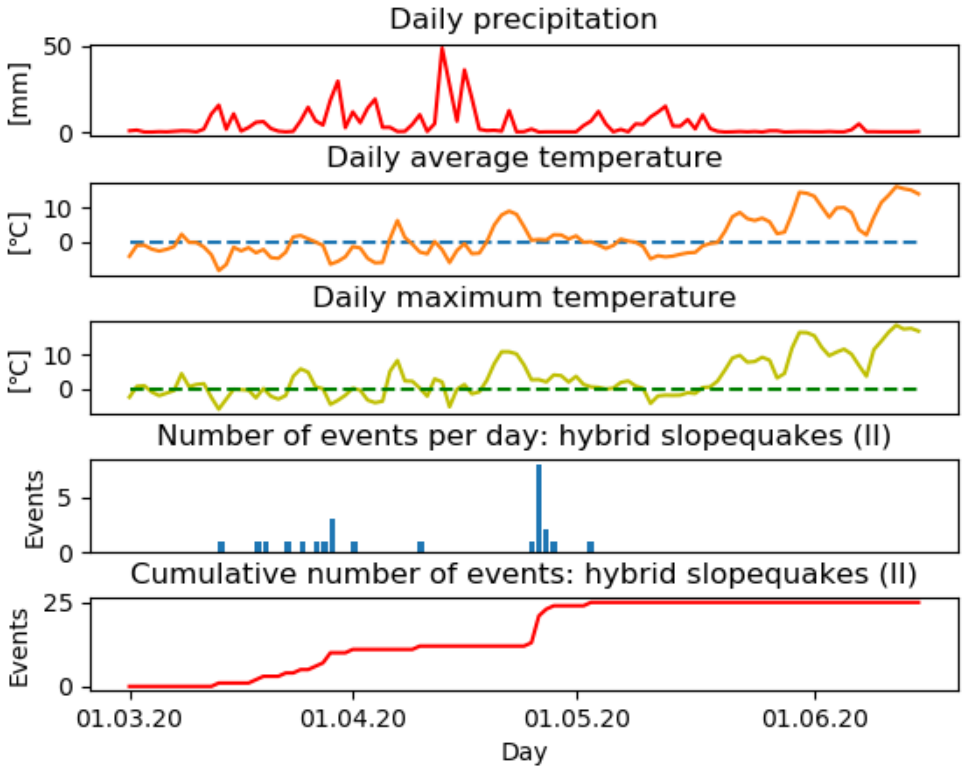

Figure 36: Time distribution of events in the hybrid slopequakes (II) class.

Figure 37.a shows an example of an event found by cross-correlation with the template event (figure 19) of the hybrid slopequakes (II) class. In figure 37.b, spectrograms and power spectral densities are given. The cross-correlation coefficient is 0.67. Many of the same characteristics as seen for the template waveform are found. It has a duration of about 1.5 seconds. The waveform shape is characterized by largest amplitudes in the first part of the signal, before a decay is seen with time. Most energy exists in two frequency bands around 10 Hz and 20 Hz and most high frequencies are observed in the first part of the signal, although there is some less low-frequency content compared to template event.

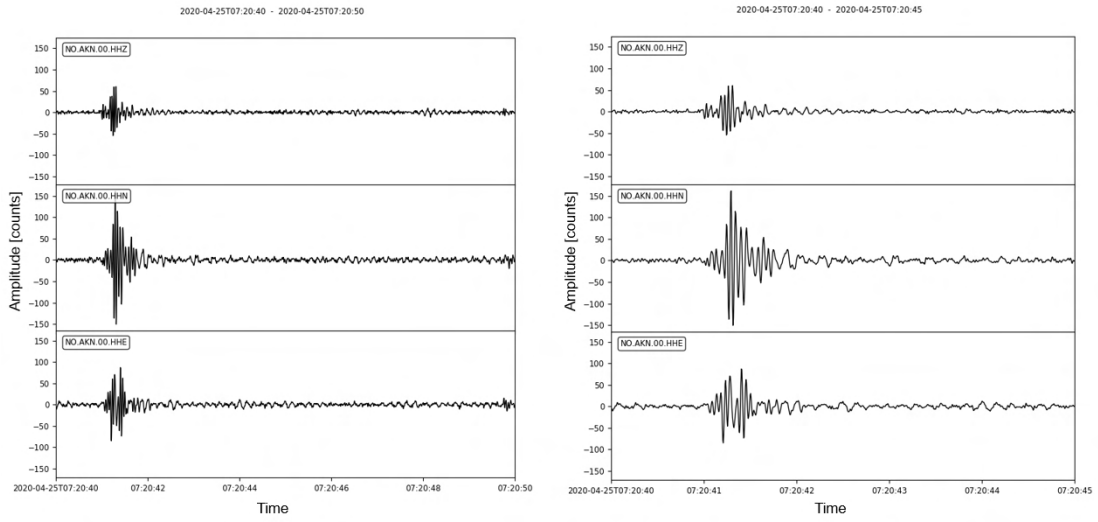

(a)

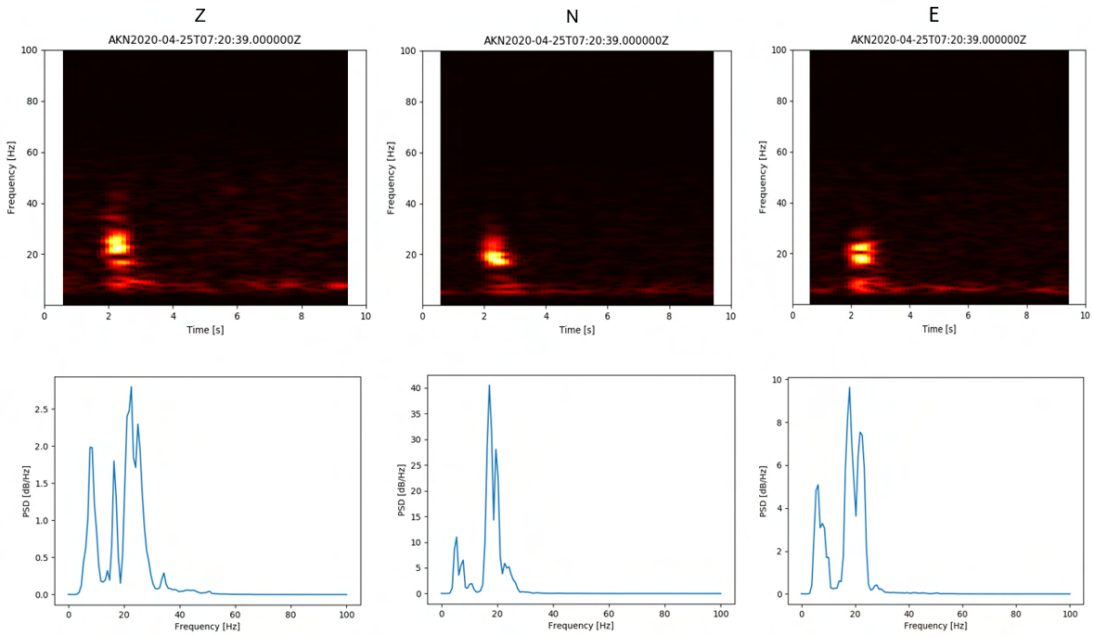

(b)

Figure 37: Example of cross-correlation detection in the hybrid slopequakes (II) class. The correlation coefficient is 0.67 to the template event (figure 19). See caption of figure 18 for explanation.

6.2.3 Low-frequency slopequakes

The distribution of low-frequency slopequakes detections is given in figure 38. It shows that there are very few detections until late March/early April, where a moderate increase in correlations occurs. During the first half of April a moderate and sporadic number of detections is seen in the histogram. In the second half of April the detection rate increases and is generally high until early May. The rise appears, similarly to the trend seen for the hybrid slopequakes classes, after the sudden rise in temperatures from negative to positive during the same period. Further, there are relatively few detections throughout the period, although a weak rise in the number of correlations is seen in late May.

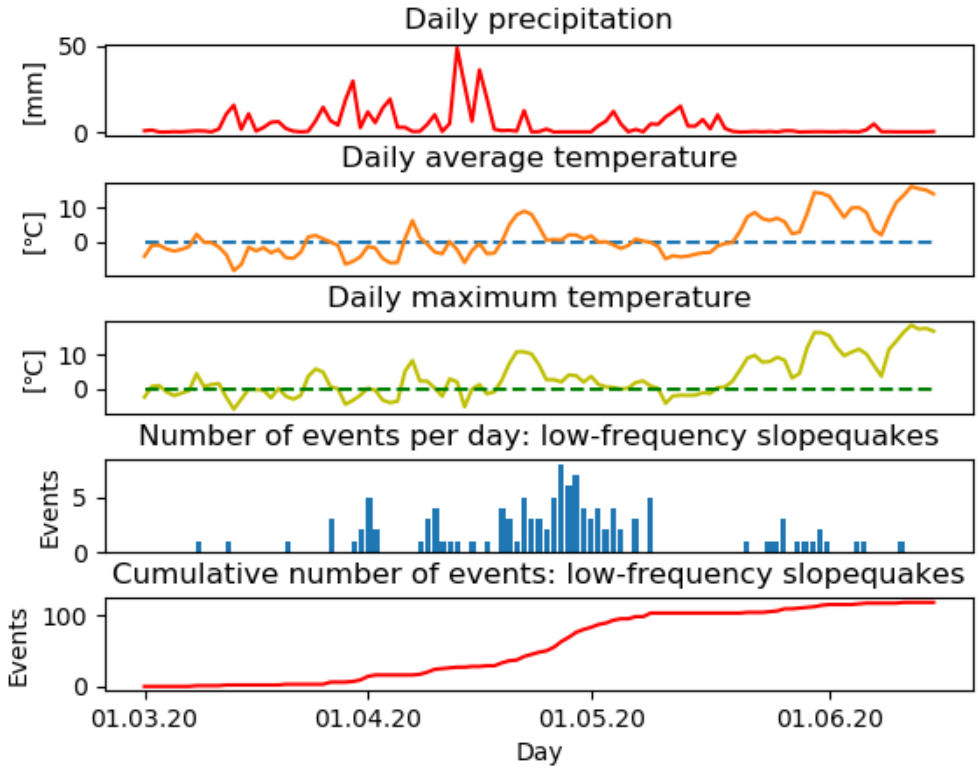

Figure 38: Time distribution of events in the low-frequency slopequakes class.

In figure 39.a an example of an event detected by cross-correlation with the template signal of the low-frequency slopequakes class (figure 20) is shown. Spectrograms and power spectral density for the three components are given in figure 39.b. The cross-correlation coefficient is 0.75 and it shows many of the same features. The duration is about 2 seconds. The waveform shape is pyramidal like with largest amplitudes in the middle of the signal. It has emergent first arrivals, hence the exact signal onset is not easy to determine. Frequencies are mainly seen in a narrow range below 10 Hz (5-10 Hz) and there are only small variations with time.

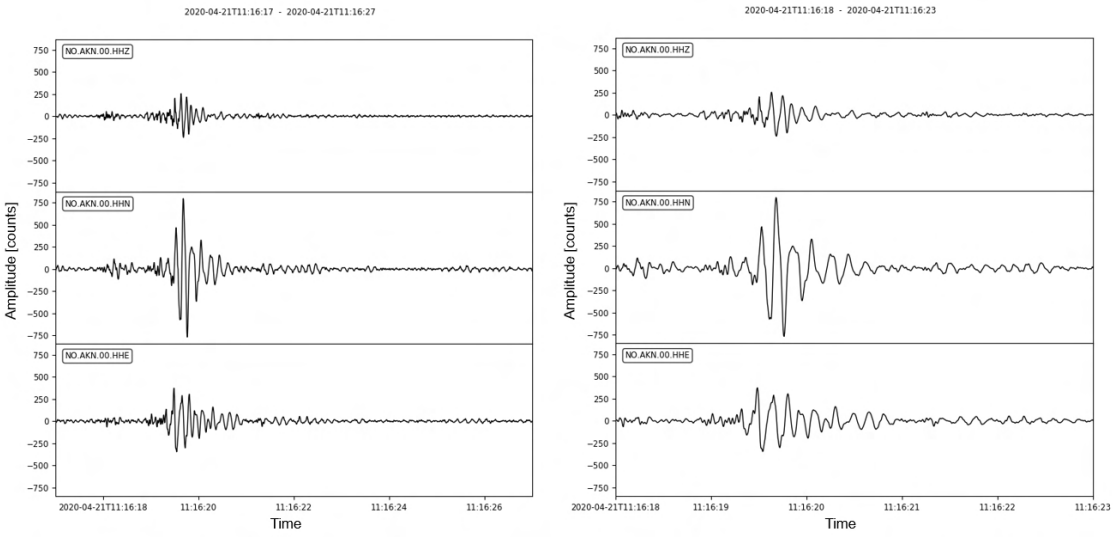

(a)

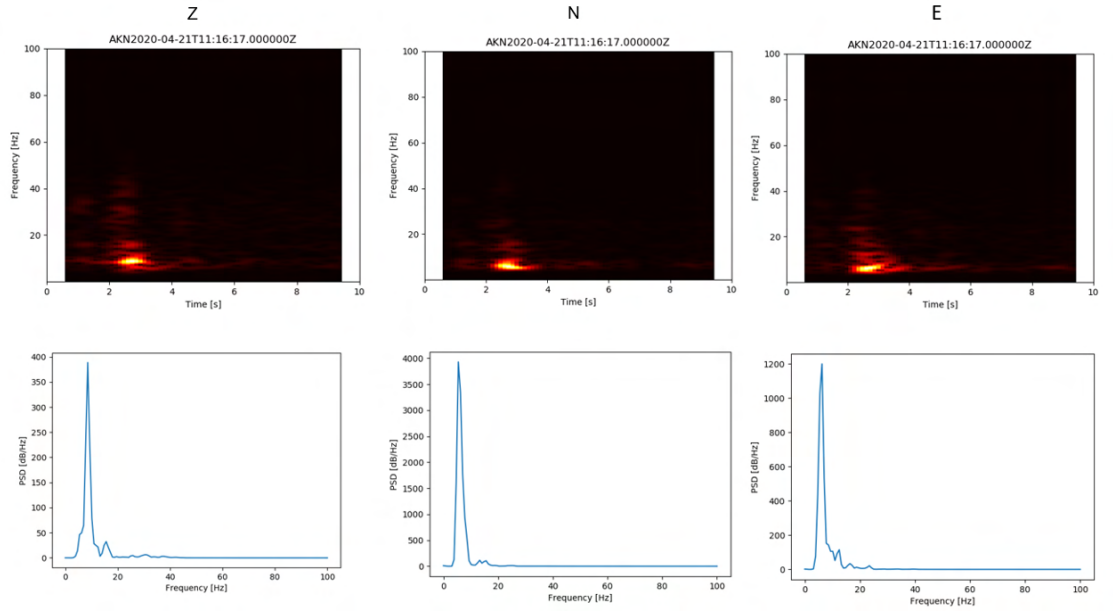

(b)

Figure 39: Example of cross-correlation detection in the low-frequency slopequakes class. The correlation coefficient is 0.75 to the template event (figure 20). See caption of figure 18 for explanation.

6.2.4 Rockfalls

As mentioned earlier, none of the events in event class 3 (rockfalls) were found suitable for template cross-correlation. Only a few events (5 in total) believed to originate from rockfalls were observed during visual inspection of the STA/LTA record, which was not enough to investigate the time distribution of these events. Figure 40.a shows the seismogram of another event in this class. It shares many similarities with the event described in section 5.2 (figure 21), both regarding the waveform shape and frequency content. The waveform shape is quite similar, as it seems to be several spikes in the waveform, although it is not as clear in this case. It has an emergent signal onset and a very clear first arrival is difficult to see. On the other hand, the duration is quite different. This event shows a duration of 5-6 seconds, compared to about 10 seconds for the other event.

The same characteristics in the frequency content between the two events can be observed. The main frequency content is below 20 Hz and most energy is found for frequencies around 10 Hz. Several areas of high energy are seen with time in the spectrograms (figure 40.b). A smaller amount of energy exists for higher frequencies up to about 40 Hz. Cross-correlation of the two waveforms only gave a maximum cross-correlation coefficient of 0.32, although they share many of the same features, showing the challenge of using the template event cross-correlation method for the detection of rockfalls. The event catalog of rockfalls is given in appendix E (table 7).

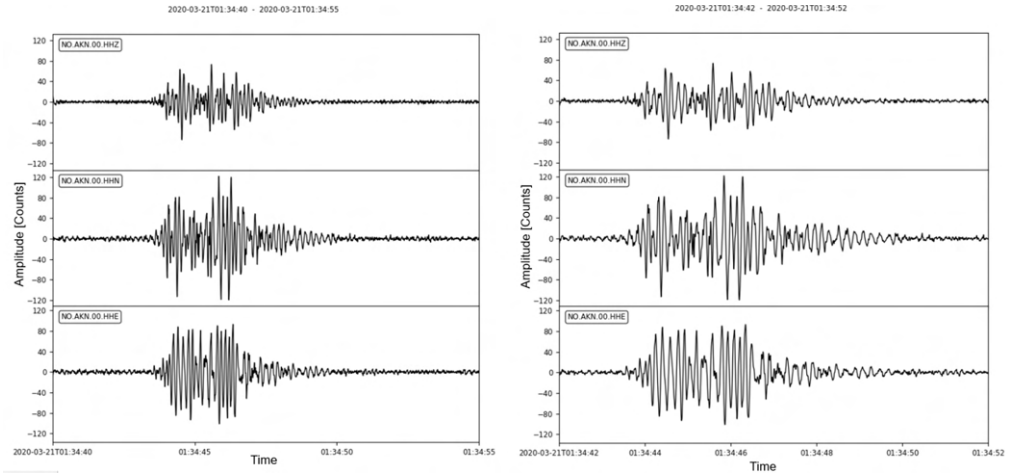

(a)

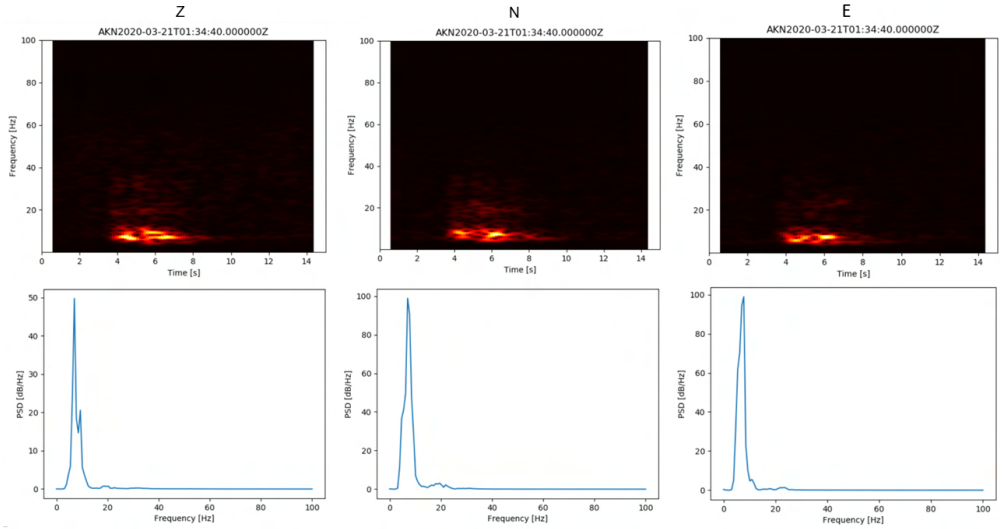

(b)

Figure 40: Example of event defined as a rockfall. See explanation in caption of figure 18. Time windows of seismograms are 15 (left) and 10 seconds (right). Spectrogram and PSD correspond to the time window of 15 seconds.

6.2.5 Other events

As previously mentioned, the total event detections from the template event cross-correlation is only a very small fraction of events registered in the STA/LTA record, and many other types of signals than those classified in one of the three classes were observed. Three examples of events that appeared in the STA/LTA record and are not classified in any of the three proposed classes are given in figure 41. An event with a duration of several minutes can be seen to the left, which is most likely a regional earthquake. A very short lasting event (< 0.5 s) with a spike-like waveform can be observed in the middle. It can perhaps be a local event of very short duration close to the station or noise. To the right, there is an event with a somewhat spindle-shaped waveform and a duration of tens of seconds. This event can maybe relate to some kind of mass flow, perhaps a snow avalanche.

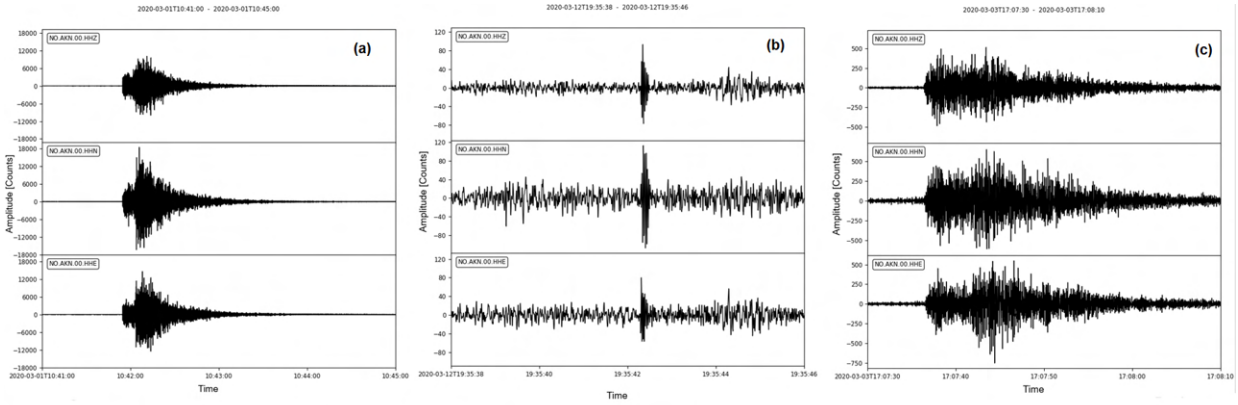

Figure 41: Examples of events in the STA/LTA record that are not classified in any of the proposed classes. a) Event with a duration of several minutes, likely to be a regional earthquake. b) Spike-like waveform of very short duration. c) Event that has a somewhat spindle-shaped waveform, lasting for tens of seconds.

6.3 Estimated source directions

A rose diagram with the back-azimuth distribution estimated using first arrivals of events in the hybrid slopequakes (I) class can be seen in figure 42a. It shows that the source directions are mainly towards north/northwest. In some cases the back-azimuth is pointing in a very different direction, but it is only seen for a few events and the clear trend is in the direction of north/northwest.

The back-azimuth distribution estimated from first arrivals of the hybrid slopequakes (II) class is seen in the rose diagram in figure 42b. It indicates that there are two dominating source directions, towards north/north-northeast and northwest. A couple of events show back-azimuths in very different directions, but the two very clear trends are in the direction of north/north-northeast and northwest.

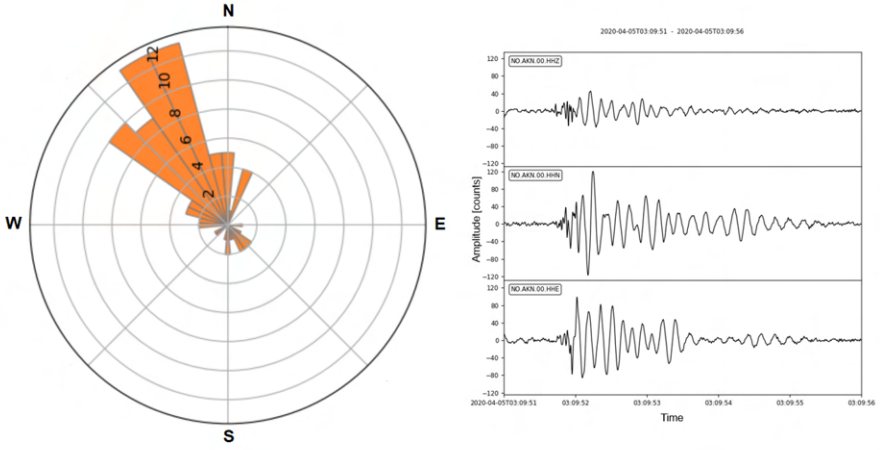

(a)

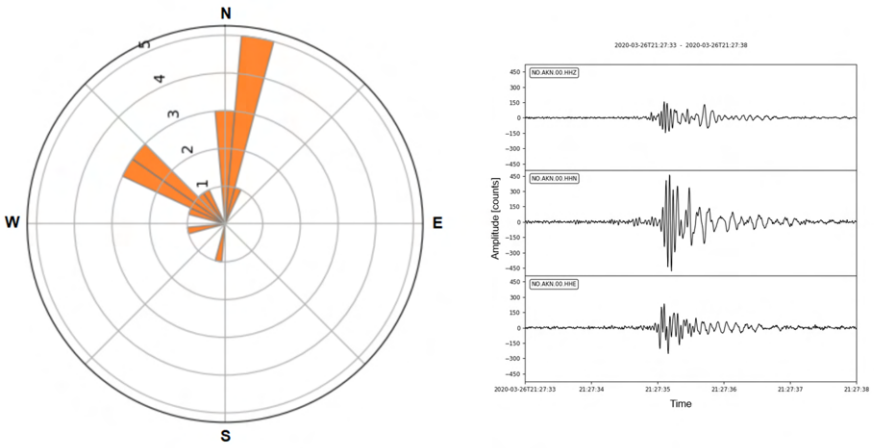

(b)

Figure 42: Back-azimuth distributions. a) Back-azimuth distribution from first arrivals of events in the hybrid slopequakes (I) class (left) and template event in this class (right). b) Back-azimuth distribution from first arrivals of events in the hybrid slopequakes (II) class (left) and template event in this class (right).

7 Discussion

7.1 Event detections and correlation with meteorological data

From the time distribution of STA/LTA detections from 01.03.20 to 15.06.20 (figure 33), some correlation between the overall seismicity and temperature development at the site is indicated. The significant rise in daily detections in the second half of April, as the daily average temperature rises and stays positive for a much longer time than earlier, may imply a connection between increased seismic activity and temperature rise at Åknes during spring. This theory is further supported by the general detection increase in late May/early June, as the temperature stays permanently above $0°C$ after a longer period of negative temperatures.

Furthermore, the time distributions of both hybrid slopequakes and low-frequency slopequakes (figure 34, 36 and 38) imply, similarly to the total amount of STA/LTA detections, that there may exist a correlation between the generation of these types of microseismic events and the temperature development through the analysed period. Especially the peak in slopequake detections in late April/early May, after the significant temperature rise, indicates a relation. It can perhaps relate to water migration in the ground from snow melt during the period of positive temperatures, which may increase the slope deformation and trigger seismic sources generating these signals.

On the other hand, no good correlations were found between the precipitation curve and the time distributions of slopequakes, or the total amount of STA/LTA detections. It may imply that there is actually no correlation, or that the chosen time period does not serve as a good reference for this meteorological parameter as a triggering factor, since much of the precipitations fall during periods of negative temperatures. Seismicity triggered by fluid flow in the ground caused by rainfalls is believed to be an important factor in rockslide areas (Helmstetter et al., 2010), but a link between rainfalls and seismicity might be difficult to see here because much of the precipitations fall as snow.

The indicated correlations between the number of microseismic events and temperature development in this study, agree well with observations of deformation changes on the slope by Grøneng et al. (2011). Their study indicated an acceleration of extensional slope deformations as temperatures become positive during spring, which are likely to generate more local microseismic events.

None of the few events that where classified in event class 3 (rockfalls) were found suitable for template event cross-correlation, which may be explained by several reasons. The total mass of a rockfall as well as the number of fragments can be very variable. Also, it might be a combination of both flowing and bouncing materials generating seismic energy and several contributions are perhaps arriving simultaneously at the station (Provost et al., 2018). Therefore, complex waveforms of variable durations are likely to be generated from rockfalls, which might explain why these signals were not found suitable for cross-correlation.

A lot of other events that have not been classified were also observed, with great variations in features like duration, waveform shape and frequency contents (figure 41). Overall, the events found by cross-correlation only represent a very small fraction of the total STA/LTA detections, implying that there are other types of signals that dominate the seismicity at Åknes. It is possible that most of these events are not related to slope deformation processes, but relates to for example regional events, teleseismic or noise variations. On the other hand, it might also be many undetected local events in the record, and it may be that there are other types of slope related signals that dominate at the site rather than the proposed classes in this study.

7.2 Source directions and source mechanisms

Considering the distribution of back-azimuths (figure 42), it is indicated that the dominant sources creating hybrid slopequakes are found above AKN, in the direction of the back scarp area in the upper part of the slope (figure 3). Taking into account that these are the areas on the slope where the fastest movements earlier have been measured (Heincke et al., 2010), the results are reasonable and agree well with previous observations. It is further supported by the locations of three events in the back scarp area (figure 32) found by Nadège Langet (NORSAR), agreeing pretty well with back-azimuths estimated for the same events from polarization analysis. Also, taking into consideration that increased extensional movements earlier are measured in the back-scarp area during the snowmelt period (Grøneng et al., 2011) and the rise of events in late April/early May, it is possible that the hybrid slopequakes relate to such processes in this area.

However, it is difficult to say something precise about the source mechanisms generating the detected events, when not knowing more about the locations. Some information regarding source mechanisms may be extracted from the characteristics of the waveforms. The very characteristic signature of the hybrid slopequakes, with a significant difference in the frequency content at the beginning of the events compared to later arrivals, may indicate that there are several processes involved. It might relate to hydro-fracturing, where the high-frequency content at the beginning of the signal is generated by brittle mechanisms such as fracturing. The significant lower-frequency arrivals in the later part might correspond to fluid flow through the discontinuities (Chouet, 1988, Benson et al, 2008). Regarding the depth of the sources, the observations of sub-horizontal incidences and indications of surface waves in the waveforms suggest that the sources are in the subsurface, not deep into the basement. The higher detection rate of these signals during the snowmelt period, where meltwater may trigger hydro-fracturing,

supports the idea of this being a possible source mechanism on the slope.

The seismic signature of the events interpreted as low-frequency slopequakes, might indicate slow failure along faults since this process may generate earthquakes of mainly low-frequencies (Thomas et al., 2016). Since the polarization analysis showed some indications of dominating surface waves (Rayleigh waves), it may imply sources at a low depth. A possible interpretation of these events can be slow tensile opening of cracks close to the surface (Deichmann et al., 2000). Effects from propagation can also be an important factor, as attenuation of high-frequency content due to the travelling distance is a possible explanation of why low-frequencies are mainly observed. Overall, it remains a challenging task to interpret the source mechanisms based only on back-azimuths, time distributions and seismic signatures, as there can be a number of explanations.

7.3 Pitfalls, limitations and potensial use of a single-station at Åknes

Based on the overall event detections, it is indicated that the approach of using STA/LTA triggering and template event cross-correlation is rather suitable for the dataset, but there certainly exists possible pitfalls and limitations of the methods used in this study. It must be taken into account that noise variations during the investigated time period may have influenced the event detections. High noise levels might camuflate low amplitude microseismic events. Oppositely, more microseismic events are maybe more easily detected during quiet periods. Therefore, when using only one instrument and not having very good estimates of the noise levels and noise level variations, there is a risk that it has affected the results. Noise may also contain much of the same frequency content as the desired events, hence there is a chance of false events being registered when doing cross-correlation, although the problem was tried avoided by visually inspect many events and only pick those also present in the STA/LTA record.

For seismic events originating from the same source mechanisms, but with dissimilarities seen in the waveform (e.g duration), the template event cross-correlation method certainly has limitations. In this study, events classified as rockfalls were found unsuitable for cross-correlation, probably due to more complex waveforms and varying durations compared to the slopequakes classes. Another limitation of using template matching for detection of events is the determination of templates, as one has to know the data before using it, which can be a very time consuming process. It might also be that the parameters set for STA/LTA event detection and template events cross-correlation were not the best fit for the analysed data, although a lot of initial testing was performed. Both methods used for event detection are relatively simple and a lot of information are likely to get lost on the way, so in a study where the overall aim is to classify events, more features should probably be taken into account. For example, by using sophisticated machine learning algorithms taking into account many features, it might be easier to classify events. For the surface network at the site this has already been done by Silverberg (2020). There, only signals visible on several geophones at the same time are considered, making it easier to validate real events versus noise. In the end it all depends on the

level of details and the kind of analysis to perform.

Since it was not possible to easily separate different phase arrivals from the polarization analysis, there are high uncertainties regarding the back-azimuth estimations and it may only serve as a brief indication of dominating source directions. It might be due to short source to receiver distances and almost simultaneously arriving phases, which breaks down the method of using polarization analysis for direction finding from a single-station.

In addition to the source-receiver distance, the complexity and inhomogeneity of the subsurface are likely to affect the polarization of waves (Bormann, 2009). Seismic waves only have a clean polarization in homogeneous and isotropic materials, and effects such as scattering of waves may influence the polarization. A P-wave recorded by a seismometer at the surface is a combination of three waves, the incoming P-wave, the converted wave (SV-wave) and reflected P-wave, thus the observed polarization is expected to be not perfectly linear (Nuttli et al., 1961). As a consequence, considering the inhomogeneous material on the slope, it can have had an impact on the identification of P-wave arrivals. Also, if there are arrivals from different events at the same time, it will surely affect the polarization and make the method for direction finding less applicable. On the other hand, scattering and conversion of waves around the seismometer are believed to have only small effects on the P-wave angle (Park et al., 2018), even though it may affect the polarization. In Köhler et al. (2019) the waves were simpler and the method applied for direction finding was easier to use as the propagation was in the ice, which is much more homegeneous than the material on a rockslope.

Observations from the polarization analysis of local slopequakes in this study agree somewhat with observations from Provost et al. (2018) and Tonnellier et al. (2013). Their studies indicated similarly to the findings here, that for these types of events a clear onset is often hard to determine and different phase arrivals are in most cases very difficult to separate, but it may sometimes be possible to identify P-waves in the high-frequency first arrivals.

However, the overall findings reveal that the use of a three-components broadband seismometer can be feasible for analysis of microseismicity at Åknes and that the seismometer is useful for local events. On the basis of the findings from polarization analysis, especially the agreement between some known event locations and back-azimuths, it is indicated that it in some cases can potentially be used for determining source directions, although further investigations are needed to verify the method.

8 Conclusions

Microseismicity from the period 01.03.20 to 15.06.20 at the Åknes unstable rockslope has been analysed, using data from a three-components broadband seismometer (AKN) installed at the site. Based on the overall detections, it can be concluded that the single-station record can potentially be used for local microseismicity at Åknes. The use of STA/LTA triggering and template event cross-correlation is feasible for event detection in the AKN data, as it resulted in the detection of many microseismic events. Three different microseismic event classes were determined: 1) hybrid slopequakes, 2) low-frequency slopequakes and 3) rockfalls. Some correlation between slopequakes and temperature was indicated, as a rise in detections was found when temperatures increased during spring. It is indicated that the use of polarization analysis for source direction determination might be applicable for some local events, but no conclusions can be drawn regarding dominating source directions, as there are too high uncertainties. However, further studies are required to reveal the full potential of using a single-station record at Åknes, both as regards detection of local events and polarization analysis.

Considering that the amount of events detected by cross-correlation is only a very small fraction of the total STA/LTA detections, there are a lot more data from AKN that should be analysed in future work. This may reveal other types of local events that are of interest for the slope monitoring. Further studies should take into consideration data from other time periods, since the investigated time period is only a small part of the year. It will give a better basis of comparison for the correlation between meteorological conditions and the time distribution of different microseismic events. By also studying and comparing data for the same time period for different years it could be easier to see if there is a correlation or not. It could also be a good idea to plot and compare other types of meteorological data to event detections over a longer time period, for example snow data.

Furthermore, noise levels and noise level variations should be taken more into account, which may give more reliable results regarding the time distribution of certain signals and their correlation with meteorological data. Other methods should be tested, for example machine learning algorithms, which might be more applicable for event detection and classification. Another idea is to compare more events detected on the AKN station with data from the geophone network. By locating more events with the geophone network and compare it to back-azimuths determined from AKN, it will be easier to see how reliable it is to use polarization analysis for source direction determination.

Appendices

A Cross-correlation threshold calibration

In this appendix, initial cross-correlation detections for the hybrid slopequakes classes, which were used for setting the cross-correlation thresholds are given (figure 43 and 44).

Hybrid slopequakes (I)

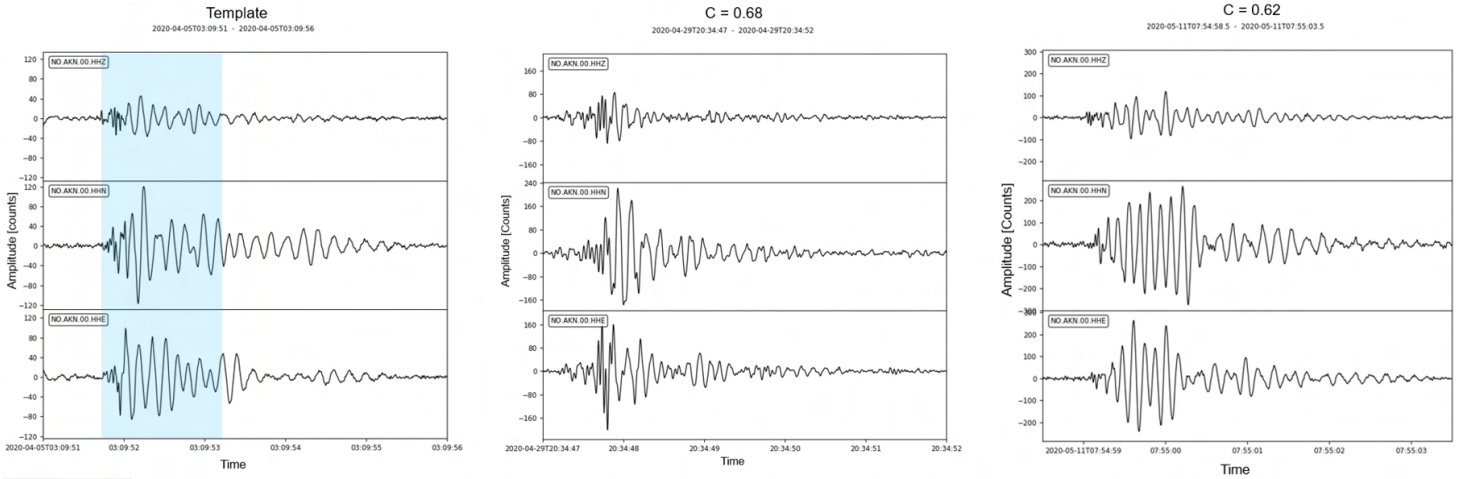

(a)

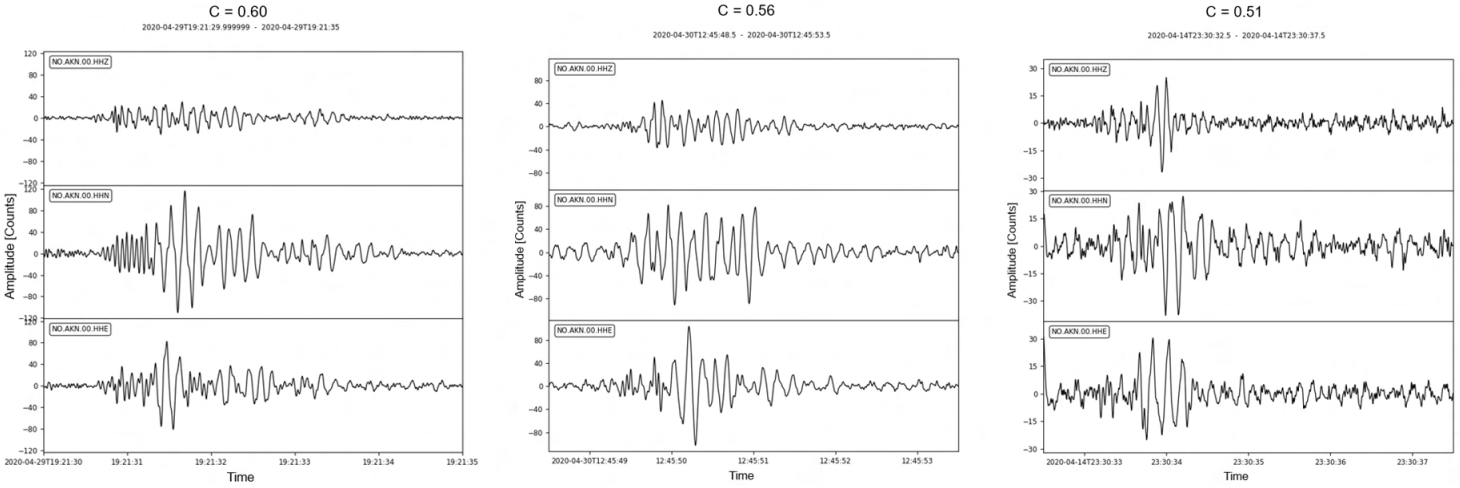

(b)

Figure 43: Hybrid slopequakes (I) class cross-correlation threshold calibration. C = cross-correlation coefficient. a) Seismogram of template waveform and the time window (blue) used for cross-correlation, and events with correlations of 0.68 and 0.62 with the template. b) Examples of waveforms with correlations of 0.60, 0.56 and 0.51 with the template event in a). A high degree of similarity was found from C = 0.60 and above, which was used as threshold for template event cross-correlation.

Hybrid slopequakes (II)

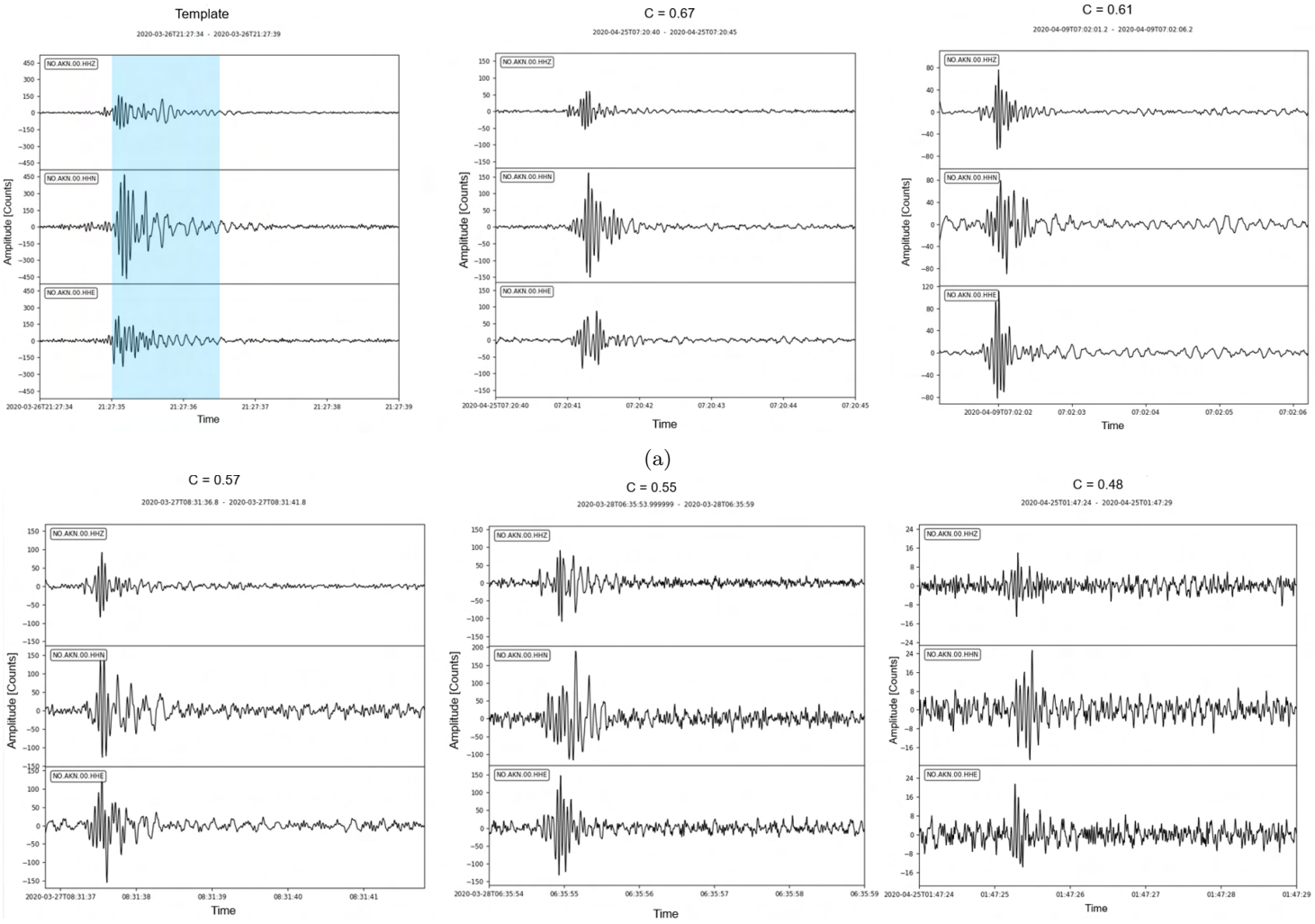

Figure 44: Hybrid slopequakes (II) class cross-correlation threshold calibration. C = cross-correlation coefficient. a) Seismogram of template waveform and the time window (blue) used for cross-correlation, and events with correlations of 0.67 and 0.61 with the template. b) Examples of waveforms with correlations of 0.57, 0.55 and 0.48 with the template event in a). A high degree of similarity was found from C = 0.55 and above, which was used as threshold for template event cross-correlation.

B Polarization analysis of regional earthquakes

This appendix shows the two other regional earthquakes, used as reference for P-wave first arrival polarization and inspection of the vertical component (figure 45 and 46).

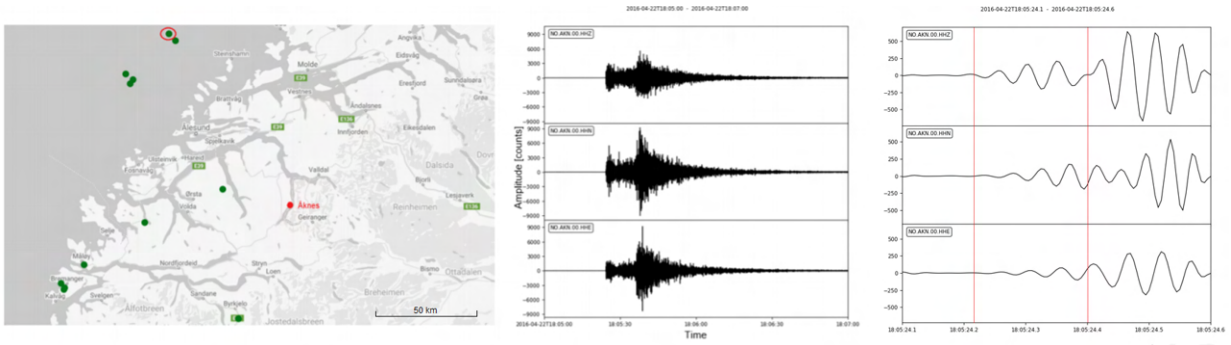

(a)

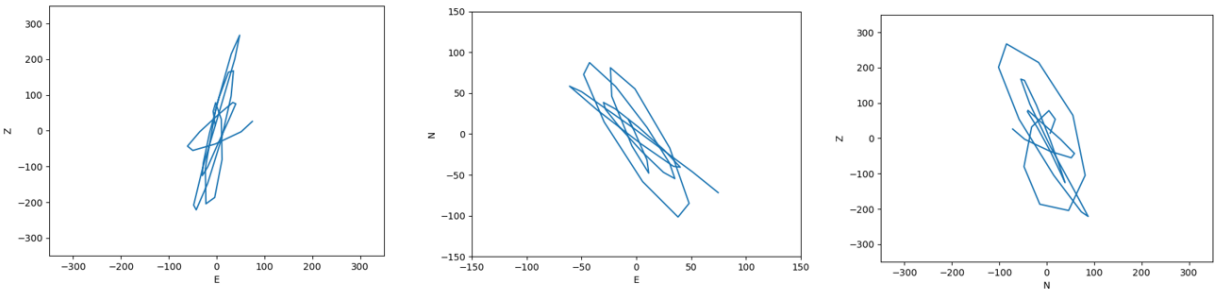

(b)

Figure 45: Polarization analysis of regional earthquake of magnitude 2.7. a) From left to right: location of event (marked by red circle), seismogram in 2 minutes time window and zoom in on first arrivals and time window used for the analysis (marked by red vertical lines) The location is towards the northwest from Åknes. b) Amplitude cross-plots in the two vertical planes (E-Z and N-Z) and the horizontal plane (E-N). It shows a near vertical incidence angle and indicates a source direction towards the northwest.

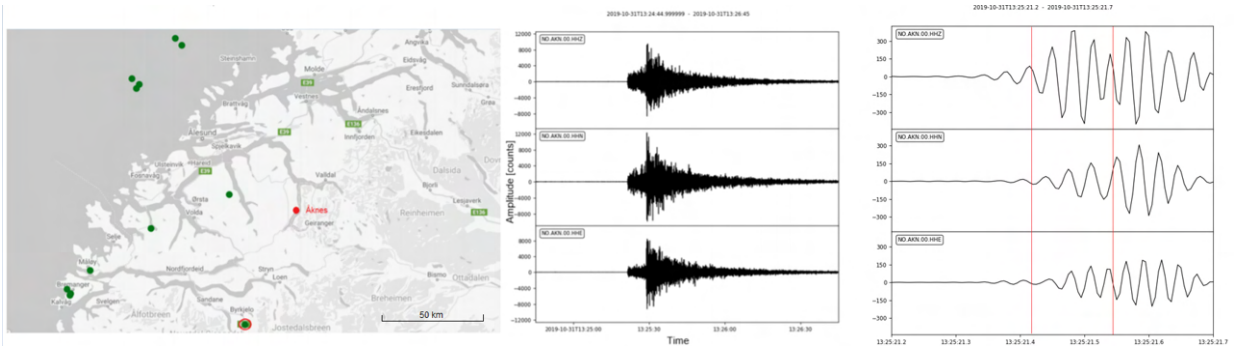

(a)

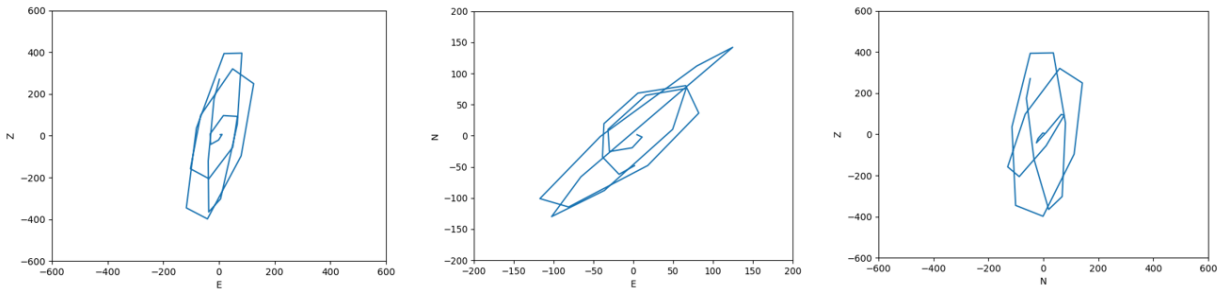

(b)

Figure 46: Polarization analysis of regional earthquake of magnitude 2.5. a) From left to right: location of event (marked by red circle), seismogram in 2 minutes time window and zoom in on first arrivals and time window used for the analysis (marked by red vertical lines). The location is towards the southwest from Åknes. b) Amplitude cross-plots in the two vertical planes (E-Z and N-Z) and the horizontal plane (E-N). A near vertical incidence angle and a source direction towards the southwest are indicated.

C Polarization analysis of local events

In this appendix, more examples from the polarization analysis of events in the slopequakes classes and rockfalls class are provided (figure 47-53).

Hybrid slopequakes (I)

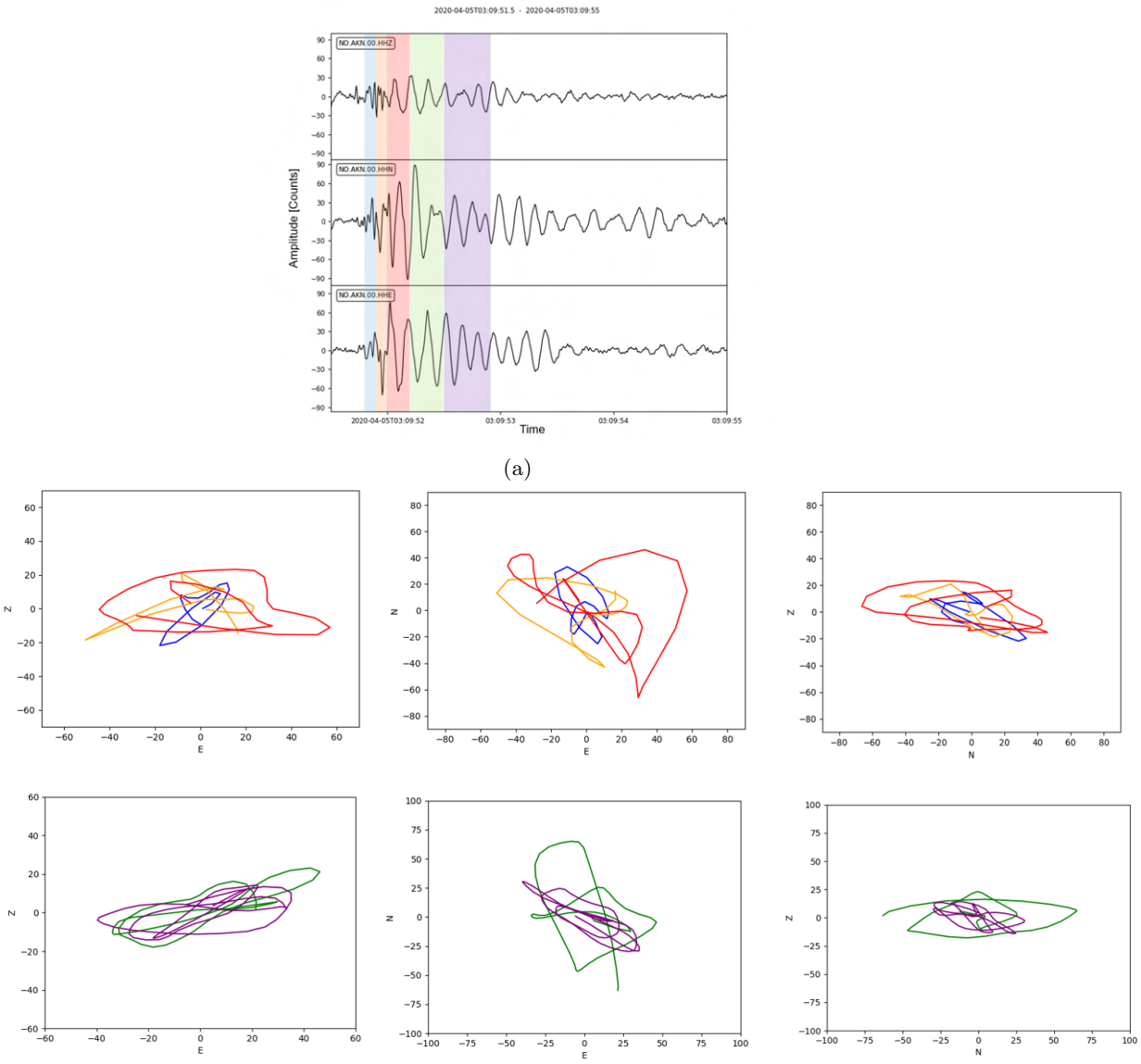

(a)

(b)

Figure 47: Example of polarization analysis of an event in the hybrid slopequakes (I) class. a) Seismogram of event with colored time windows used for the analysis. b) Amplitude cross-plots with colors corresponding to the different time windows.

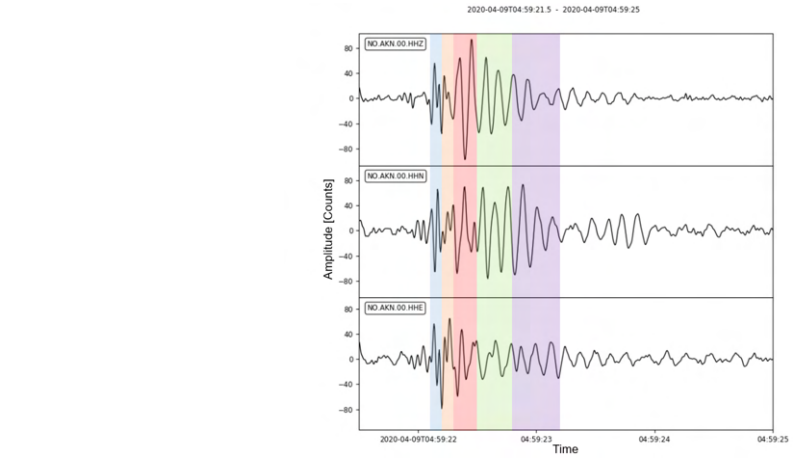

(a)

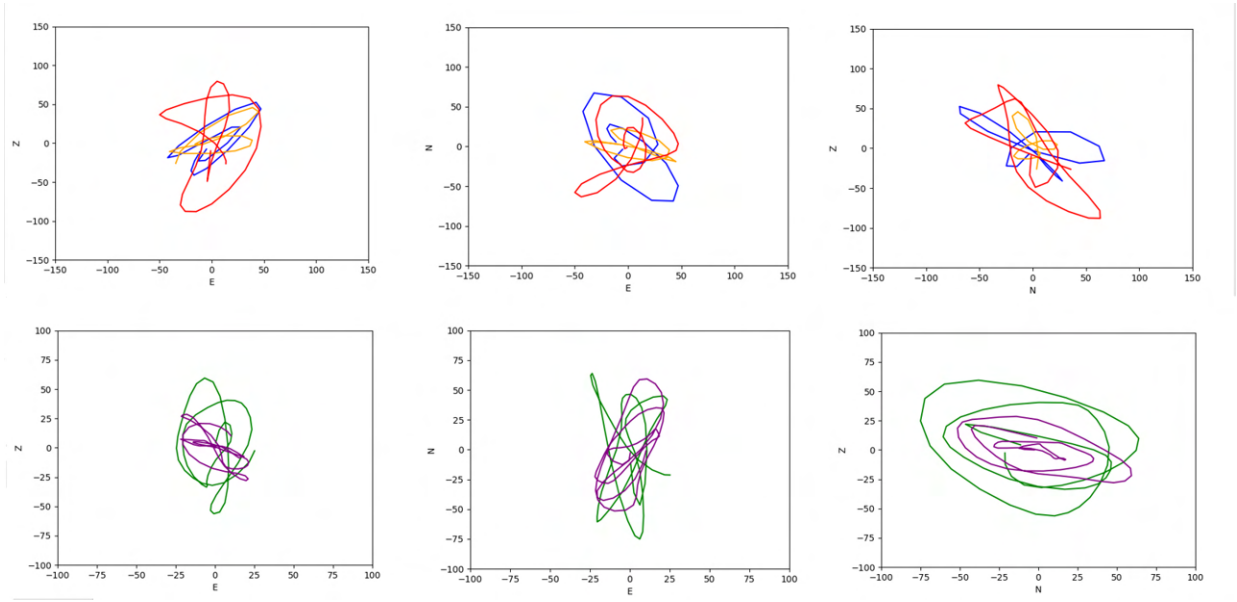

(b)

Figure 48: Example of polarization analysis of an event in the hybrid slopequakes (I) class. See description in caption of figure 47.

Hybrid slopequakes (II)

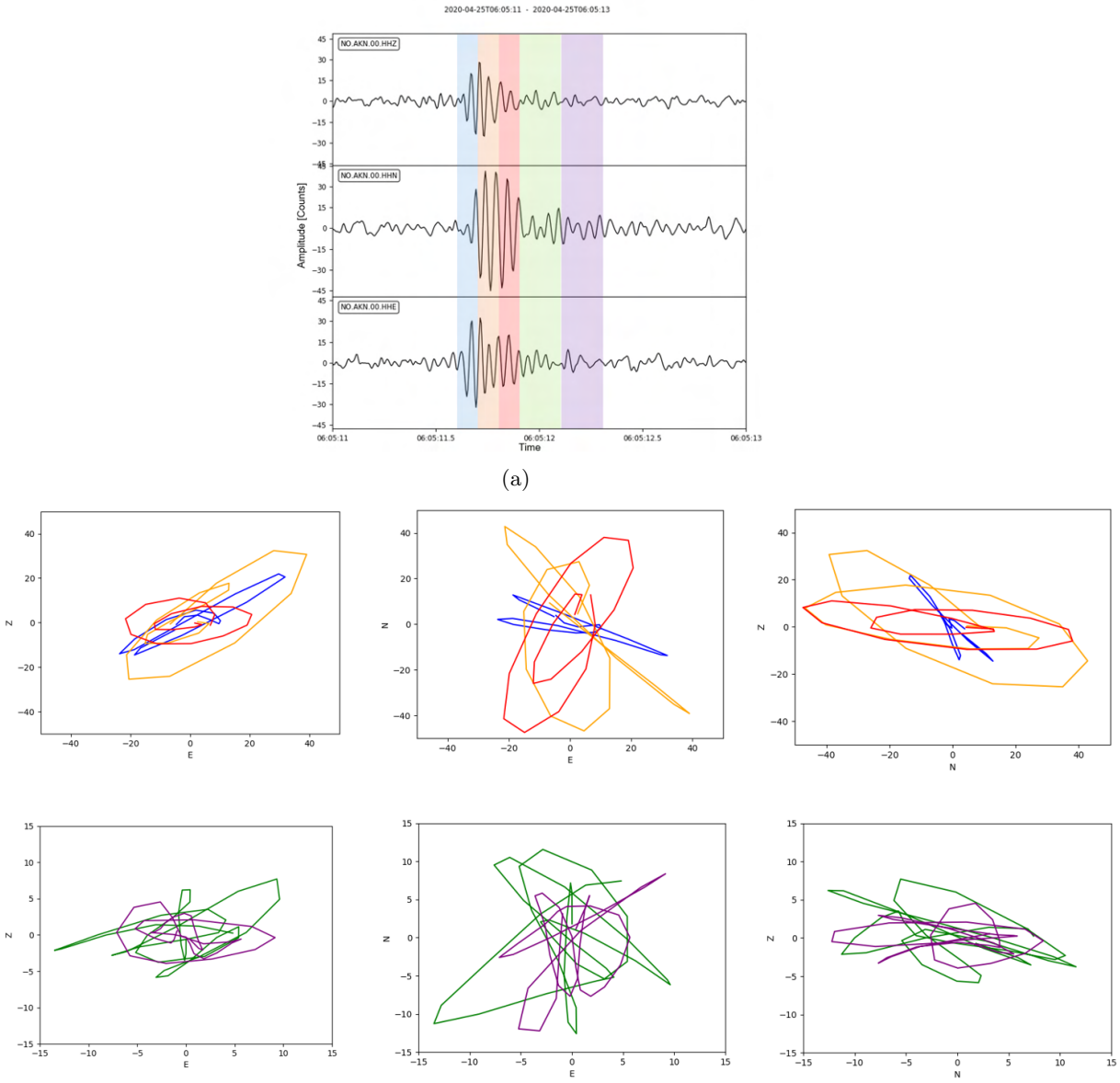

(a)

(b)

Figure 49: Example of polarization analysis of an event in the hybrid slopequakes (II) class. See description in caption of figure 47.

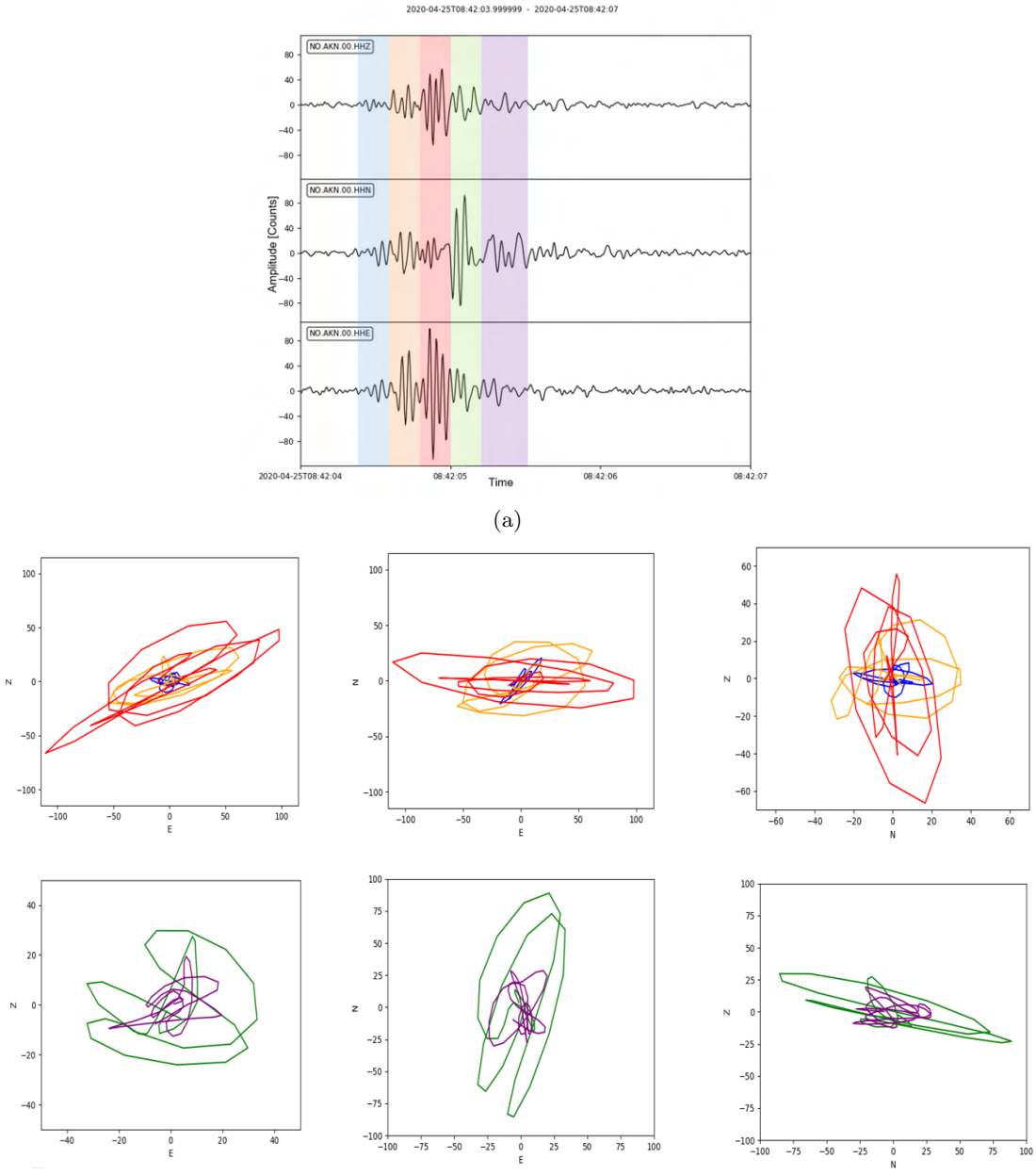

Figure 50: Example of polarization analysis of an event in the hybrid slopequakes (II) class. See description in caption of figure 47.

Low-frequency slopequakes

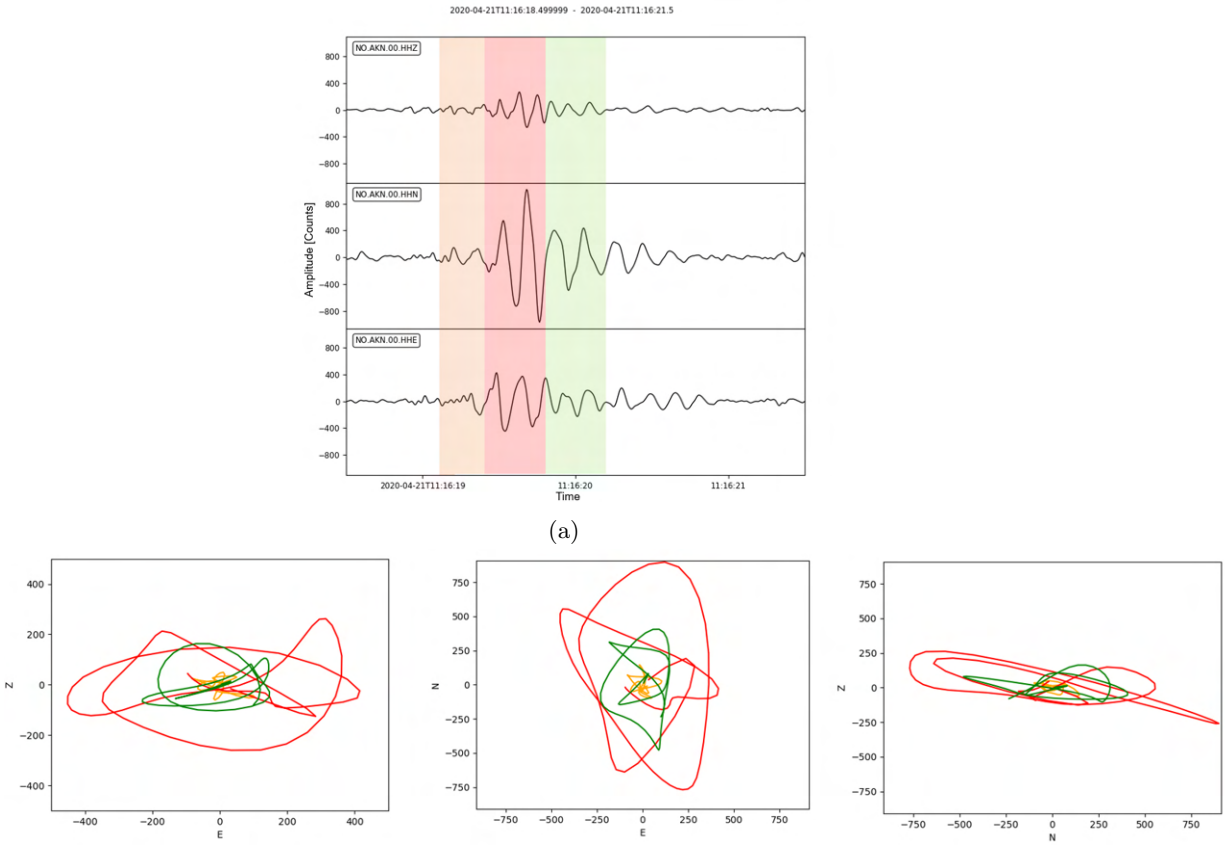

(a)

(b)

Figure 51: Example of polarization analysis of an event in the low-frequency slopequakes class. See description in caption of figure 47.

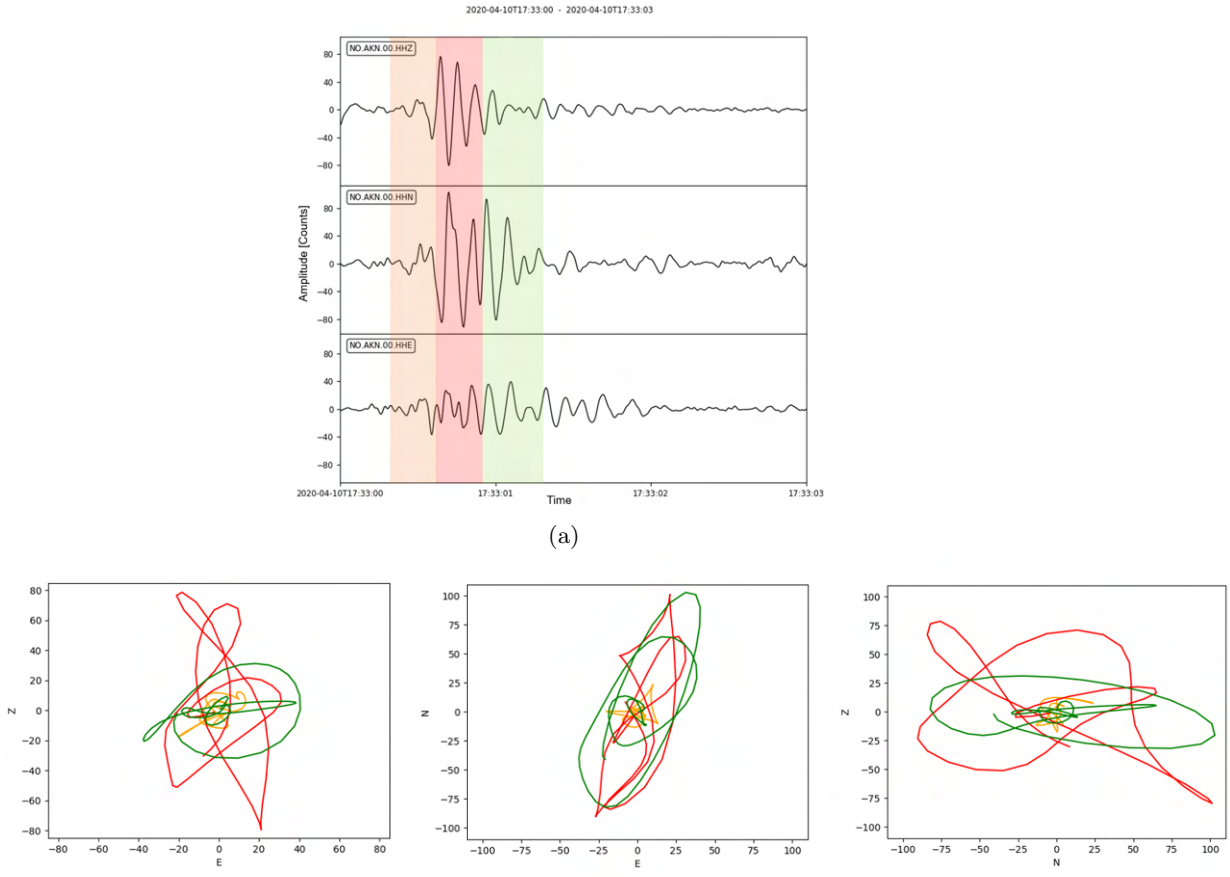

(a)

(b)

Figure 52: Example of polarization analysis of an event in the low-frequency slopequakes class. See description in caption of figure 47.

Rockfalls

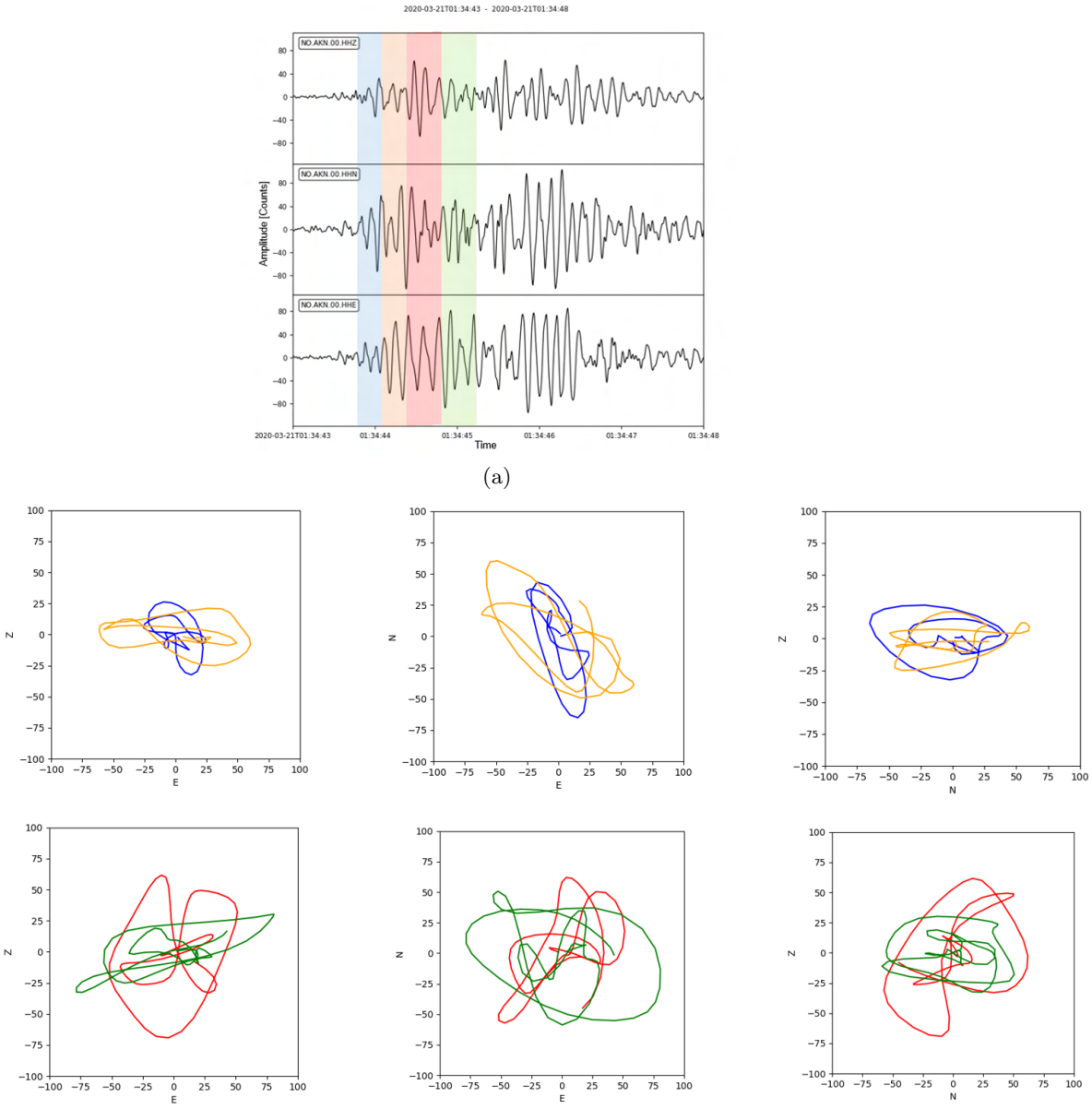

(a)

(b)

Figure 53: Example of polarization analysis of an event in the rockfalls class. See description in caption of figure 47.

D Polarization analysis using rotated coordinate system

In figure 54, 55 and 56 examples of polarization analysis of events in the slopequakes classes in the rotated coordinate system are given. They are the same events as analysed in the ZNE-system in figure 25, 26 and 27.

Hybrid slopequakes (I)

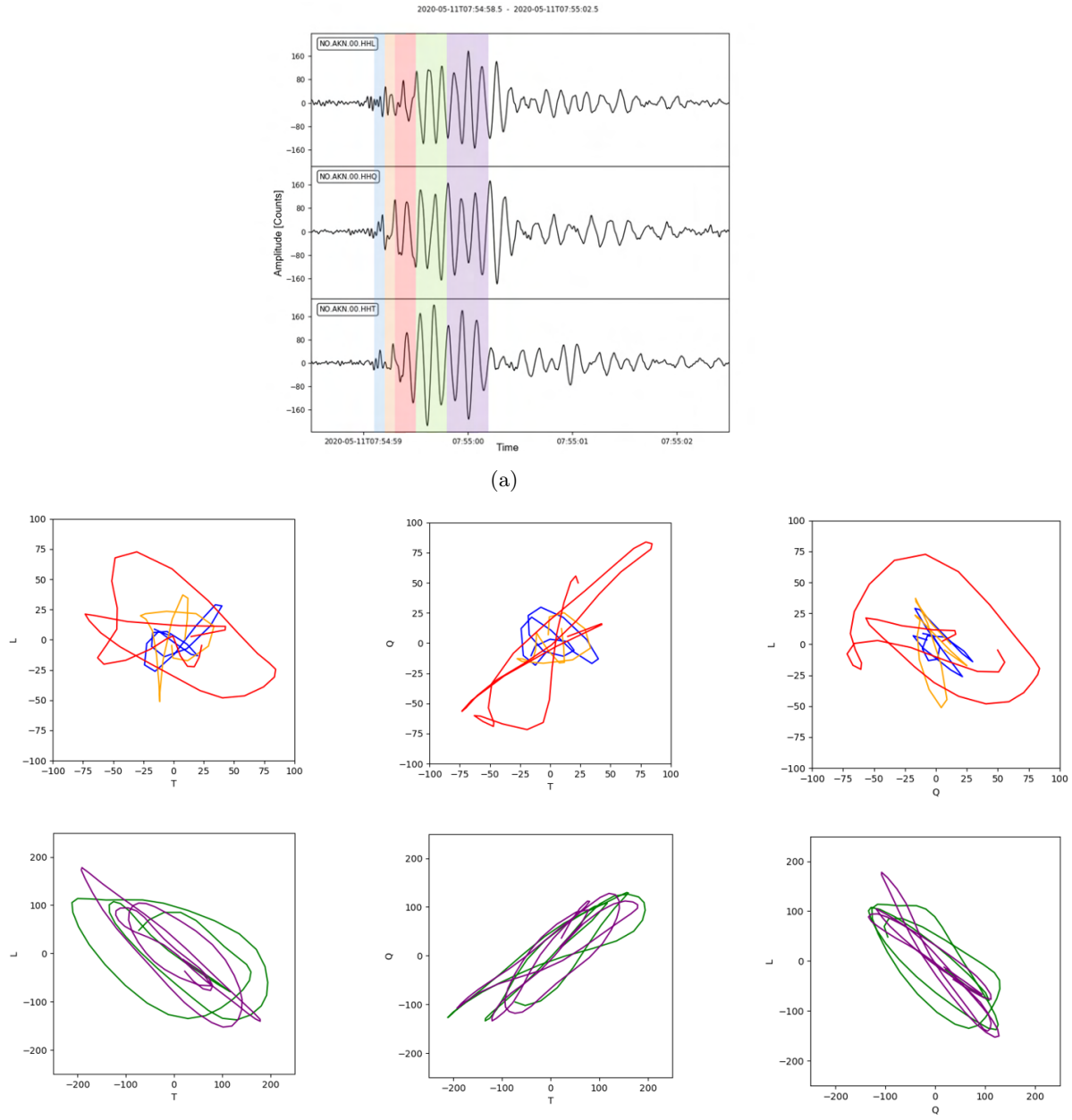

(a)

(b)

Figure 54: Example of polarization analysis of an event in the hybrid slopequakes (I) class in rotated system. See description in caption of figure 47.

Hybrid slopequakes (II)

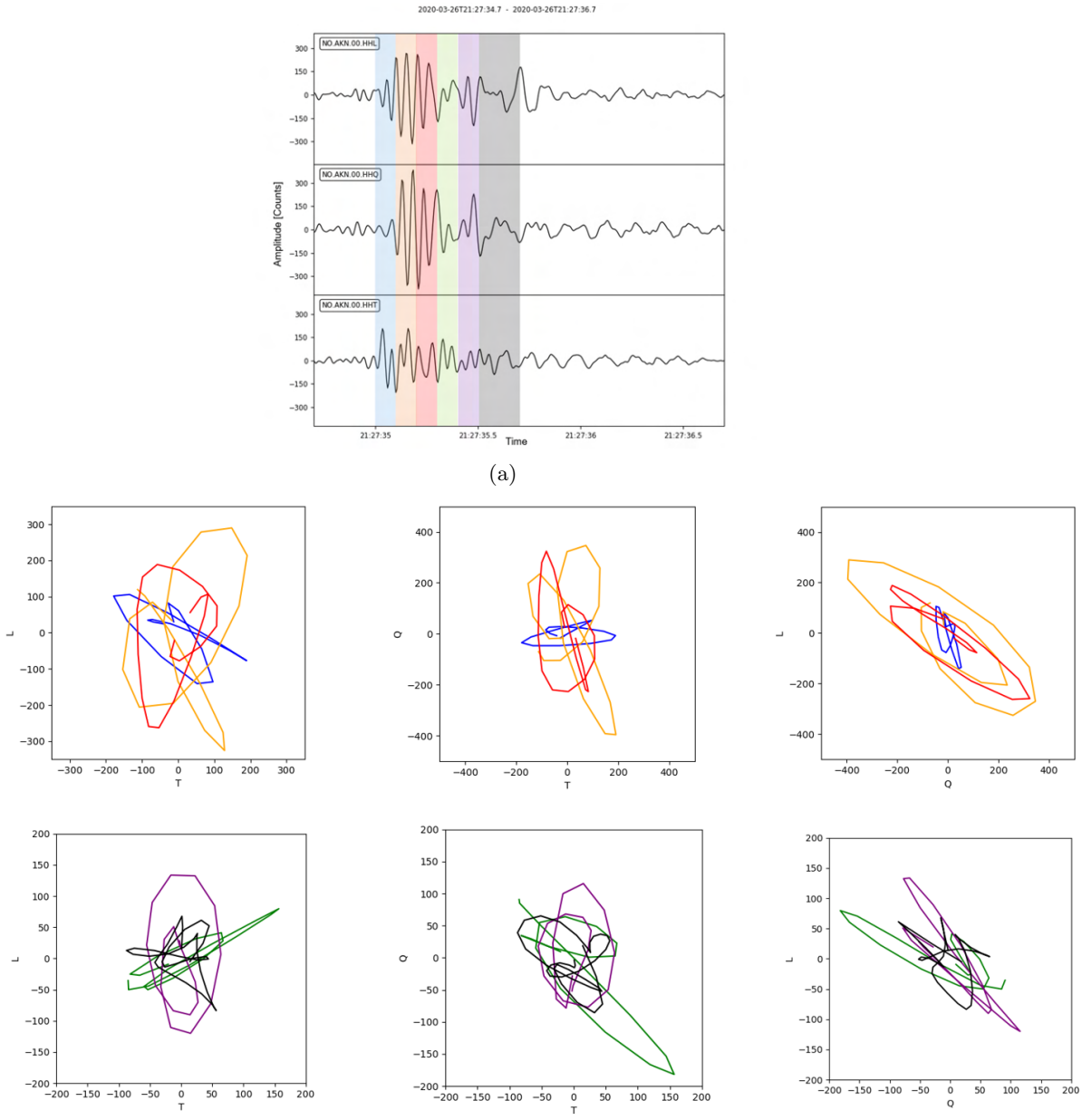

(a)

(b)

Figure 55: Example of polarization analysis of an event in the hybrid slopequakes (II) class in rotated system. See description in caption of figure 47.

Low-frequency slopequakes

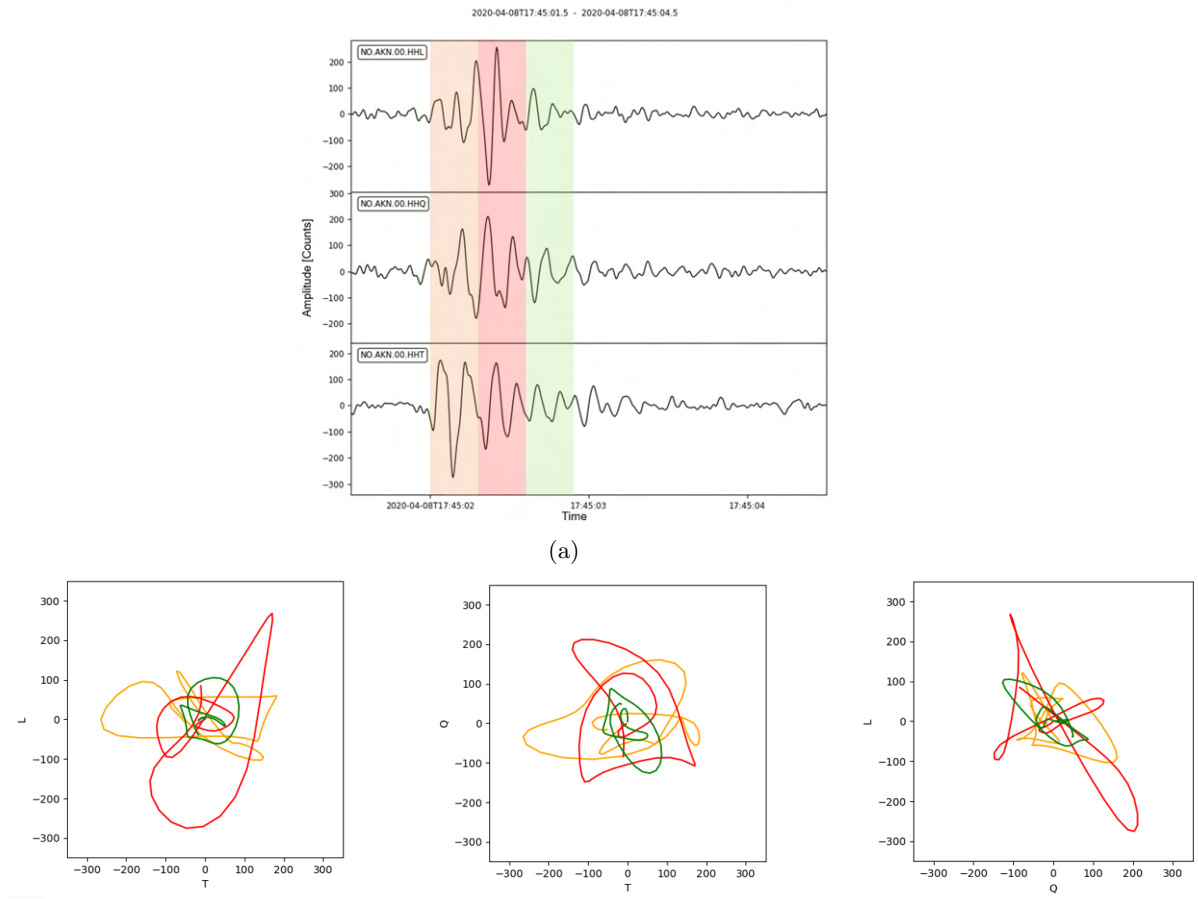

(a)

(b)

Figure 56: Example of polarization analysis of an event in the low-frequency slopequakes class in rotated system. See description in caption of figure 47.

E Event catalogs

Hybrid slopequakes (I)

Table 4: Template event cross-correlation detections of hybrid slopequakes (I).

Event	Time	Correlation coeff.	Template
1	2020-03-03T13:20:06.199999Z	0.645230	2020-04-05T03:09:51.88
2	2020-03-15T10:25:39.370000Z	0.634695	2020-04-05T03:09:51.88
3	2020-03-18T19:26:33.665000Z	0.623200	2020-04-05T03:09:51.88
4	2020-03-27T23:41:22.130000Z	0.624500	2020-04-05T03:09:51.88
5	2020-03-29T00:30:45.625000Z	0.620091	2020-04-05T03:09:51.88
6	2020-03-29T01:23:59.785000Z	0.606399	2020-04-05T03:09:51.88
7	2020-03-29T07:07:11.180000Z	0.610273	2020-04-05T03:09:51.88
8	2020-03-29T07:08:59.405000Z	0.607820	2020-04-05T03:09:51.88
9	2020-03-29T08:45:08.240000Z	0.609720	2020-04-05T03:09:51.88
10	2020-03-29T12:44:37.670000Z	0.645098	2020-04-05T03:09:51.88
11	2020-03-30T06:18:36.120000Z	0.612268	2020-04-05T03:09:51.88
12	2020-03-30T08:10:36.710000Z	0.606243	2020-04-05T03:09:51.88
13	2020-03-30T16:37:41.450000Z	0.635110	2020-04-05T03:09:51.88
14	2020-03-31T11:46:04.290000Z	0.601242	2020-04-05T03:09:51.88
15	2020-04-03T02:37:34.715000Z	0.657946	2020-04-05T03:09:51.88
16	2020-04-05T03:09:51.880000Z	1.000000	2020-04-05T03:09:51.88
17	2020-04-05T10:08:25.495000Z	0.651614	2020-04-05T03:09:51.88
18	2020-04-09T04:59:22.165000Z	0.630449	2020-04-05T03:09:51.88
19	2020-04-10T00:30:35.140000Z	0.616728	2020-04-05T03:09:51.88
20	2020-04-11T15:03:40.365000Z	0.664350	2020-04-05T03:09:51.88
21	2020-04-11T17:55:00.815000Z	0.601909	2020-04-05T03:09:51.88
22	2020-04-17T03:33:17.135000Z	0.648966	2020-04-05T03:09:51.88
23	2020-04-18T14:57:56.445000Z	0.649282	2020-04-05T03:09:51.88
24	2020-04-20T13:10:54.970000Z	0.752916	2020-04-05T03:09:51.88
25	2020-04-20T20:16:55.080000Z	0.639831	2020-04-05T03:09:51.88
26	2020-04-21T08:45:37.020000Z	0.626117	2020-04-05T03:09:51.88
27	2020-04-21T14:38:00.530000Z	0.642879	2020-04-05T03:09:51.88
28	2020-04-21T18:41:05.075000Z	0.617604	2020-04-05T03:09:51.88
29	2020-04-22T02:23:21.060000Z	0.614643	2020-04-05T03:09:51.88
30	2020-04-23T05:40:34.945000Z	0.612035	2020-04-05T03:09:51.88
31	2020-04-23T10:58:30.695000Z	0.611702	2020-04-05T03:09:51.88
32	2020-04-23T12:49:55.705000Z	0.609347	2020-04-05T03:09:51.88
33	2020-04-24T11:45:41.150000Z	0.617058	2020-04-05T03:09:51.88
34	2020-04-25T07:50:31.520000Z	0.619174	2020-04-05T03:09:51.88
35	2020-04-25T11:57:44.065000Z	0.620503	2020-04-05T03:09:51.88

Event	Time	Correlation coeff.	Template
36	2020-04-25T21:48:41.665000Z	0.633568	2020-04-05T03:09:51.88
37	2020-04-26T03:46:59.255000Z	0.614528	2020-04-05T03:09:51.88
38	2020-04-26T09:36:24.490000Z	0.602473	2020-04-05T03:09:51.88
39	2020-04-27T03:22:26.615000Z	0.601242	2020-04-05T03:09:51.88
40	2020-04-27T06:31:28.455000Z	0.627076	2020-04-05T03:09:51.88
41	2020-04-27T07:04:50.150000Z	0.629253	2020-04-05T03:09:51.88
42	2020-04-27T12:49:00.660000Z	0.619149	2020-04-05T03:09:51.88
43	2020-04-27T13:41:26.435000Z	0.610629	2020-04-05T03:09:51.88
44	2020-04-28T05:22:38.340000Z	0.620205	2020-04-05T03:09:51.88
45	2020-04-28T14:28:41.535000Z	0.634151	2020-04-05T03:09:51.88
46	2020-04-29T18:23:47.845000Z	0.638815	2020-04-05T03:09:51.88
47	2020-04-29T19:21:32.030000Z	0.601410	2020-04-05T03:09:51.88
48	2020-04-29T20:34:47.480000Z	0.682386	2020-04-05T03:09:51.88
49	2020-04-30T12:20:20.555000Z	0.634462	2020-04-05T03:09:51.88
50	2020-05-01T03:56:35.760000Z	0.604834	2020-04-05T03:09:51.88
51	2020-05-01T04:47:02.595000Z	0.631386	2020-04-05T03:09:51.88
52	2020-05-02T02:54:33.900000Z	0.607868	2020-04-05T03:09:51.88
53	2020-05-02T12:52:37.840000Z	0.623468	2020-04-05T03:09:51.88
54	2020-05-04T08:23:55.225000Z	0.663544	2020-04-05T03:09:51.88
55	2020-05-06T22:43:58.975000Z	0.625927	2020-04-05T03:09:51.88
56	2020-05-11T07:55:00.745000Z	0.619991	2020-04-05T03:09:51.88
57	2020-05-11T22:45:36.505000Z	0.666042	2020-04-05T03:09:51.88
58	2020-05-21T09:59:37.184999Z	0.635436	2020-04-05T03:09:51.88
59	2020-05-22T01:48:08.210000Z	0.600703	2020-04-05T03:09:51.88
60	2020-05-22T06:24:17.155000Z	0.614066	2020-04-05T03:09:51.88
61	2020-05-22T13:25:17.395000Z	0.645795	2020-04-05T03:09:51.88
62	2020-05-22T20:46:00.515000Z	0.636996	2020-04-05T03:09:51.88
63	2020-05-24T12:35:01.235000Z	0.627017	2020-04-05T03:09:51.88
64	2020-05-25T16:51:49.659999Z	0.646212	2020-04-05T03:09:51.88
65	2020-05-27T13:25:28.415000Z	0.639305	2020-04-05T03:09:51.88
66	2020-05-27T14:24:33.240000Z	0.642615	2020-04-05T03:09:51.88
67	2020-05-29T10:23:47.945000Z	0.604883	2020-04-05T03:09:51.88
68	2020-05-30T02:04:04.934999Z	0.631687	2020-04-05T03:09:51.88
69	2020-05-30T08:31:55.529999Z	0.649658	2020-04-05T03:09:51.88
70	2020-05-30T12:10:11.794999Z	0.623698	2020-04-05T03:09:51.88
71	2020-05-31T00:57:34.250000Z	0.606875	2020-04-05T03:09:51.88
72	2020-05-31T18:29:39.045000Z	0.612048	2020-04-05T03:09:51.88
73	2020-06-01T00:39:19.290000Z	0.602163	2020-04-05T03:09:51.88
74	2020-06-01T05:24:43.780000Z	0.606436	2020-04-05T03:09:51.88
75	2020-06-01T08:08:25.695000Z	0.619355	2020-04-05T03:09:51.88
76	2020-06-01T17:46:16.095000Z	0.637055	2020-04-05T03:09:51.88

Event	Time	Correlation coeff.	Template
77	2020-06-03T15:53:07.000000Z	0.606465	2020-04-05T03:09:51.88
78	2020-06-05T08:01:20.880000Z	0.626379	2020-04-05T03:09:51.88
79	2020-06-05T08:33:35.240000Z	0.614825	2020-04-05T03:09:51.88
80	2020-06-06T15:21:22.575000Z	0.603263	2020-04-05T03:09:51.88
81	2020-06-09T03:29:11.765000Z	0.608583	2020-04-05T03:09:51.88
82	2020-06-10T08:49:05.735000Z	0.625868	2020-04-05T03:09:51.88
83	2020-06-10T20:25:48.315000Z	0.609112	2020-04-05T03:09:51.88
84	2020-06-11T05:40:29.960000Z	0.633642	2020-04-05T03:09:51.88
85	2020-06-12T21:18:46.555000Z	0.645851	2020-04-05T03:09:51.88
86	2020-06-13T08:32:34.040000Z	0.644692	2020-04-05T03:09:51.88

Hybrid slopequakes (II)

Table 5: Template event cross-correlation detections of hybrid slopequakes (II).

Event	Time	Correlation coeff.	Template
1	2020-03-13T09:41:59.765000Z	0.545351	2020-03-26T21:27:35.03
2	2020-03-18T22:00:28.930000Z	0.546098	2020-03-26T21:27:35.03
3	2020-03-19T11:58:07.565000Z	0.549888	2020-03-26T21:27:35.03
4	2020-03-22T18:45:33.795000Z	0.544357	2020-03-26T21:27:35.03
5	2020-03-24T17:18:45.799999Z	0.559732	2020-03-26T21:27:35.03
6	2020-03-26T21:27:35.030000Z	1.000000	2020-03-26T21:27:35.03
7	2020-03-27T08:31:37.350000Z	0.572238	2020-03-26T21:27:35.03
8	2020-03-28T03:44:43.655000Z	0.557380	2020-03-26T21:27:35.03
9	2020-03-28T06:35:54.755000Z	0.554026	2020-03-26T21:27:35.03
10	2020-03-28T20:05:05.400000Z	0.647425	2020-03-26T21:27:35.03
11	2020-03-31T21:39:56.690000Z	0.570111	2020-03-26T21:27:35.03
12	2020-04-09T07:02:01.805000Z	0.612061	2020-03-26T21:27:35.03
13	2020-04-24T10:46:55.195000Z	0.560093	2020-03-26T21:27:35.03
14	2020-04-25T01:01:36.205000Z	0.622449	2020-03-26T21:27:35.03
15	2020-04-25T01:47:08.570000Z	0.647910	2020-03-26T21:27:35.03
16	2020-04-25T06:05:11.510000Z	0.584388	2020-03-26T21:27:35.03
17	2020-04-25T07:20:41.065000Z	0.670401	2020-03-26T21:27:35.03
18	2020-04-25T16:37:06.620000Z	0.566850	2020-03-26T21:27:35.03
19	2020-04-25T08:42:04.685000Z	0.600558	2020-03-26T21:27:35.03
20	2020-04-25T22:19:37.685000Z	0.556509	2020-03-26T21:27:35.03
21	2020-04-25T23:02:35.205000Z	0.561279	2020-03-26T21:27:35.03
22	2020-04-26T00:18:21.595000Z	0.602674	2020-03-26T21:27:35.03
23	2020-04-26T18:03:04.370000Z	0.718364	2020-03-26T21:27:35.03
24	2020-04-27T01:06:34.625000Z	0.555232	2020-03-26T21:27:35.03

Event	Time	Correlation coeff.	Template
25	2020-05-02T01:13:40.780000Z	0.574911	2020-03-26T21:27:35.03

Low-frequency slopequakes

Table 6: Template event cross-correlation detections of low-frequency slopequakes.

Event	Time	Correlation coeff.	Template
1	2020-03-08T17:58:30.460000Z	0.665116	2020-04-08T17:45:02.14
2	2020-03-12T04:21:20.460000Z	0.791013	2020-04-08T17:45:02.14
3	2020-03-20T16:01:35.735000Z	0.677673	2020-04-08T17:45:02.14
4	2020-03-26T20:02:03.370000Z	0.729245	2020-04-08T17:45:02.14
5	2020-03-26T20:02:06.510000Z	0.702410	2020-04-08T17:45:02.14
6	2020-03-26T20:02:07.670000Z	0.675853	2020-04-08T17:45:02.14
7	2020-03-29T22:25:45.110000Z	0.660889	2020-04-08T17:45:02.14
8	2020-03-30T08:10:36.695000Z	0.658135	2020-04-08T17:45:02.14
9	2020-03-30T21:53:20.640000Z	0.653452	2020-04-08T17:45:02.14
10	2020-03-31T11:21:23.010000Z	0.655108	2020-04-08T17:45:02.14
11	2020-03-31T13:22:47.825000Z	0.682319	2020-04-08T17:45:02.14
12	2020-03-31T14:39:39.295000Z	0.676942	2020-04-08T17:45:02.14
13	2020-03-31T17:04:02.880000Z	0.685295	2020-04-08T17:45:02.14
14	2020-03-31T20:40:21.355000Z	0.663866	2020-04-08T17:45:02.14
15	2020-04-01T00:00:32.720000Z	0.659165	2020-04-08T17:45:02.14
16	2020-04-01T20:13:26.665000Z	0.664457	2020-04-08T17:45:02.14
17	2020-04-07T06:58:33.550000Z	0.658627	2020-04-08T17:45:02.14
18	2020-04-08T06:45:38.660000Z	0.659325	2020-04-08T17:45:02.14
19	2020-04-08T17:45:02.140000Z	1.000000	2020-04-08T17:45:02.14
20	2020-04-08T18:14:43.255000Z	0.661305	2020-04-08T17:45:02.14
21	2020-04-09T01:38:26.285000Z	0.662756	2020-04-08T17:45:02.14
22	2020-04-09T01:38:35.225000Z	0.696557	2020-04-08T17:45:02.14
23	2020-04-09T02:03:59.700000Z	0.781446	2020-04-08T17:45:02.14
24	2020-04-09T02:04:23.405000Z	0.859008	2020-04-08T17:45:02.14
25	2020-04-10T17:33:00.245000Z	0.650314	2020-04-08T17:45:02.14
26	2020-04-11T06:05:22.685000Z	0.657664	2020-04-08T17:45:02.14
27	2020-04-12T08:26:08.410000Z	0.650336	2020-04-08T17:45:02.14
28	2020-04-14T19:50:03.300000Z	0.655579	2020-04-08T17:45:02.14
29	2020-04-16T07:30:44.695000Z	0.678115	2020-04-08T17:45:02.14
30	2020-04-18T08:03:36.230000Z	0.665755	2020-04-08T17:45:02.14
31	2020-04-18T13:11:16.065000Z	0.661211	2020-04-08T17:45:02.14
32	2020-04-18T14:26:35.410000Z	0.670991	2020-04-08T17:45:02.14
33	2020-04-18T14:57:56.590000Z	0.699294	2020-04-08T17:45:02.14

Event	Time	Correlation coeff.	Template
34	2020-04-19T09:50:33.560000Z	0.732217	2020-04-08T17:45:02.14
35	2020-04-19T11:19:54.735000Z	0.735211	2020-04-08T17:45:02.14
36	2020-04-19T22:38:27.605000Z	0.677681	2020-04-08T17:45:02.14
37	2020-04-20T23:43:57.005000Z	0.672264	2020-04-08T17:45:02.14
38	2020-04-21T09:11:18.075000Z	0.659105	2020-04-08T17:45:02.14
39	2020-04-21T11:16:19.225000Z	0.753430	2020-04-08T17:45:02.14
40	2020-04-21T18:41:13.315000Z	0.781858	2020-04-08T17:45:02.14
41	2020-04-21T22:40:08.505000Z	0.756024	2020-04-08T17:45:02.14
42	2020-04-21T22:42:47.150000Z	0.670037	2020-04-08T17:45:02.14
43	2020-04-22T05:38:04.450000Z	0.778476	2020-04-08T17:45:02.14
44	2020-04-22T15:00:25.075000Z	0.702986	2020-04-08T17:45:02.14
45	2020-04-22T15:34:20.645000Z	0.685640	2020-04-08T17:45:02.14
46	2020-04-23T08:20:14.325000Z	0.731622	2020-04-08T17:45:02.14
47	2020-04-23T19:11:14.760000Z	0.732825	2020-04-08T17:45:02.14
48	2020-04-23T19:11:28.225000Z	0.690246	2020-04-08T17:45:02.14
49	2020-04-24T05:10:47.985000Z	0.707672	2020-04-08T17:45:02.14
50	2020-04-24T09:52:33.675000Z	0.672756	2020-04-08T17:45:02.14
51	2020-04-25T02:51:41.585000Z	0.697118	2020-04-08T17:45:02.14
52	2020-04-25T04:52:30.580000Z	0.657235	2020-04-08T17:45:02.14
53	2020-04-25T07:10:26.960000Z	0.672341	2020-04-08T17:45:02.14
54	2020-04-25T19:01:21.255000Z	0.692402	2020-04-08T17:45:02.14
55	2020-04-25T22:14:21.880000Z	0.681623	2020-04-08T17:45:02.14
56	2020-04-26T03:00:10.570000Z	0.664158	2020-04-08T17:45:02.14
57	2020-04-26T07:30:57.000000Z	0.663600	2020-04-08T17:45:02.14
58	2020-04-26T14:26:58.755000Z	0.682645	2020-04-08T17:45:02.14
59	2020-04-26T16:32:07.020000Z	0.663187	2020-04-08T17:45:02.14
60	2020-04-26T17:14:20.510000Z	0.679675	2020-04-08T17:45:02.14
61	2020-04-26T19:31:52.865000Z	0.663409	2020-04-08T17:45:02.14
62	2020-04-26T23:21:53.970000Z	0.709188	2020-04-08T17:45:02.14
63	2020-04-26T23:32:28.815000Z	0.664302	2020-04-08T17:45:02.14
64	2020-04-27T06:59:50.820000Z	0.686765	2020-04-08T17:45:02.14
65	2020-04-27T09:15:46.740000Z	0.678911	2020-04-08T17:45:02.14
66	2020-04-27T09:15:53.325000Z	0.735177	2020-04-08T17:45:02.14
67	2020-04-27T11:37:31.275000Z	0.733738	2020-04-08T17:45:02.14
68	2020-04-27T12:53:33.520000Z	0.722003	2020-04-08T17:45:02.14
69	2020-04-27T17:08:35.875000Z	0.776233	2020-04-08T17:45:02.14
70	2020-04-28T07:35:52.420000Z	0.660977	2020-04-08T17:45:02.14
71	2020-04-28T11:45:16.440000Z	0.659690	2020-04-08T17:45:02.14
72	2020-04-28T14:47:04.620000Z	0.673261	2020-04-08T17:45:02.14
73	2020-04-28T14:48:29.740000Z	0.775200	2020-04-08T17:45:02.14
74	2020-04-28T15:59:18.050000Z	0.669880	2020-04-08T17:45:02.14

Event	Time	Correlation coeff.	Template
75	2020-04-28T16:04:05.340000Z	0.686887	2020-04-08T17:45:02.14
76	2020-04-28T16:24:40.670000Z	0.688767	2020-04-08T17:45:02.14
77	2020-04-29T00:09:07.215000Z	0.686273	2020-04-08T17:45:02.14
78	2020-04-29T12:48:47.335000Z	0.659571	2020-04-08T17:45:02.14
79	2020-04-29T13:42:14.450000Z	0.738489	2020-04-08T17:45:02.14
80	2020-04-29T22:12:39.470000Z	0.667508	2020-04-08T17:45:02.14
81	2020-04-30T10:59:06.380000Z	0.691187	2020-04-08T17:45:02.14
82	2020-04-30T14:54:46.640000Z	0.650816	2020-04-08T17:45:02.14
83	2020-04-30T16:23:12.595000Z	0.658601	2020-04-08T17:45:02.14
84	2020-05-01T13:18:19.605000Z	0.678009	2020-04-08T17:45:02.14
85	2020-05-01T15:19:29.560000Z	0.673268	2020-04-08T17:45:02.14
86	2020-05-01T15:32:36.335000Z	0.681309	2020-04-08T17:45:02.14
87	2020-05-01T23:50:06.060000Z	0.667224	2020-04-08T17:45:02.14
88	2020-05-02T14:30:04.330000Z	0.659734	2020-04-08T17:45:02.14
89	2020-05-02T22:34:53.050000Z	0.658088	2020-04-08T17:45:02.14
90	2020-05-03T00:31:43.930000Z	0.660561	2020-04-08T17:45:02.14
91	2020-05-03T09:59:35.775000Z	0.712669	2020-04-08T17:45:02.14
92	2020-05-03T12:09:26.375000Z	0.654873	2020-04-08T17:45:02.14
93	2020-05-03T12:58:50.365000Z	0.687623	2020-04-08T17:45:02.14
94	2020-05-04T19:47:54.965000Z	0.666650	2020-04-08T17:45:02.14
95	2020-05-04T21:43:02.165000Z	0.653461	2020-04-08T17:45:02.14
96	2020-05-06T13:05:23.535000Z	0.748689	2020-04-08T17:45:02.14
97	2020-05-06T14:08:41.780000Z	0.655960	2020-04-08T17:45:02.14
98	2020-05-06T19:45:56.600000Z	0.721652	2020-04-08T17:45:02.14
99	2020-05-08T07:13:53.975000Z	0.653990	2020-04-08T17:45:02.14
100	2020-05-08T14:14:16.310000Z	0.651398	2020-04-08T17:45:02.14
101	2020-05-08T14:54:15.765000Z	0.683465	2020-04-08T17:45:02.14
102	2020-05-08T18:54:59.330000Z	0.655619	2020-04-08T17:45:02.14
103	2020-05-08T20:36:35.395000Z	0.654394	2020-04-08T17:45:02.14
104	2020-05-21T16:14:37.664999Z	0.662386	2020-04-08T17:45:02.14
105	2020-05-24T15:06:00.930000Z	0.676170	2020-04-08T17:45:02.14
106	2020-05-25T20:25:18.149999Z	0.674160	2020-04-08T17:45:02.14
107	2020-05-26T01:16:59.700000Z	0.678746	2020-04-08T17:45:02.14
108	2020-05-26T01:17:01.215000Z	0.664380	2020-04-08T17:45:02.14
109	2020-05-26T13:58:58.340000Z	0.652900	2020-04-08T17:45:02.14
110	2020-05-28T10:10:06.085000Z	0.699653	2020-04-08T17:45:02.14
111	2020-05-29T10:13:43.465000Z	0.664652	2020-04-08T17:45:02.14
112	2020-05-30T20:11:28.434999Z	0.682299	2020-04-08T17:45:02.14
113	2020-05-31T02:43:09.995000Z	0.694224	2020-04-08T17:45:02.14
114	2020-05-31T06:04:45.605000Z	0.650223	2020-04-08T17:45:02.14
115	2020-06-01T09:17:18.115000Z	0.691689	2020-04-08T17:45:02.14

Event	Time	Correlation coeff.	Template
116	2020-06-05T06:21:17.710000Z	0.670948	2020-04-08T17:45:02.14
117	2020-06-06T17:29:16.355000Z	0.652871	2020-04-08T17:45:02.14
118	2020-06-11T14:14:44.810000Z	0.659033	2020-04-08T17:45:02.14

Rockfalls

Table 7: Events classified as rockfalls.

Event	Time	Duration
1	2020-03-19T07:25:15.920000Z	1.200000
2	2020-03-21T01:34:43.780000Z	3.235000
3	2020-04-03T06:05:38.040000Z	3.695000
4	2020-05-13T06:42:32.660000Z	2.495000
5	2020-06-07T06:50:56.980000Z	9.450000

References

[Andersen et al., 1997] Andersen, T.B., Osmundsen, P.T., Berry, H.N., Torsvik, T.H., Eide, E.A. 1997. Multi-level detachments and exhumation in the Norwegian Caledonides. *Geological Society of America*, 29(6), pp. 317

[Austrheim et al., 2003] Austrheim, H. and Corfu, F. and Bryhni, I., Andersen, T. 2003. The Proterozoic Hustad igneous complex: a low strain calve enclave with a key to the history of the Western Gneiss Region. *Precambrian Research*, 120(1), pp.149-175. https://doi.org/10.1016/S0301-9268(02)00167-5

[Benson et al., 2008] Benson, P.M., Vinciguerra, S., Meredith, P.G., Young, R.P. 2008. Laboratory Simulation of Volcano Seismicity. *Science*, 322, pp.249-252. https://doi.org/10.1126/science.1161927

[Blikra et al., 2006] Blikra, L.H., Longva, O., Braathen, A., Anda, E., Dehls, J., Stalsberg, K. 2006. Rock-slope failures in Norwegian fjord areas: examples, spatial distribution and temporal pattern. In: Evans, S.G., Scarawcia Mugnozza, G., Strom, A.L., Hermanns, R.L.: Landslides from massive rock slope failure. *Nato Science Series*, 49, pp. 475-496. https://doi.org/10.1007/978-1-4020-4037-5_26

[Bormann et al., 2009] Bormann, P., Engdahl, B., Kind, R. 2009. Seismic Wave Propagation and Earth models. In: Bormann, P. (Ed.), *New Manual of Seismological Observatory Practice (NMSOP)*, Potsdam : Deutsches GeoForschungsZentrum GFZ, pp.1-70. https://doi.org/10.2312/GFZ.NMSOP_r1_ch2

[Bolt, 1982] Bolt, B.A. 1982. *Inside the Earth.* W.H Freeman and company, San Francisco.

[Braathen et al., 2004] Braathen, A., Blikra, L.H., Berg, S., Karlsen, F. 2004. Rock-slope failures of Norway; types, geometry, deformation mechanisms and stability. *Norwegian Journal of Geology*, 84, pp.67–88

[Chouet, 1988] Chouet, B. 1988. Resonance of a fluid-driven crack: Radiation properties and implications for the source of long-period events and harmonic tremor. *Journal of Geophysical Research Solid Earth*, 93, pp.4375-4400. https://doi.org/10.1029/JB093iB05p04375

[Braathen, 1999] Braathen, A. 1999. Kinematics of post-Caledonian polyphase brittle faulting in the Sunnfjord region, western Norway. *Tectonophysics*, 302(1), pp.99-121. https://doi.org/10.1016/S0040-1951(98)00281-9

[Deichmann et al., 2000] Deichmann, N., Ansorge., J., Scherbaum, F., Aschwanden, A., Bernard, F., Gudmundsson, G.H. 2000. Evidence for deep icequakes in an Alpine glacier. *Annals of Glaciology*, 31, pp.85-90 https://doi.org/10.3189/172756400781820462

[Derrick et al., 2004] Derrick, T.R., Thomas, J.M. 2004. Time Series Analysis: The Cross-Correlation Function. In: Stergiou, N.(Ed.), *Innovative Analyses of Human Movement*, Illinois: Human Kinetics Publishers, pp.189-205

[Fischer et al., 2019] Fischer, T., Kühn, D., Roth, M. 2019. Microseismic events on the Åknes rockslide in Norway located by a back-projection approach. *Journal of Seismology*, 24, pp. 55-74. https://doi.org/10.1007/s10950-019-09884-5

[Ganerød et al., 2008] Ganerød, G.V., Grøneng, G., Rønning, J.S., Dalsegg, E., Elvebakk, H., Tønnesen, J.F., Kveldsvik, V., Eiken, T., Blikra, L.H., Braathen, A. 2008. Geological model of the Åknes rockslide, western Norway. *Engineering Geology*, 102(1), pp.1-18. https://doi.org/10.1016/j.enggeo.2008.01.018

[Ganerød et al., 2007] Ganerød, G.V., Grøneng, G., Aardal, I.B., Kveldsvik, V. 2007. Core logging of seven boreholes from Åknes, Stranda municipality, Møre and Romsdal County. Technical report 2007.020, Norwegian Geological Survey (NGU)

[Grøneng et al., 2011] Grøneng, G., Christiansen, H.H., Nilsen, B., Blikra, L.H. 2011. Meteorological effects on seasonal displacements of the Åknes rockslide, western Norway. *Landslides*, 8(1), pp.1-15. https://doi.org/10.1007/s10346-010-0224-x

[Harbitz et al., 2015] Harbitz, C.B., Glimsdal, S., Kveldsvik, V., Løvholt, F., Pedersen, G., Jensen, A. 2015. Mulige flodbølger fra Åkerneset. Åkneskonferansen: Norwegian Geotechnical Institute (NGI)

[Heincke et al., 2010] Heincke, B., Günther, T., Dalsegg, E., Rønning, J.S., Ganerød, G.V., Elvebakk, H. 2010. Combined three-dimensional electric and seismic tomography study on the Åknes rockslide in western Norway. *Journal of Applied Geophysics*, 70(4), pp.292-306. https://doi.org/10.1016/j.jappgeo.2009.12.004

[Holland, 2013] Holland, A. A. 2013. Earthquakes Triggered by Hydraulic Fracturing in South-Central Oklahoma. *Bulletin of the Seismological Society of America*, 103(3), pp.1784-1792. https://doi.org/10.1785/0120120109

[Köhler et al., 2019] Köhler, A., Maupin, V., Nuth C., Van Pelt, W. 2019. Characterization of seasonal glacial seismicity from a single-station on-ice record record at Holtedahlfonna, Svalbard. *Annals of Glaciology*, 60(79), pp.23-36. https://doi.org/10.1017/aog.2019.15

[Luckman, 2013] Luckman, B.H., 2013. Processes, Transport, Deposition, and Landforms: Rockfall. In: Shroder, J., Marston, R.A., Stoffel, M. *Treatise on Geomorphology*. Academic Press, San Diego, 7, pp.174-182. https://doi.org/10.1016/B978-0-12-374739-6.00162-7

[Norgeskart, 2021] Norgeskart. 2021. Åkerneset. Norgeskart. Retrieved from https://www.norgeskart.no/#!?project=norgeskart&layers=1002&zoom=13&lat=6919348.66&lon=84197.50&markerLat=6919348.658283825&markerLon=84197.50154621917&panel=searchOptionsPanel&sok=%C3%85kerneset

[Nuttli et al., 1961] Nuttli, O., Whitmore, J.D. 1961. An Observational Determination of the variation of the angle of incidence of P-waves with epicentral distance. *Bulletin of the Seismological Society of America*, 51, pp.269-276

[NVE, 2020] NVE. 2020. Åknes. Norges vassdrags- og energidirektorat (NVE). Retrieved from https://www.nve.no/flaum-og-skred/fjellskredovervaking/kontinuerlig-overvakede-fjellpartier/aknes/

[Osmundsen et al., 2001] Osmundsen, P.T., Andersen, T.B. 2001. The middle Devonian basin of western Norway; sedimentary response to large-scale transtensional tectonics?. *Tectonophysics*, 332 (1-2), pp.51-68. https://doi.org/10.1016/S0040-1951(00)00249-3

[Park et al., 2018] Park, S., Ishii, M. 2018. Near-surface compressional and shear wave speeds constrained by body-wave polarization analysis. *Geophysical Journal International*, 213, pp.1559-1571. https://doi.org/10.1093/gji/ggy072

[Provost et al., 2018] Provost, F., Malet, J-P., Hibert, C., Helmstetter, A., Radiguet, M., Amitrano, D., Langet, N., Larose, E., Abancó, C., Hürlimann, M., Lebourg, T., Levy, C., Le Roy, G., Ulrich, P., Vidal, M., Vial, B. 2018. Towards a standard typology of endogenous landslide seismic sources. *Earth Surface Dynamics*, 6, pp.1059-1088. https://doi.org/10.5194/esurf-6-1059-2018

[Reynolds, 2011] Reynolds, J.M. 2011. *An introduction to applied and environmental geophysics*. Wiley-Blackwell, Chichester, pp.145-148

[Roth et al., 2009] Roth, M., Blikra, L.H. 2009. Seismic monitoring of the unstable rock slope at Aaknes, Norway. *Geophysical research abstracts*, 11

[Silverberg, 2020] Silverberg, F.M.J. 2020. Feature and event analysis of seismic data using machine learning at Åknes (Master's Thesis). Retrieved from https://www.duo.uio.no/handle/10852/79208

[Thomas et al., 2016] Thomas, A.M., Beroza, G.C., Shelly, D.R. 2016. Constraints on the source parameters of low-frequency earthquakes on the San Andreas Fault. *Geophysical research letters*, 43, pp. 1464-1471. https://doi.org/10.1002/2015GL067173

[Tonnellier et al., 2013] Tonnellier, A., Helmstetter, A., Malet, J-P., Schmittbuhl, J., Corsini, A., Joswig, M. 2013. Seismic monitoring of soft-rock landslides: the Super-Sauze and Valoria case studies. *Geophysical Journal International*, 193, pp.1515-1536. https://doi.org/10.1093/gji/ggt039

[Trnkoczy, 1999] Trnkoczy, A. 1999. Understanding and parameter setting of STA/LTA trigger algorithm. In: Bormann, P. (Ed), *New Manual of Seismological Observatory Practice 2 (NMSOP-2)*, Potsdam: Deutsches GeoForschungsZentrum GFZ, pp.1-20

[Tucker et al., 1990] Tucker, R.D., Krogh, T.E., and Råheim, A. 1990. Proterozoic evolution and age-province boundaries in the central part ofthe Western Gneiss Region, Norway: results of U/Pbdating of accessory minerals from Trondheimsfjord to Geiranger. Mid-Proterozoic geology of the Southern Margin of Proto-Laurentia-Baltica. *Geological Association of Canada Special Paper*, 241, pp.33-50

[Varnes, 1978] Varnes, D.J., 1978. Slope Movement Types and Processes. In: Schuster, R.L., Krizek, R.J, *Landslides - Analysis and control*: National Research Council, Washington D.C, Transportation Research Board, 176, pp.11-33